Measuring the Resolution of a GEM - TPC in a Magnetic Field

by

Gabriel Rosenbaum
B.Sc., University of Victoria, 2002.

Thesis Submitted in Partial Fulfillment of the
Requirements for the Degree of

Master of Science

in the Department of Physics and Astronomy.

Abstract

Supervisor: Dr. Dean Karlen

The University of Victoria detector research team has been testing a prototype for a central tracker for use at the proposed International Linear Collider. This detector must have excellent momentum resolution in a strong magnetic field (which means it must have excellent spatial resolution). The University of Victoria's prototype detector is a Time Projection Chamber (TPC). A TPC uses a pad array to collect ionization tracks, and uses timing information to reconstruct tracks of charged particles in three dimensions. Our detector uses gas electron multipliers (GEMs) for electron gain in the gas and was the first to be tested in magnetic fields.

During the summers of 2003 and 2004, the chamber was operated in a strong axial magnetic field at the DESY laboratory in Hamburg to determine its capabilities in reconstructing cosmic ray tracks. A UV laser system was also designed and built to aid in calibration and in assessing systematics. The results of these tests are presented and demonstrate the excellent tracking resolution of a GEM-TPC.

Supervisor: Dr. Dean Karlen, (Department of Physics and Astronomy)

Contents

List of Figures

List of Tables

Chapter 1

Introduction

1.1 Motivation

The standard model in particle physics (SM) precisely describes properties of the fundamental particles and the interactions between them and has been tested and confirmed in many different ways for many years. Every particle in the standard model has been observed except for the particle known as the Higgs boson. The Higgs particle is expected to be discovered at the Large Hadron Collider (LHC) which is currently under construction at CERN and will turn on in 2007. The LHC will be a proton-proton collider capable of center of mass energies of up to 14 TeV. Although this proton collider will be a carnival of interesting physics for many years to come it is not the tool for every job. For the past few decades particle physicists have primarily used two types of machines to test their theories. These are: proton colliders[1] and electron colliders[2]. Proton colliders can achieve collision energies which are much

[1]This refers to protons or antiprotons.
[2]This refers to electrons or positrons.

higher than electron colliders making it possible to produce more massive particles. However, a proton is not a fundamental particle. It is made up of quarks (fundamental fermions) and gluons (the force-carrying bosons of the strong force). The fact that proton colliders bring composite particles into collision raises two difficulties: 1) Each particle in the proton carries a varying fraction of the proton's momentum so the energy involved in each interaction is not known a priori; and 2) Since the proton is made up of many constituents the initial state is much more complicated than that of two colliding electrons. While proton machines can scan high energies and have been used to make discoveries, the electron colliders can make precision measurements of particle properties and physical observables.

Currently scientists from around the globe are collaborating to finalize a design proposal for an electron-positron collider which would be built after the LHC turns on and be used to make precision measurements of the physical processes seen first at the LHC. The International Linear Collider (ILC) would collide electrons and positrons at center of mass energies of up to 1 TeV allowing us to produce all of the standard model particles including the Higgs boson[3].

The linear collider will need an elaborate detector to precisely measure the products of the interaction of the electron and positron collisions. Our group's research is focused on testing a time projection chamber which has been designed as a prototype for the central tracking detector at the ILC. The tracking detector will

[3]The ILC will not be constrained to study only Higgs physics. It will also be an extremely useful tool if evidence of other theories are seen, such as super-symmetry.

need to operate in a strong magnetic field and reconstruct in three dimensions the tracks of charged particles which pass through it. Because these charged particles are moving in a magnetic field, they travel in a curved path. By accurately reconstructing their trajectories we can determine their momenta by the curvature of their path.

1.2 Goals

One of the major physics processes of interest at the linear collider will be Higgs-strahlung production, where the positron and electron annihilate producing a virtual Z-boson which goes to a Z-boson and a Higgs ($e^+e^- \rightarrow Z^* \rightarrow Z^0H^0$) see figure 1.1.

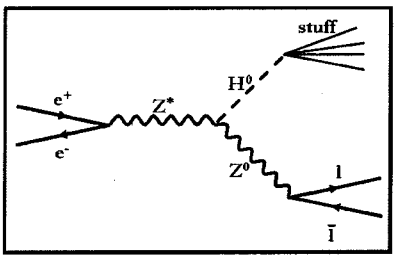

Figure 1.1: Higgstralung process.

The case where the Z-boson decays to a lepton, anti-lepton pair ($Z^0 \rightarrow l\bar{l}$) is significant since the recoil mass of the Higgs can be reconstructed exclusively from the momenta of the lepton anti-lepton pair. However, the precision needed in measuring the momenta of the two leptons is the most challenging task for the central tracker at the linear collider. Figure 1.2 shows examples of the relative size of the Higgs mass peak as compared to backgrounds for situations with two different momentum resolutions. The red curve shows the simulated signal with a transverse

momentum resolution of $\delta(1/p_t) < 5 \times 10^{-5}\, GeV^{-1}$, the goal for the entire detector, which translates into a momentum resolution goal for the central tracker alone of $\delta(1/p_t) < 2 \times 10^{-4}\, GeV^{-1}$[1]. The green curve shows the simulated signal in the case where the momentum resolution is four times worse. It is convenient to consider the resolution in terms of the spatial resolution for each point that is measured along the track of the charged particle. If we let B (in tesla) be the magnetic field (which is perpendicular to the transverse direction) and R (in meters) be the radius of curvature of the track, then the transverse momentum, p_t (in GeV) is given by[2]:

$$p_t = 0.3BR \tag{1.1}$$

Now, define k as $\frac{1}{R}$ and we obtain,

$$\delta(1/p_t) = \frac{\delta k}{0.3B} \tag{1.2}$$

where

$$\delta k = \frac{\epsilon}{L'^2}\sqrt{\frac{720}{N+4}}\,. \tag{1.3}$$

Where N is the number of points measured along the track ($N \geq 10$), L' is the length of the projection of the track in the transverse plane and ϵ is the spatial measurement error for each point. Finally,

$$\epsilon = \delta(1/p_t)0.3BL^2\sqrt{\frac{N+4}{720}}\,. \tag{1.4}$$

Reasonable parameters for a full scale tracker at the ILC are $B = 4T$, $L' = 1m$,

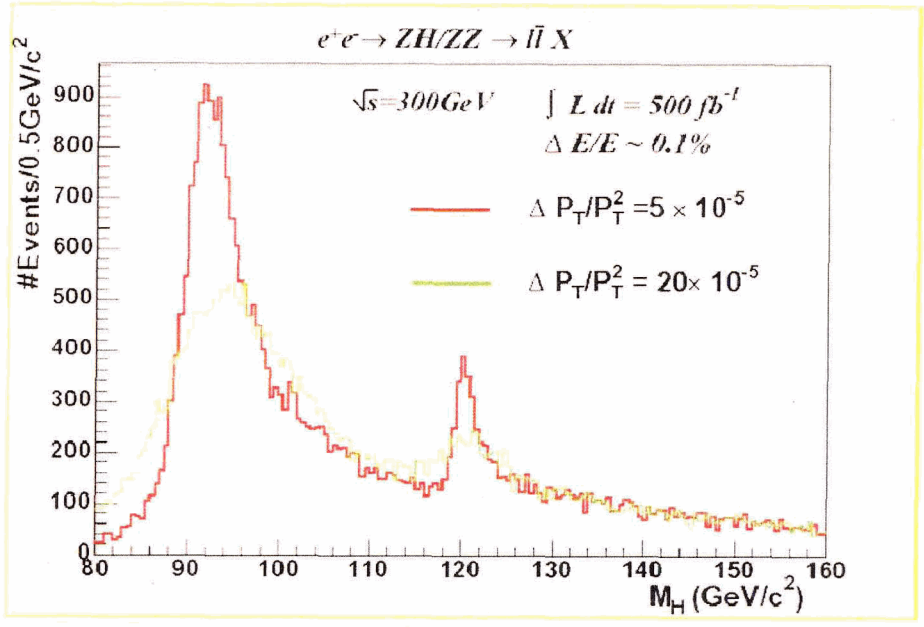

Figure 1.2: Simulated Higgs mass peak. The red curve shows a simulated signal measured at the momentum resolution goal for the ILC detector. The green curve shows the signal measured at a resolution which is four times worse[3].

$N = 145$ and $\delta(1/p_t) < 2 \times 10^{-4} GeV^{-1}$ resulting in a space point resolution goal of:

$$\epsilon < 110\,\mu m \tag{1.5}$$

Chapter 2

Description of Time Projection Chambers

2.1 What is a TPC?

A time projection chamber uses the ionization track of a charged particle through a gas to reconstruct the particle's trajectory in three dimensions. For example let us consider the chamber as a cylinder with its axis defined as the z-direction (see figure 2.1). The cylinder is filled with a gas mixture and an electric field is applied throughout the chamber's volume along the axial (or z) direction[1]. A charged particle will leave a trail of ionization along its path which consists of electrons and positively charged ions. The electrons are transported by the electric field in the z-direction to one end of the TPC. Near this end the signal is amplified through additional ionizations. A signal is then produced on conducting pads which lie in the plane defined by the x and y axes (which we will call the transverse plane). This signal is produced by collecting all of the electrons from the ionization on the pads or by the

[1]There is also a magnetic field applied in the z-direction whose importance will be discussed later.

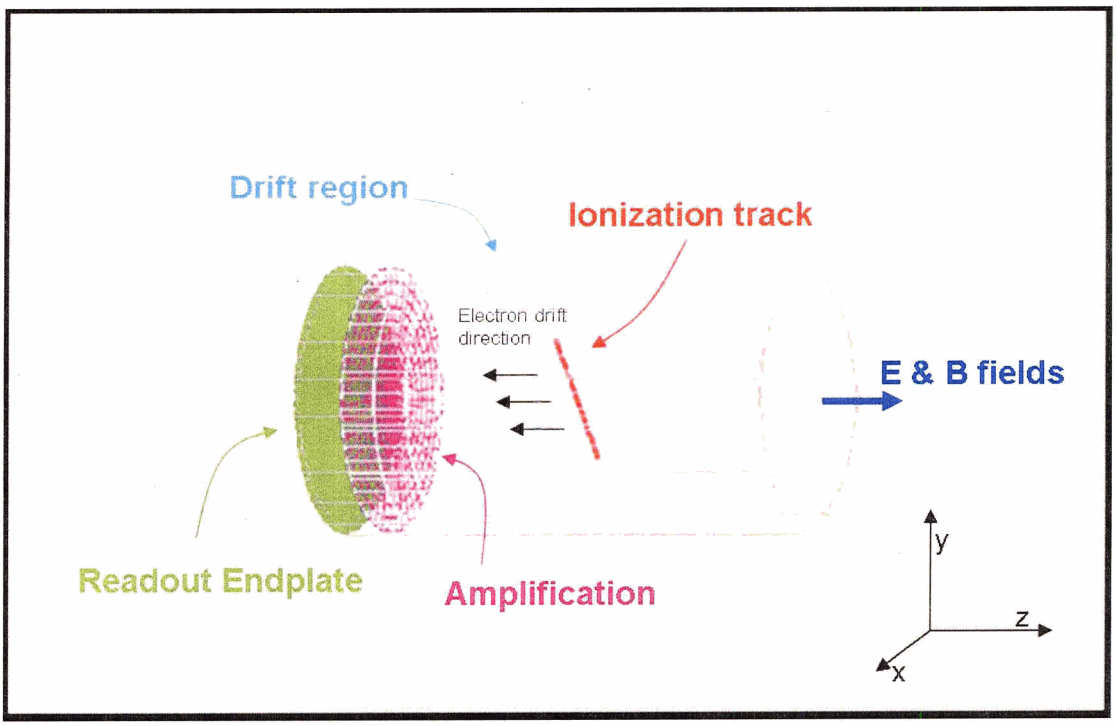

Figure 2.1: Schematic of a generic TPC

motion of the positive ions which have been produced in the ionization. The x and y coordinates of the initial track are determined by the distribution of signals in the transverse plane. The z coordinate of the track is estimated by measuring the arrival times of the signal. The drift time through the volume of the chamber is proportional to the z-distance from the end plane since the electrons drift through the chamber at a constant speed[2].

[2]This will be discussed in more detail later.

2.2 Regions

It is useful to consider the TPC in three sections. They are: the drift region where the ionization takes place and through which the ionized electrons are transported, the amplification region in which the number of charged particles is increased, and the readout region where charge is measured for tracking.

For the track to maintain its original shape, the electric field in the drift region must be uniform and parallel to the axis of the chamber in order to keep the electron trajectories straight as they drift toward the amplification region. There are numerous ways in which the number of electrons can be amplified in the chamber. Although the details of how this is done will vary from chamber to chamber the general principle is to use a region of very high electric field in which the electrons gain enough energy to ionize other atoms. The resulting electrons can then ionize other atoms and so on, causing an electron avalanche. The method specific to our research will be discussed in the following chapter. In this thesis we will discuss the method for readout by collecting the electrons directly onto conducting pads. As will be seen in the following chapter, one must choose the appropriate gas and electric and magnetic fields in order to optimize the reconstruction capability of the detector.

2.3 Limitations of Wire TPCs

Originally time projection chambers used a series of thin wires located directly above the pad array to amplify the signal from the primary electrons from the initial ionization. The drifting electrons would follow the electric field lines into these wires. In the region very close to these wires the electrons see a very strong electric field. The electrons gain enough energy in this field to ionize atoms in the gas. These ionized electrons can then have enough energy to ionize other atoms, causing an avalanche. However, primary electrons (which are not in line with a wire when ionized) must acquire a velocity component perpendicular to the magnetic field direction in order to drift toward the wires. The electrons now with a transverse component to their velocity feel a force from the magnetic field.

Consider two elements of charge along the track (one above a wire and one below). The force due to the magnetic field will be in different directions for each charge element (see figure 2.2) causing the track to rotate slightly. As an example of the effect of having a section of the track rotated consider a track which would pass directly between two pads sharing its charge equally with both pads regardless of how the charge is distributed along the track. However, if the track has a rotated section the fluctuations in the charge density along the track can cause the charge to be shared unevenly between the pads (see figure 2.3). This effect, know as the $\mathbf{E} \times \mathbf{B}$ effect, has been the limiting factor for spatial resolution of wire TPCs. An alternative

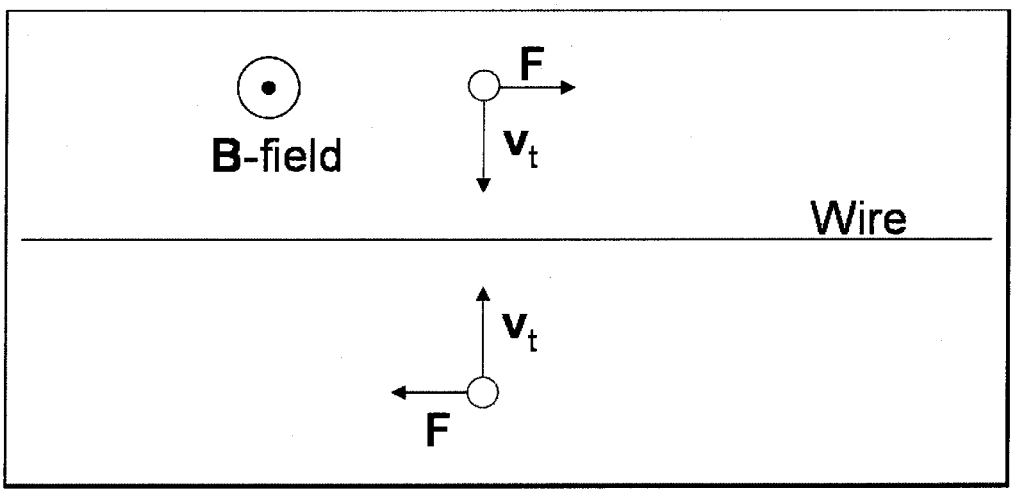

Figure 2.2: A segment of charge above a wire will feel a force (due to the magnetic field) which is in the opposite direction of a segment of charge which is below a wire

to wire amplification will be discussed in later sections.

2.4 Gas Properties and Fields

The choice of gas constituents and strength of magnetic and electric fields must be considered in tandem to maximize the performance of a TPC. In this section we will discuss the important properties of electron transport in gases and the effect of varying magnetic and electric fields.

The properties of electron transport through a gas depend, in general, on the constituents of the gas, gas pressure and temperature, and the electric and magnetic fields. In all following discussions it will be assumed that the TPC operates at a constant pressure and temperature and that the electron drift velocities are small compared to thermal velocities. Instead of discussing gas properties in terms of

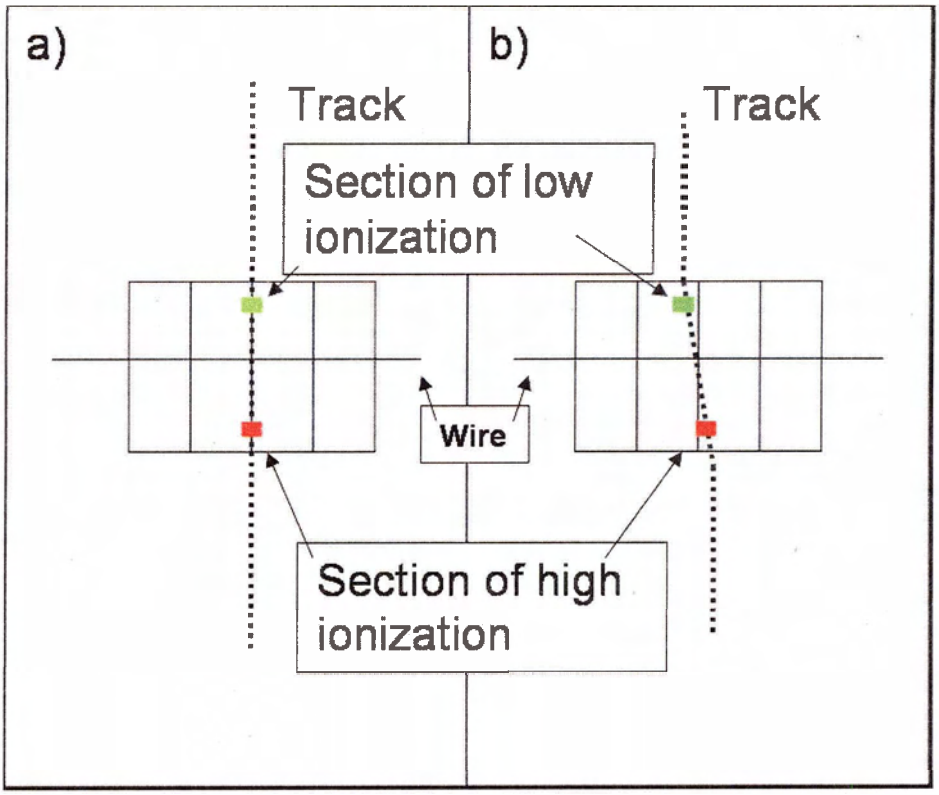

Figure 2.3: A track with a rotated section can skew charge sharing between pads with fluctuations in ionization.

pressure and electric field one will obtain the same results by considering only the ratio of electric field to pressure (E/P) instead of electric field on its own. All mention of the electric fields will be given in kV/cm assuming that the pressure is one atmosphere, however, this value can be scaled by 1/P for a chamber operating at a different pressure.

2.4.1 Drift Velocity

Electrons drifting though a gas in the presence of an electric field very quickly reach a constant velocity called the drift velocity. The drift velocity is a function of E/P and gas constituents. In the situation of the TPC with the electric and magnetic fields being parallel, the drift velocity is not a function of magnetic field and the electrons drift in the direction of the fields. Often the gas and the electric field are chosen so that the drift velocity is at a maximum. This allows the chamber to be cleared of ionization quickly and, since the velocity is at a maximum there will be less of an effect on the drift velocity with small changes in electric field or pressure (see figure 2.4). Since the z-coordinate is reconstructed using the drift velocity it is important that this quantity be well known.

2.4.2 Diffusion

As the electron cloud in the TPC drifts it spreads out (or diffuses) in all directions in the form of a Gaussian distribution. We define the width of the cloud due to diffusion as the standard deviation of this Gaussian ($\equiv \sigma$). The number of electrons

per infinitesimal distance (dx) in the x direction after some time t is given by

$$\frac{dN}{dx} = \frac{N_{tot}}{D_x\sqrt{2\pi t}}\, e^{\frac{-(x-\mu_x)^2}{2D_x^2 t}} \tag{2.1}$$

where N_{tot} is the total number of electrons in the distribution, μ_x is the x position of the center of the track and D_x is known as the diffusion constant. The width of the track (σ) in the x-direction is then given by

$$\sigma_x^2 = D_x^2 t\ . \tag{2.2}$$

We have defined the x direction as the transverse direction (perpendicular to the axis of the chamber) so we change our labels here to

$$\sigma^2 = D_t^2 t\ . \tag{2.3}$$

We also consider the diffusion in the longitudinal (z) direction where the track width is σ_l, where

$$\sigma_l^2 = D_l^2 t\ . \tag{2.4}$$

When electrons drift parallel to the magnetic field (as in a TPC) the magnetic field has a substantial effect on the transverse diffusion (while the longitudinal diffusion is unaffected). Once the electron acquires a velocity in the transverse direction the Lorentz force acts on it spiraling it along the direction of drift. Thus the transverse diffusion constant (D_t) is a function of E and B, while the longitudinal diffusion constant (D_l) is a function of only E. The effect of differing magnetic fields for an argon-methane mix is shown in figure 2.5.

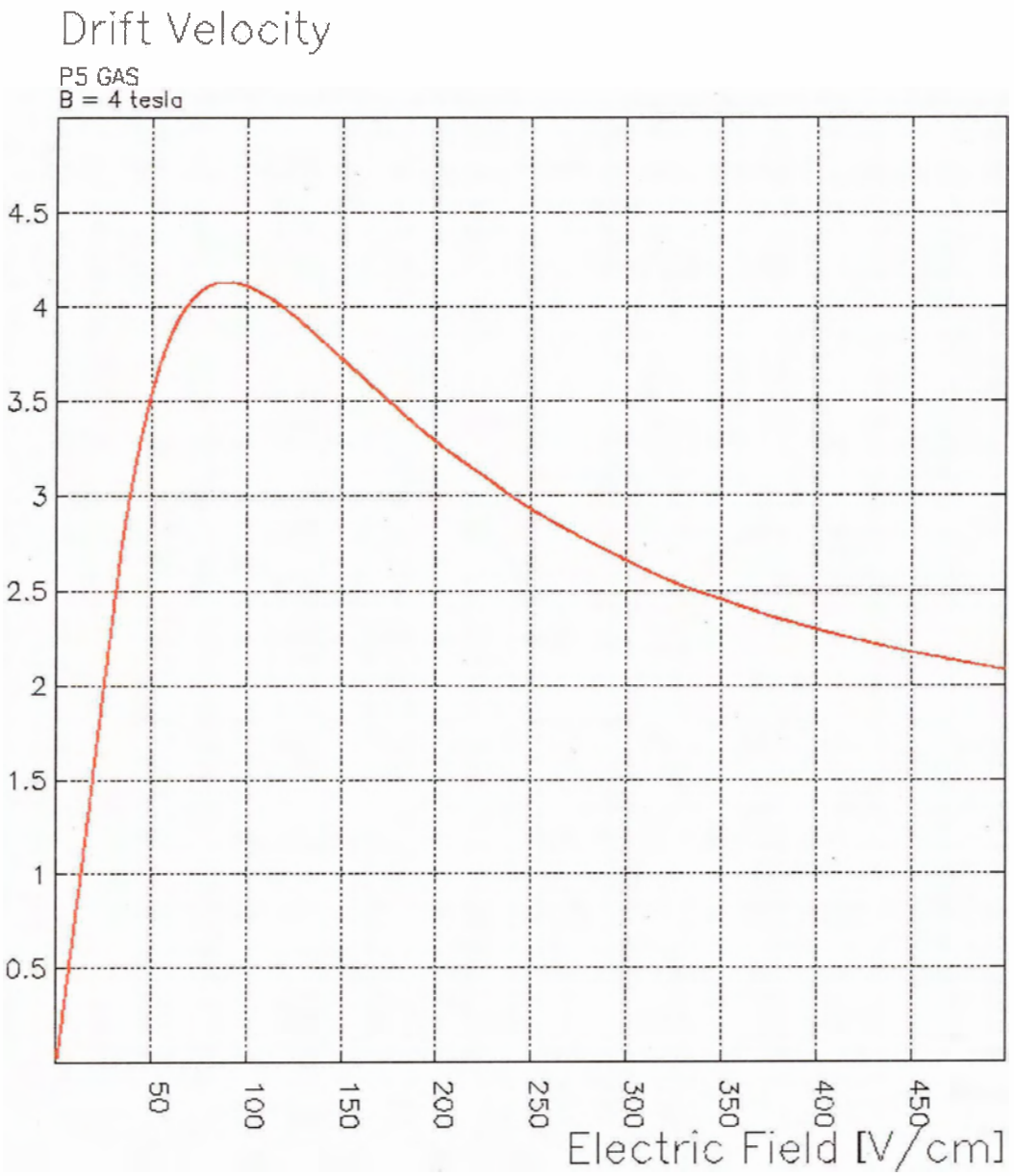

Figure 2.4: Drift velocity of 95:5 argon:methane mixture, generated using the Magboltz simulation program.

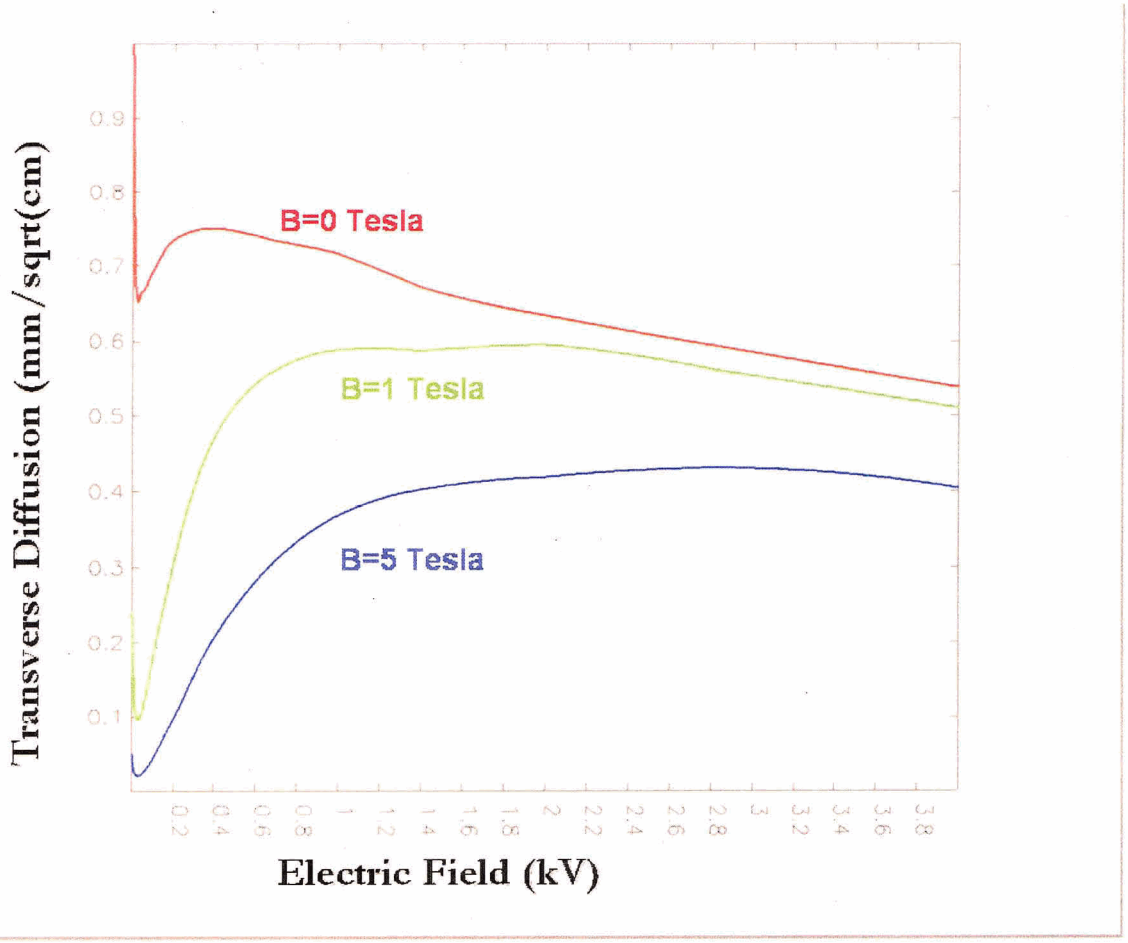

Figure 2.5: Transverse diffusion as a function of electric field for varying magnetic fields in 95:5 argon:methane mixture, generated using the Magboltz simulation program. (NB: The longitudinal diffusion is similar to the transverse diffusion at B=0T .)

2.4.3 Attachment and Townsend Coefficients

Some gases have a significant electron attachment cross section, that is, a significant probability that a drifting electron will attach itself to a gas atom. Examples of this type of gas are H_2O, O_2, and SF_6. Although there are some applications in which these gases can be useful, in general they are avoided in the TPC volume. The attachment coefficient (A) is defined so that $A\,dz$ is the probability that after some drift distance dz the electron attaches to an atom. Then the number of electrons remaining after some drift distance z considering only attachment is

$$N(z) = N_0 e^{-Az} . \tag{2.5}$$

Similarly the Townsend coefficient (T) is defined so that $T\,dz$ is the probability of an electron ionizing an atom in a distance dz, which gives the number of electrons after a distance z (when considering only ionization) of

$$N(z) = N_0 e^{Tz} . \tag{2.6}$$

Combining these effects we get

$$N(z) = N_0 e^{(T-A)z} \tag{2.7}$$

as the total number of electrons after a drift distance z. We then must choose our fields and a gas mixture so that A is insignificant and T is large enough in the amplification region to obtain an appreciable gain.

2.5 History of Time Projection Chambers

At the end of the 1970's the technology of accelerators had made significant advances, but there had been few major developments in detectors. With the planning of accelerators with higher energies such as the Positron Electron Project (PEP) at the Stanford Linear Accelerator Center (SLAC) and Positron Electron Tandem Ring Accelerator (PETRA) at the Deutschen Elektronen Sychrotron laboratory (DESY) in Germany, a new type of detector was going to be necessary. A study of the detector which would be needed for PEP was done. To avoid synchrotron radiation, the magnetic field would have to be in the same direction as the beam. Drift chambers could be used, but the detectors for particle identification, such as Cerenkov detectors, would have to be outside of the tracking detectors yet inside the magnet coils. As well there would have to be many other components including one meter of steel for muon absorption which would have an outer diameter of over ten meters. This huge detector would be unfeasible and another idea was needed. This idea was conceived by one of the scientists working on the PEP project, David Nygren [4]. Nygren's idea was to have the electric and magnetic fields aligned parallel to each other. This detector would be operated at positive pressure in order to obtain more ionization and hence better statistics. By tracking the path of the charged particle in a magnetic field, the chamber operated as a magnetic spectrometer while the amount of ionization in the gas would be measured at numerous space points in order to determine a

particle's energy loss per unit distance (a measurement which is needed for particle identification). This group developed such a detector and called it a time projection chamber or TPC. The first full scale TPC application was the PEP-4 detector at SLAC. Since then TPCs have been used in numerous other experiments, perhaps most notably in two of four major experiments at LEP (the world's largest electron positron collider at CERN, near Geneva): DELPHI[5] and ALEPH[6]. DELPHI used a 1.3m x 2m cylindrical TPC (see figure 2.6) filled with a gas of 80% argon and 20% methane and operated in a 1.2 tesla magnetic field. This chamber was able to achieve spatial resolution of $250\,\mu m$ and $900\,\mu m$ in the transverse and longitudinal directions respectively, using a sampling length of $45\,mm$ per point. The ALEPH TPC had a radius of $1.8\,m$ and two drift volumes each of $2.2\,m$. It used a gas mixture of 91% argon and 9% methane in a magnetic field of 1.5 tesla. The ALEPH TPC (see figure 2.7) achieved point resolutions of approximately $180\,\mu m$ and $900\,\mu m$ in the transverse and longitudinal directions using a sampling length of $30\,mm$. TPCs are also in use or being planned in heavy ion collider experiments such as STAR at RHIC (at the Brookhaven Laboratory, on Long Island, New York) and ALICE at the LHC (at CERN) respectively.

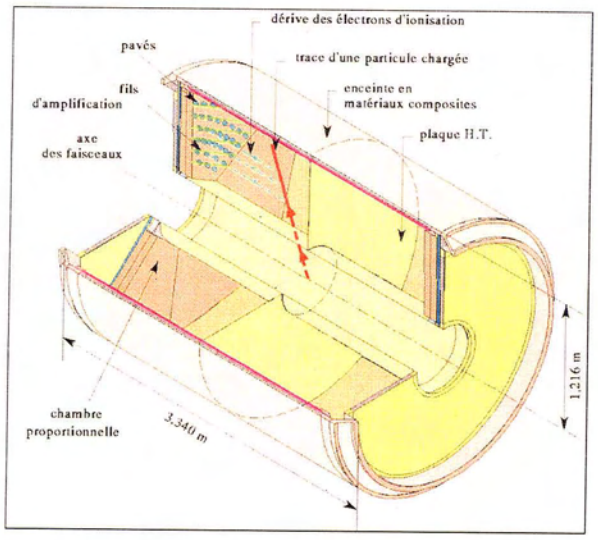

Figure 2.6: An artist's rendering of the DELPHI TPC.

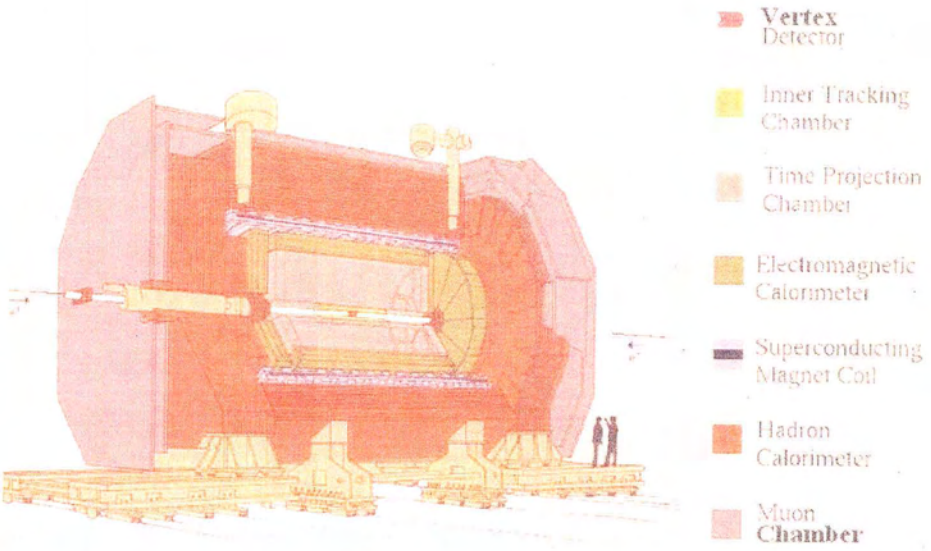

Figure 2.7: An artist's rendering of the ALEPH detector with the TPC shown in pink.

Chapter 3

University of Victoria TPC

3.1 TPC R&D at UVic

Since July 2002 the University of Victoria has had a group researching time projection chambers as a possible choice for the central tracker for the proposed high energy e^+e^- linear collider. This research has been focused on testing the capabilities of our time projection chamber (which we will refer to as the University of Victoria TPC or UVTPC for short), shown in figures 3.1 and 3.2. The UVTPC was designed as a small scale prototype for the linear collider central tracker. It has a drift volume $30\,cm$ long and an outer diameter of about $25\,cm$. This chamber has been equipped with quartz windows that transmit ultra-violet light which allows for experiments involving ionization tracks from laser pulses as well as tracks from cosmic rays.

3.2 Gas Amplification

The UVTPC uses what are known as Gas Electron Multipliers[7] (GEMs) for gas amplification. A GEM consists of a thin sheet ($50\,\mu m$ thick) of dielectric material

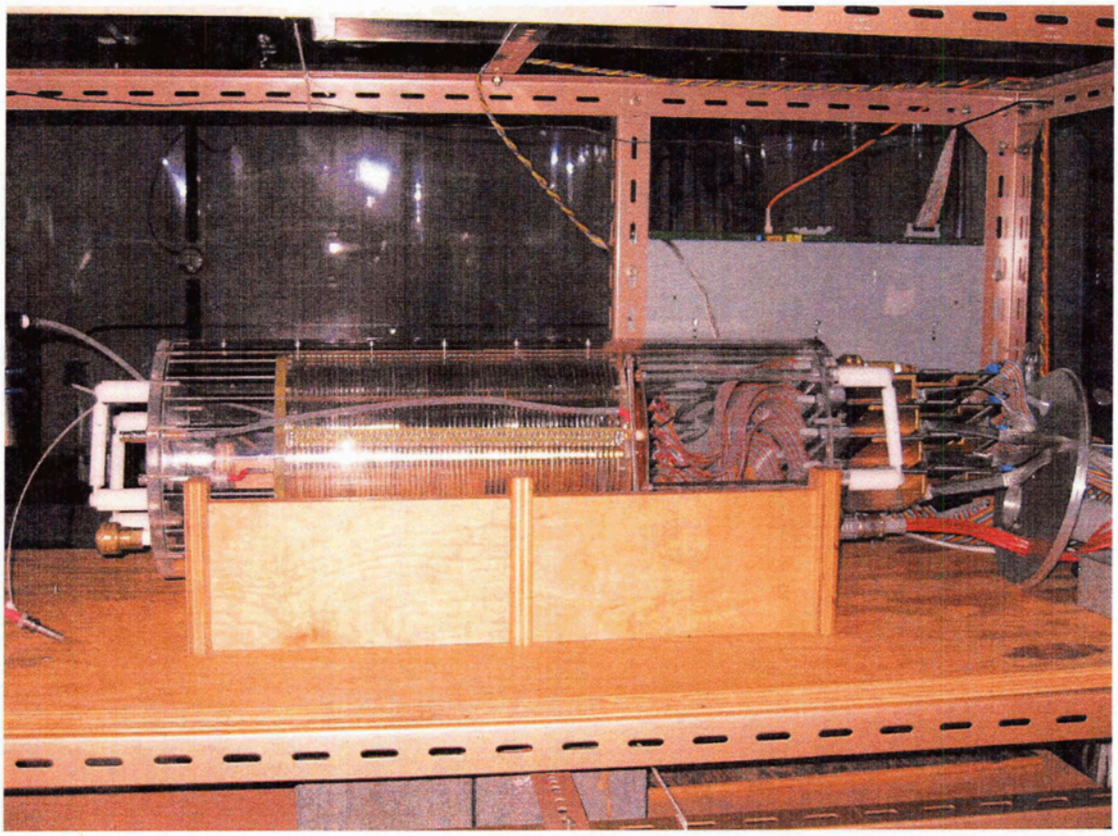

Figure 3.1: The University of Victoria's Time Projection Chamber

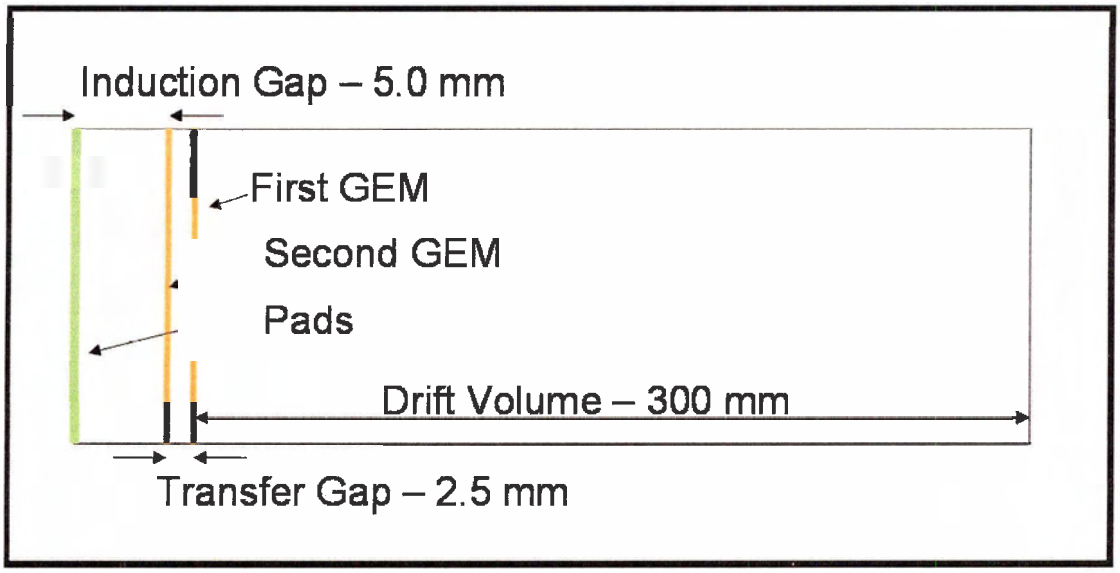

Figure 3.2: Schematic of the University of Victoria's Time Projection Chamber

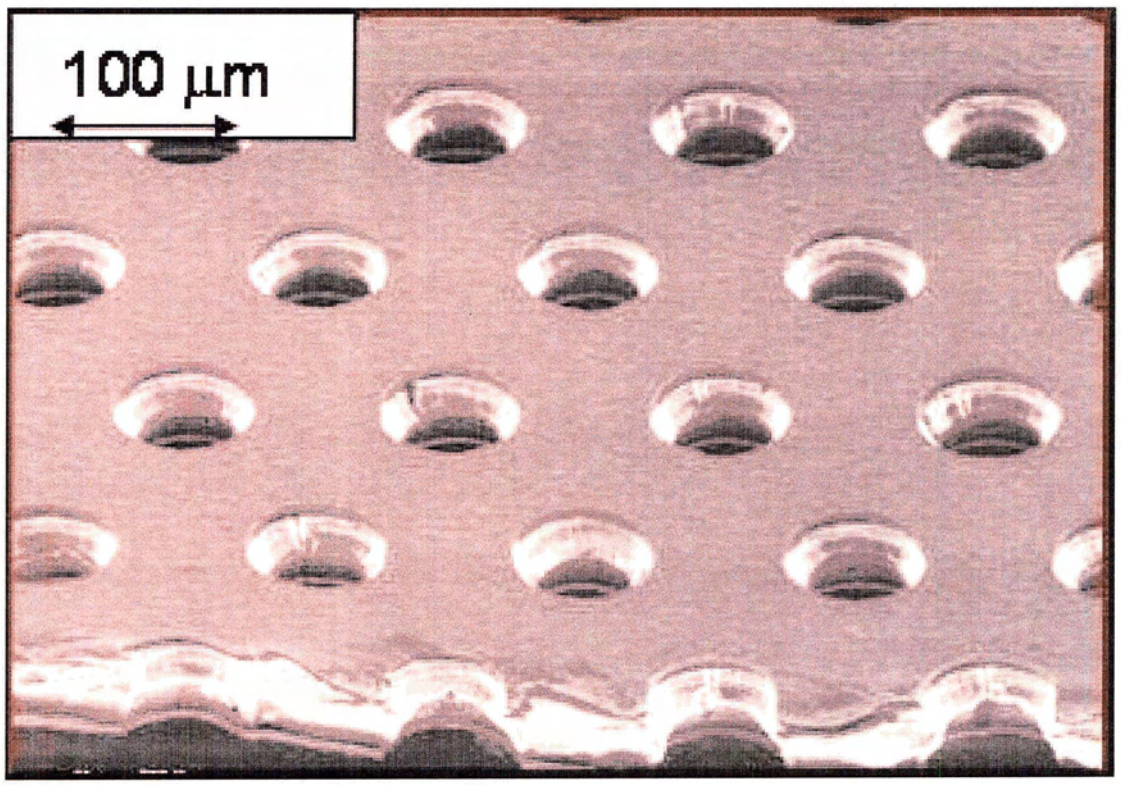

Figure 3.3: Electron microscope image of the hole pattern on a GEM foil[8].

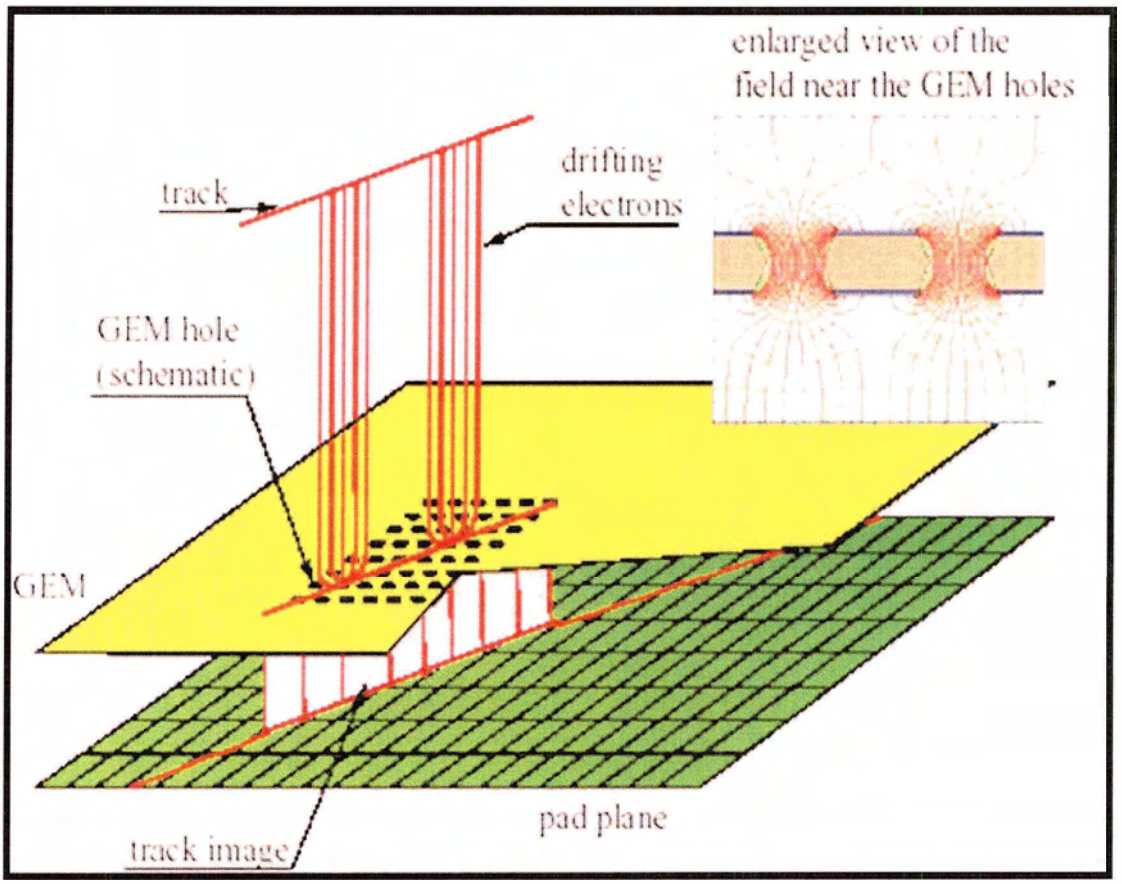

Figure 3.4: Schematic of GEM holes[1] with electric field lines shown[9]

with a conducting layer on each side. This three layer foil has a series of holes through it with an hexagonal pitch of approximately $140\,\mu m$ between centers. The holes are a double conical shape, with an outside diameter of $70\,\mu m$ and a center diameter of $50\,\mu m$ (see figure 3.3 and 3.4). The two conducting layers are maintained at a high potential relative to each other and are insulated from each other by the middle layer. The high voltage across such a short distance allows for a very high electric field of order ($\mathcal{O}[80]\,kV/cm$) inside the holes of the GEM. The drifting electrons follow the electric field lines into the holes of the GEM foil. When these electrons enter the holes they gain enough energy to ionize atoms in the gas. The ionized electrons then have enough energy to cause another ionization. This repeats multiple times causing what is called an electron avalanche. The gain of an individual GEM depends on the choice of gas, the hole dimension and the GEM voltage. Typically in a TPC which uses GEMs for electron amplification either two or three GEMs are used. In the UVTPC two GEMs are used. These GEMs are maintained at a potential of approximately 350V-450V between the conducting layers resulting in an amplification of approximately 70-90 per primary electron therefore resulting in a total gain of of order $\mathcal{O}[5000 - 10000]$.

As mentioned in the previous chapter, the factor that limits the spatial resolution capabilities of a TPC which uses wires for amplification is the $\mathbf{E} \times \mathbf{B}$ effect. When a GEM is used for amplification the electrons only need to travel in the transverse direction far enough to reach a hole in the GEM.

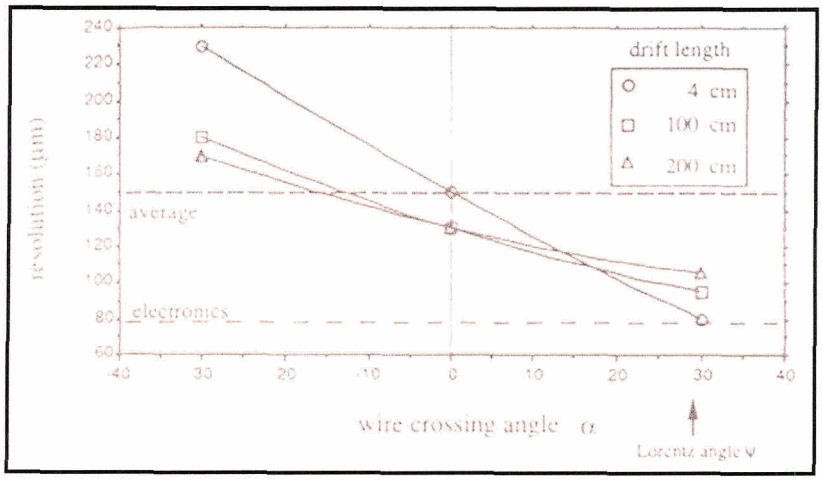

Figure 3.5: Transverse resolution vs. wire crossing angle for the ALEPH TPC in which the sampling length per row is $30\,mm$[10].

The electric field has very small transverse components even near the GEM foil because the holes are separated by only $140\,\mu m$, essentially eliminating $\mathbf{E} \times \mathbf{B}$ effects. Figure 3.5 [10] shows the transverse resolution for a wire TPC (ALEPH TPC) as a function of wire crossing angle. When the wire crossing angle is equal to the Lorentz angle[1] the $\mathbf{E} \times \mathbf{B}$ effect is minimized and the resolution is optimized.

Another advantage of a GEM-TPC is that the signals seen on the pads are narrower, both spatially and temporally, allowing for better two track separation. Since a wire TPC uses induced signals from the motion of positive ions (which drift extremely slowly) there is a long tail (in time) associated with the signals. A TPC which uses GEMs collects the electrons directly on the pads which has a much narrower signal in time as the electrons drift approximately 1000 times faster than the

[1]The Lorentz angle is the angle between the electron drift direction and electric field direction for an electron drifting in an electric and magnetic field. In a GEM-TPC the electrons have a Lorentz angle very close to zero from ionization to collection.

ions. Spatially we consider what is called a pad response function (PRF). A PRF is a function which describes the distribution of signals which will be seen on the pads. Since a GEM TPC collects electrons directly on the pad response function can be considered to be the same as the distribution of the electrons due to diffusion, which is a Gaussian distribution. In a high magnetic field this distribution will have a width of order $\mathcal{O}[0.5]mm$. In a wire TPC the PRF depends on the the induced signal from the motion of positive ions which is not limited to the pads directly below the electron charge distribution, thus increasing the width of the PRF.

In wire TPCs many of the positively charged ions drift back towards the cathode. While the electrons in an ionization track drift through the drift volume, ions which have been produced in previous events can still be present in the drift volume (drifting in the opposite direction) and can distort the ionization track. The GEM structures however, naturally suppress ion feedback, as the ions do not easily drift back through the GEMs. It has been shown that the ion feedback in a GEM TPC can be reduced to the order of 0.5% of the anode current[11], while in a wire TPC the ion feedback is not significantly reduced by the wires themselves, and needs to be dealt with by other means[2].

[2]For example with a gating grid.

3.3 High Voltage Supply

Each conducting surface of each GEM must have a different voltage supplied to it in order to obtain the desired electric fields throughout the amplification region. Due to the very high fields inside the holes of the GEM it is possible in some situations for debris to become lodged in the holes of a GEM and to conduct some current across the GEM, or for sparking to take place. The high voltage power supplies are equipped with over-current protection to ensure that the GEMs do not draw too much current. However, if the GEMs are powered by separate supplies, in the event of an over-current, a situation can arise in which only one high voltage supply powering the GEM trips while the other remains on. In this situation the GEM can have a very high potential across its two sides breaking down the dielectric in the center of the GEM, destroying it. For this reason it is crucial to power the GEMs using only one power supply. Our GEM high voltage supply uses a resistor voltage divider to select the ratios of the voltages across each GEM and the fields between each GEM. It also incorporates a shunt resistor with a floating voltmeter used to measure any current across the GEMs at the nano-amp scale. Also included are four monitor points which readout one one-thousandth of the voltage on each side of both GEMs (see figure 3.6 and table 3.1). In the event of an over-current trip the power is switched off to all the GEM surfaces simultaneously.

The nominal voltages at each output point are shown in table 3.2. Since the

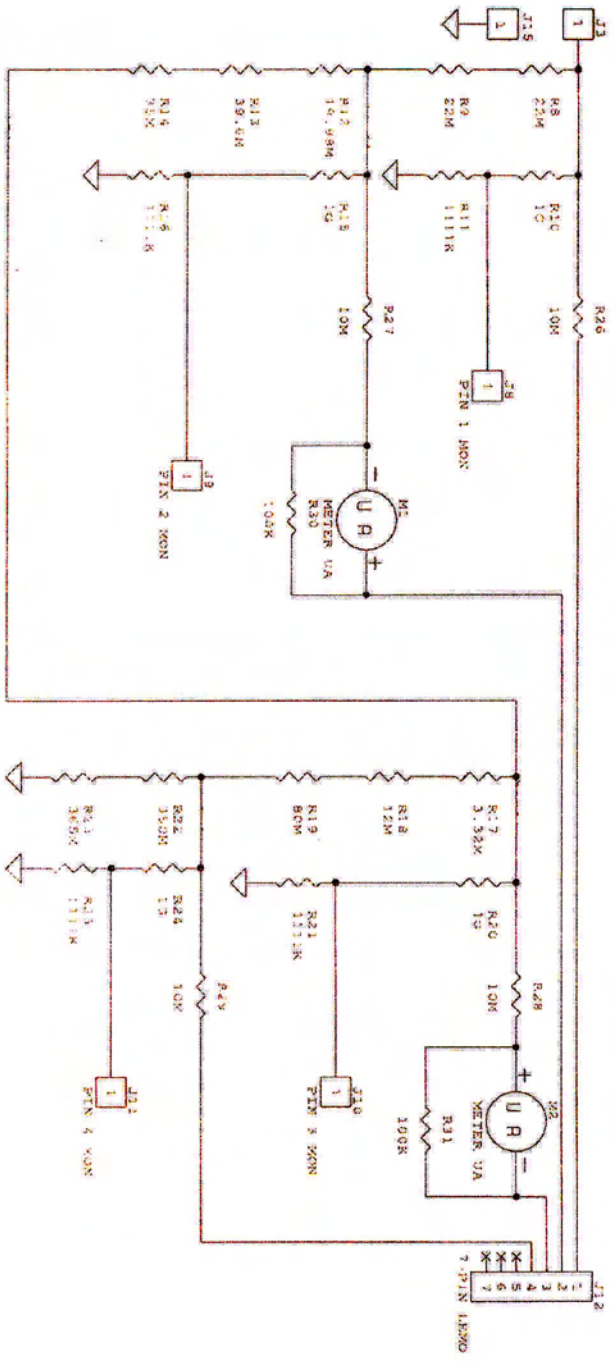

Figure 3.6: Circuit diagram of high voltage divider. See table 3.1 for GEM connections.

GEM part	HV output	1/1000 monitor output
Top first GEM	J12 (pin 1)	J8
Bottom first GEM	J12 (pin 2)	J9
Top second GEM	J12 (pin 3)	J10
Bottom second GEM	J12 (pin 4)	J11

Table 3.1: Important output locations

GEM part	Voltage [V]
Top first GEM	3150
Bottom first GEM	2750
Top second GEM	2150
Bottom second GEM	1750

Table 3.2: Nominal voltages.

circuit uses only one power supply the ratio of these voltages (and hence the ratio fields) is fixed. The pad array is at ground.

3.4 Readout

3.4.1 Pad Array

The electrons which exit the GEMs are collected on an array of gold plated pads on a printed circuit board. There are 256 individual pads which are isolated electronically from each other and from the surrounding area of the pad plane which is grounded (see figure 3.7). The pad array consists of eight rows of either 31 or 32 pads each. The pads in each row are staggered relative to the pads in the rows above and below them. There are three large pads which span the width of the array. These large pads are not used for track reconstruction but are useful in filtering data before writing to

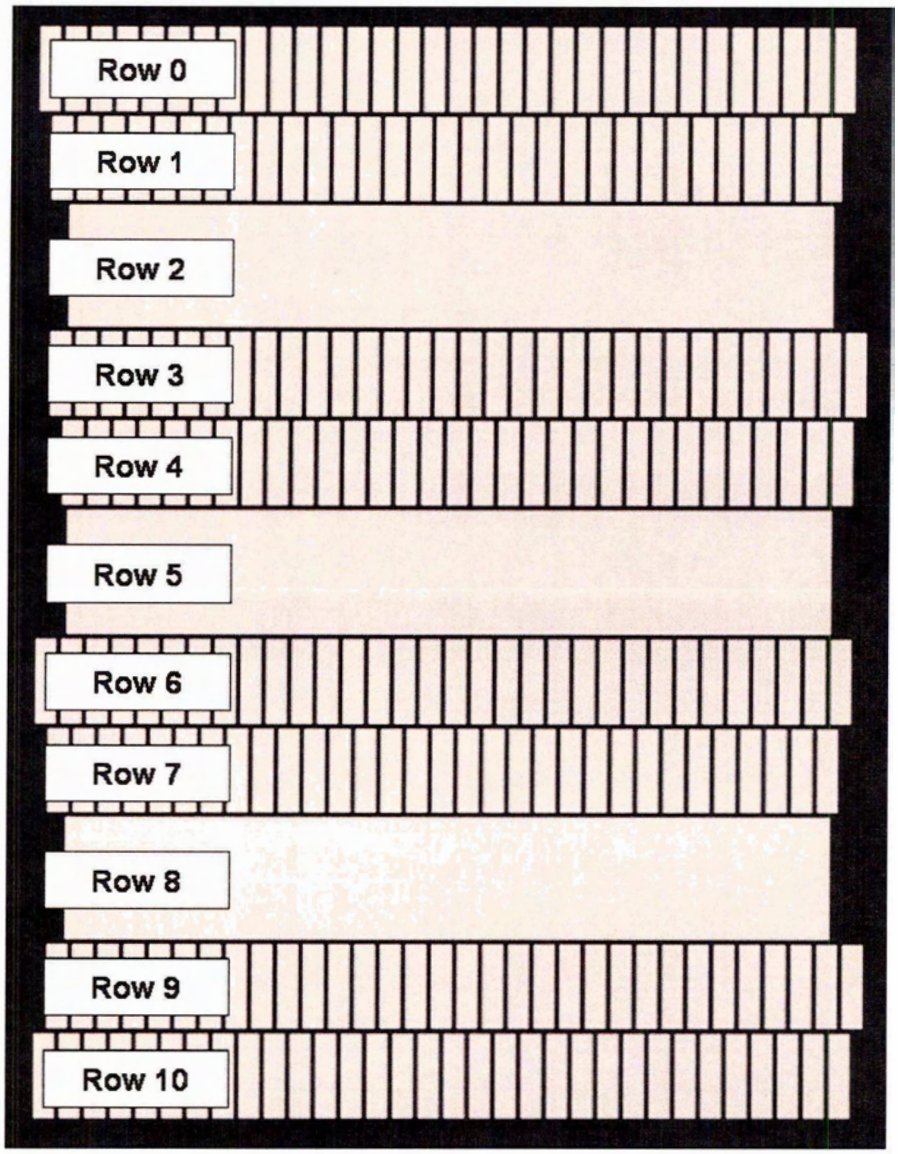

Figure 3.7: Schematic of one of two UVTPC pad arrays (2.0 mm wide pads)

disc (see section 3.5), for analyzing systematics and for making dE/dx measurements. The UVTPC has two readout pads boards which can be used. They differ only in the width of the pads, one array has pads which are $2.0\,mm$ wide $\times$ $7\,mm$ high, the other has $1.2\,mm \times 7\,mm$ pads. The pad rows are numbered from top to bottom (including the large pads as individual rows) from 0 to 10.

3.4.2 Electronics

The readout system is composed of eight front end electronics (FEE) cards with 32 channels each. Each FEE consists of 32 shaper and charge-sensitive pre-amplifiers and 32 pipelines of switched capacitor arrays (SCAs). When triggered, the SCAs store 512 samples of each channel with a sampling rate of 20 MHz. After the sampling is completed, the signals in the SCA are digitized and the data are sent to the readout motherboard which multiplexs the output from pairs of cards and sends the data to the data acquisition computer via 1.2Gbit/s fiber optic link. The data is received by the Rosie receiver board. Rosie uses a CVME964 VME Single Board Computer from Cyclone Microsystems which includes an Intel i960 processor, 32 MBytes of shared DRAM and 4 MBytes of private DRAM. Rosie can interface with an external PC via an ethernet link or to other VME modules via the VME backplane. Rosie's function is to receive the raw data from the mother board and store it temporarily until it is transferred to external permanent storage (such as a hard drive).

3.4.3 Pad Signals

The signals seen on the pads are caused by electrons being collected directly on a pad and the induced signal caused by the motion of the electrons in the gap between the last GEM and the pads. Pads which directly collect electrons have a substantially different pulse shape than pads which see only an induction pulse. Figure 3.8 shows typical pulses seen on three pads (after a pedestal correction has been applied) as readout by the SCAs after shaping. The x and y axes show the collection time (in 50 ns time bins) and the number of ADC counts respectively. The signals seen in figures 3.8A and 3.8B show the signals seen on pads which have directly collect electrons. The signal seen in figure 3.8C is due to only the induced signal from the motion of the charge in the induction gap. In order to fit the data to a Gaussian PRF the induction signals are canceled by summing over the positive and negative values of this bipolar signal.

3.5 Data Acquisition System

The data acquisition system uses the Rosie temporary receiver card, a Strucke SIS3100 fiber optic VME controller and a Linux PC. The DAQ software (written primarily by the author) consists of two C programs running simultaneously (one on Rosie's CPU and one on the Linux PC). Upon initialization the PC and Rosie establish an NFS connection via an ethernet link. A connection is also made between the PC and the VME controller via a fibre optic link. A block of memory, called the *status memory*

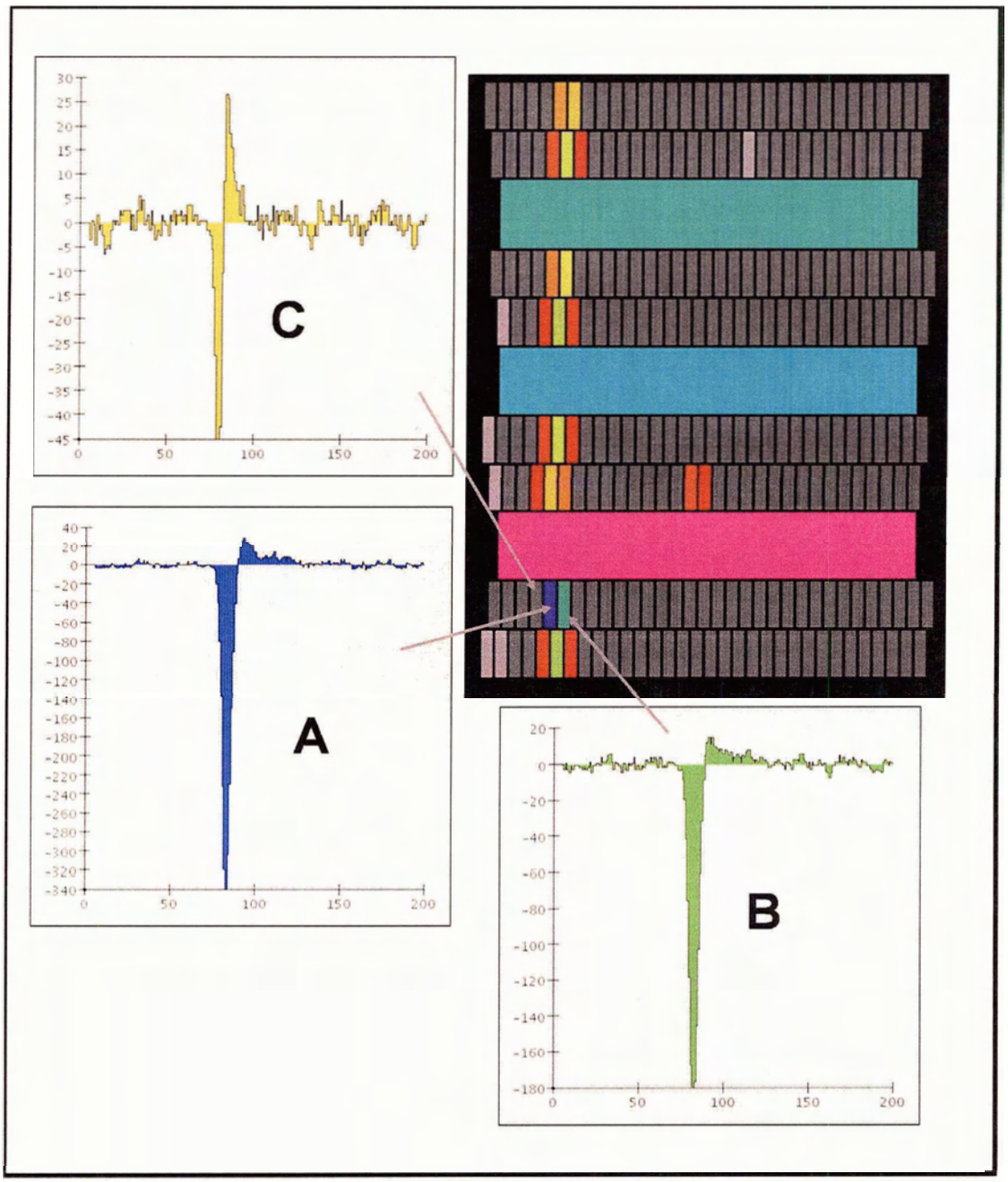

Figure 3.8: Typical signal seen on three pads. Figure A and B show pads which directly collect electrons. Figure C shows the signal on a pad which has only an induced pulse from the motion of the charge in the induction gap.

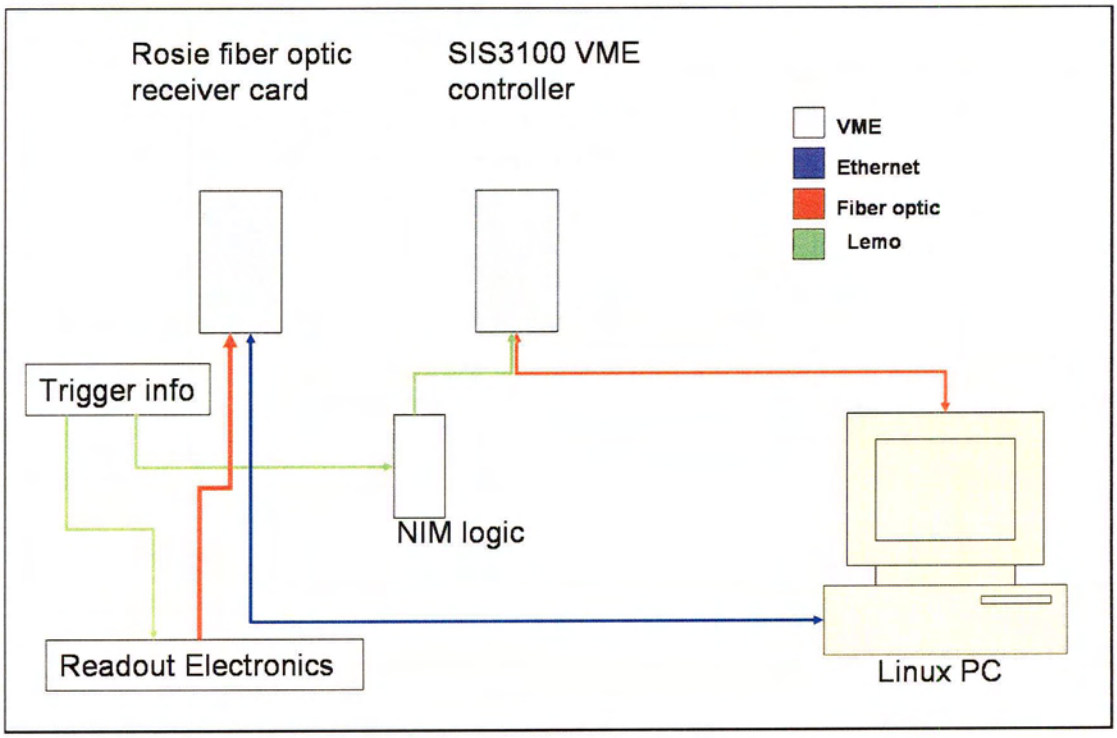

Figure 3.9: Schematic of the data acquisition system.

(which is visible to Rosie) is allocated on the PC which is used to hold a 16 bit status register (table 3.3) and the address of a block of memory which is allocated in Rosie's memory space and can be seen in the VME back plane (called the *copy memory*).

The DAQ system was designed to write data events that are associated with cosmic rays and data events that are associated with laser beam tracks to separate files. The distinction is made after a trigger is received using NIM logic. Once a trigger is received the raw data are written to Rosie's private memory and then copied to the copy memory. Once the data have been copied they are accessed by the PC through the VME back plane via the VME controller and written to disk on the PC. The copy memory is then freed, a new copy memory block is allocated and the address of this block is updated in the status memory. Each event written to disc includes: an event number, a time stamp, a bit to signify whether the event is a cosmic or laser event, and the digitized raw data. The system is capable of writing events to disc at a rate of approximately 3 Hz. Before any event is written to disc a check is done to see if a pulse is visible on the large pads of the pad array. If there is no pulse seen then it is assumed that there is no useful track and the event is discarded.

3.6 UVTPC Parameters

There are several parameters that can be changed in the operation of the UVTPC. We will discuss the choice of electric and magnetic fields, the choice of gas and the actual geometry of the TPC components. The overall goal of varying the operating param-

Bit	Name	Description
0	ROSIEBUSY	high when Rosie busy
1	SIS3100BUSY	high when SIS3100 busy
2	LASEREVENT	high when event is from laser trigger
3	CRUNFINISHED	high when cosmic data run is finished
4	LRUNFINISHED	high when cosmic data run is finished
5	STARTNEWLASERRUN	high when new laser data run is ready to start
6	WRITECOSMICDATA	high when data from cosmic event is ready to write to disc
7	WRITECOSMICDATA	high when data from laser event is ready to write to disc
8	FILTERED	high when event filtering is on to check for hits before writing data
9	free	free
10	free	free
11	free	free
12	free	free
13	free	free
14	free	free
15	free	free

Table 3.3: Use of status register bits

eters is to optimize the spatial resolution measurement capabilities of the chamber. To achieve this, it is necessary to keep the electron distribution intact throughout the drift but also to be able to accurately estimate the centre of the charge distribution in the readout plane, which can be competing goals. If we ignore the method for collecting the charge on the endplate for the moment, the smaller the transverse diffusion of the electron clouds in the drift volume, the more accurately we can estimate the original track parameters since this would keep the track in the same configuration as when the ionization took place. If the pads were much narrower than the intrinsic track width then we would only concern ourselves with keeping the electron cloud as narrow as possible. However, we do have a finite pad size. When the track fit is done, the fitting software uses the information from all the pads in a row that have a pulse seen on them. As the track narrows the number of pads with a hit decreases. If many pads in a row are hit, then there are more points to fit to the pad response function, greatly improving our resolution. This is not possible, however, for a realistic large scale TPC. If the charge distribution is so narrow that it is typically sampled by only a single pad in each row, there is a significant loss of information and the track parameter estimation degrades. The solution is to choose operating conditions and TPC geometry in such a way as to keep the transverse diffusion low in the drift volume but to spread out the charge in the transverse direction after amplification and before it is collected on the pads.[3] With a very low diffusion in drift volume we

[3]The staggered pad geometry is also important so that narrow tracks in the center of a pad which do not share charge with adjacent pads will be located between two pads in the rows above and

also gain the advantage of having very little degradation of resolution with increased drift distances, as the width of the electron distribution does not increase appreciably over the drift distance. We choose a gas with the following properties:

1. Very low transverse diffusion in a magnetic field: This allows for the track to maintain the same width throughout the drift volume.

2. High drift velocity: This allows for the chamber to clear the ionization quickly and is also the main factor in having a low diffusion in a magnetic field since the force on a moving charged particle from a magnetic field is proportional to the magnitude of the particle's velocity.

3. Low operating electric fields: These gases have the desired properties at a low electric field which reduces the need for very high cathode voltages.

4. Insignificant electron attachment and appreciable gains at high electric fields.

The two gases which are used in our tests which fit the above criteria are: argon:methane:CO_2 93:5:2 (we will call this TDR gas) and argon:methane 95:5[4] (we will call this P5 gas).

We choose the field in the drift volume to maximize drift velocity and keep the diffusion small. However, we still need to spread the charge out over multiple pads. The GEMs can be put an arbitrary distance from the readout end plane. Consider

below it, ensuring charge sharing.

[4]argon:methane 90:10 (P10) would perform slightly better than P5 however due to its modest flammable nature it was not possible for it to be used in our tests at DESY.

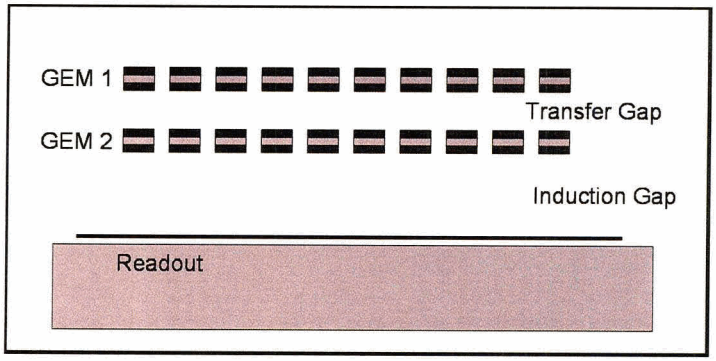

Figure 3.10: Schematic of GEM and readout setup

two regions between the end of the drift volume and the readout plane: the transfer gap (the region between the GEMs) and the induction gap (the region between the last GEM and the readout plane (see figure 3.10). The electric fields in these regions are chosen at a value such that the diffusion is much larger than in the drift volume and the width of the induction gap is chosen to allow enough distance for the charge distribution to disperse. The transfer and induction gaps have a width of $2.5\,mm$ and $5\,mm$ respectively with nominal electric field strengths of $2400\,V/cm$ and $3500\,V/cm$ respectively. This then "defocuses" the electron cloud just before hitting the readout pads, thus spreading the charge over many pads (see figure 3.11).

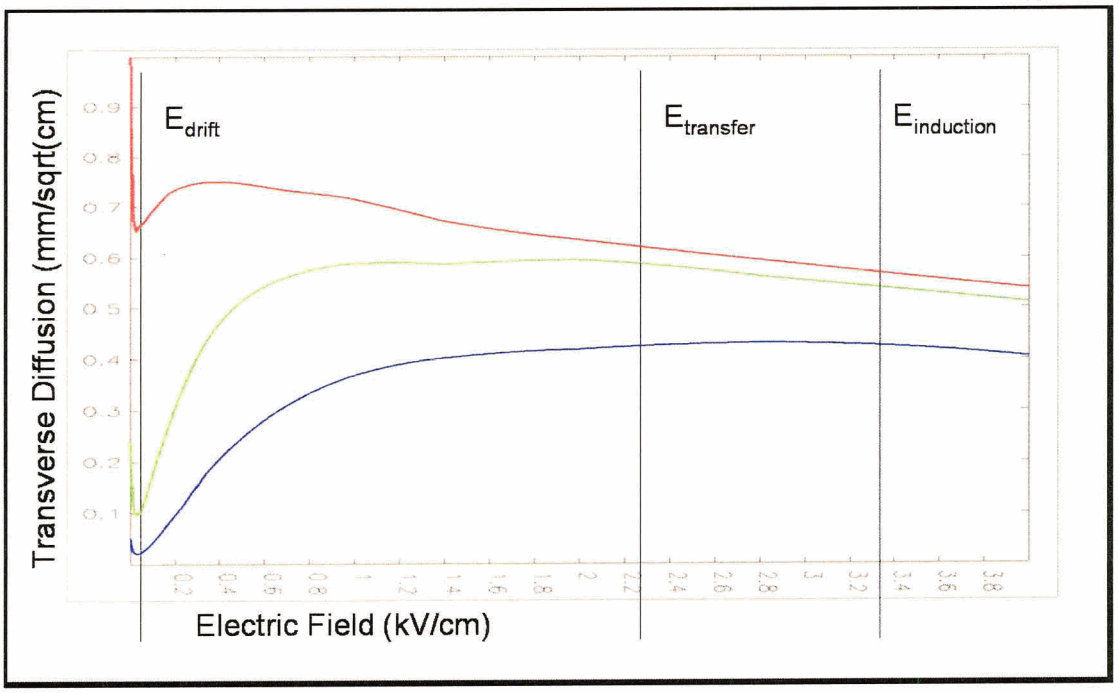

Figure 3.11: Example of electric field choice at 93% of the nominal fields in the amplification and readout regions. This plot shows P5 (argon:methane 95:5) gas. Red, green and blue lines correspond the magnetic fields of 0,1,5T respectively.

Chapter 4

Description of Tests

The data for this analysis were acquired at DESY (Deutschen Elektronen Sychrotron), a particle physics laboratory in Hamburg, Germany. During these tests the TPC was inserted into a super-conducting solenoid which is capable of producing magnetic fields up to 5.2 tesla. The controllable parameters for our tests were choice of gas, electric and magnetic field intensities and choice of pad widths ($2.0\,mm$ and $1.2\,mm$).

The tests which quantify the resolution capabilities of our detector use cosmic ray tracks. We divide these data into 12 data sets based on the operating parameters which were chosen. The data set names include: gas type, magnetic field strength, an indication of whether the wide ($2\,mm$) or the narrow ($1.2\,mm$) pads were used, and indicator if the data set is a Monte Carlo simulation (MC) data set. For example, data set tdrB2n has "tdr" indicating that it was TDR gas, "B2" indicating a 2 tesla magnetic field and "n" indicating the narrow pads were used. The corresponding MC data set would be called tdrB2nMC. Table 4.1 lists all the data sets analyzed.

For all data sets the electric field in the transfer and induction gaps were

Data set name	B field [T]	Gas	Pad Width [mm]	data/MC	Drift Field [V/cm]
p5B4w	4.0	"P5"	2.0	data	160
p5B4wMC	4.0	"P5"	2.0	MC	160
p5B4n	4.0	P5	1.2	data	90
p5B4nMC	4.0	P5	1.2	MC	90
tdrB4w	4.0	TDR	2.0	data	230
tdrB4wMC	4.0	TDR	2.0	MC	230
tdrB4n	4.0	TDR	1.2	data	230
tdrB4nMC	4.0	TDR	1.2	MC	230
tdrB1n	1.0	TDR	1.2	data	230
tdrB1nMC	1.0	TDR	1.2	MC	230
tdrB0n	0.0	TDR	1.2	data	230
tdrB0nMC	0.0	TDR	1.2	MC	230

Table 4.1: List of data sets to be analyzed.

2232 V/cm and 3255 V/cm respectively. The voltage across each GEM was 372 V.

Our experimental setup also included an ultra-violet laser beam system which was capable of producing straight ionization tracks in the chamber. The position of this beam was controllable in the x and z directions. Some data sets which were acquired using laser tracks are used in the analysis. When this is the case it will be made clear that the data are from laser tracks.

Chapter 5

Analysis Methods

This chapter describes in detail the methods used to analyze our data. To illustrate the method we will show the details of the analysis on one data set (p5B4w). A summary of all the results and a detailed discussion will be found in the following chapters.

5.1 Analysis and Simulation Software

Our analysis software is a java-based object oriented package (written by Dean Karlen) which is used for our data simulation as well as data analysis. The MC reads in a file which has been generated by GEANT3. The GEANT3 simulation produces a simulated initial ionization track from a cosmic ray. The simulation then propagates the charge through the drift volume giving it a Gaussian spread in the x,y and z directions based on diffusion constants which are inputs in the simulation. Once the electron clouds arrive at the first GEM, each electron is propagated through a GEM hole and the number of electrons exiting the GEM is found by choosing a

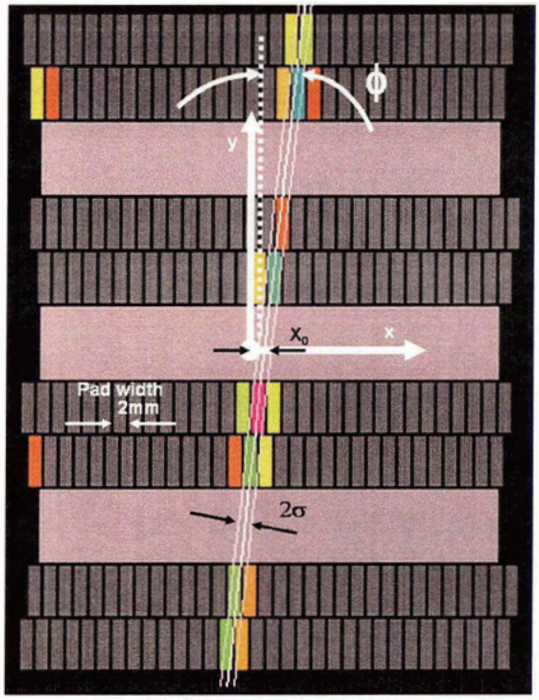

Figure 5.1: Example of fitted track with fit parameters labeled.

random number from an exponential distribution with a mean equal to the GEM gain (the GEM gain is also an input parameter to the MC). The transfer and induction gaps and the second GEM use the same methods as the drift volume and the first GEM respectively. The charge is than assigned to a readout pad based on its position. Finally, a function which simulates the electronic shaping is scaled to the number of electrons arriving on each pad. The output is then put into the same digital form as the real data and can be analyzed with the same analysis software as the real data.

In order to reconstruct the track in the transverse plane from the raw data (either real or simulated) we must first assign a number of electrons to each pad based on the digitized signal on that pad. First, the pedestal for each channel is calculated

by averaging the signal in the last several time bins, and the data is shifted by this amount. For the pads in a row, the signals in the pads are combined and the time bin with the largest signal is taken to be the arrival time of the ionization. For each pad in the row, the ADC values are summed from three time bins before the peak to three bins after the peak. This number is then divided by the number of ADC counts per electron (this value is known for our electronics) to convert it into the number of electrons on that pad. A threshold value is chosen for the minimum number of electrons on a pad, any pad with less than this threshold is assumed to have no signal and assigned zero electrons. The number of electrons on all of the pads is then used to perform a four parameter track fit. The four parameters are (see figure 5.1):

x_0 , the track's horizontal position from the centre of the pad array.

ϕ , the angle from vertical of the track at the centre of the pad array.

σ , the width of the track (this is defined by the standard deviation of a Gaussian which is fit to pad signals).

$1/R$, the inverse of the radius of curvature of the track.

The track fitting software performs a maximum likelihood fit to the data in all the rows simultaneously assuming the pad response function is Gaussian and that the curvature and width of the track is constant. The fit is seeded by using a straight track with a width of $1\,mm$. This seed track is chosen as a straight line which passes through the center of the pads with the largest signal on the two outside rows.

To perform a fit in the longitudinal direction, the arrival time information for each row is used in a linear fit. This is parameterized by z_0, the drift time of the center of the track (center in the y-direction) and the tangent of the angle of the track in the y-z plane, $\tan \lambda = dz/dy$. Since the drift velocity is not known prior to the analysis, the quantity $\Lambda = \Delta$ z [time bins] / Δ y [mm] is used instead.

5.2 Bad Channels and Cuts

In some instances a small number of the electronics channels become noisy, fail or display erratic behaviour. This can corrupt the reconstruction of tracks. To check for this we choose a random time slice in the data for each channel in each event. The number of electrons which would be attributed to the signal in that time slice is calculated. If a channel has more than 4000 electrons or less than 100 electrons in this time slice for more than 10% of the events in a run then that channel is subsequently turned off for the analysis of that run. In total three channels were turned off for all runs and no more than one additional channel was turned off in specific runs.

Cuts on the following variables are applied:

x_0 : A cut on x_0 is made to ensure that tracks located close to the edge of the pad array which deposit some charge in the area next to the pad array are not included in the analysis, see figure 5.3.

errx_0 : A cut on the error in x_0 is made. This cut is loose enough to only exclude fits

which were not made to real tracks, but rather to noise pulses, see figure 5.4.

ϕ : A cut on ϕ is made to include only tracks which are fairly vertical, see figure 5.5.

σ : A cut on σ is made to exclude events in which a very large signal is collected on some pads which is out of the dynamic range of the electronics. These events are characterized by a very large σ, see figure 5.2 and 5.6.

errσ : Like the cut on the error on x_0 this is to remove events where tracks were fit to noise, see figure 5.7

z_0 : A cut on z_0 is made to remove any tracks in the first few time bins (due to electronic problems) and to remove tracks whose drift time implies that they started outside of the chamber, see figure 5.8.

Λ :A cut on Λ is made to select tracks which are close to vertical in the y-z plane, see figure 5.9.

#clus :Two dimensional boxes are made in the x-z direction. If there are a number of electron above a threshold in one of these boxes it is considered a cluster. A cut is made on this quantity to ensure that there is one track per row and that large noise pulses are not present.

stat :There is a status bit assigned in the analysis which is set to 1 if any of the fits fail. It is otherwise set to 0. A cut is made on this to ensure no failed fits.

Cut	See figure
$\|x_0\| < 24mm$	5.3
error in $x_0 < 0.2mm$	5.4
$\|\phi\| < 0.1rad$	5.5
$0.15mm < \sigma < 1.0mm$	5.6
error in $\sigma < 0.2mm$	5.7
$10tb < z_0 < 150tb$	5.8
$\|\Lambda\| < 0.3\frac{tb}{cm}$	5.9

Table 5.1: Cuts used in analysis of data set p5b4 (tb refers to time bins).

Table 5.1 shows the specific cuts which have been applied to the data set p5B4w.

5.3 Drift Velocity, Diffusion and Defocusing

The UV laser was used to calculate the drift velocity for a data set. One run was taken at a fixed drift distance. The laser beam position in the z-direction was changed by a known amount and another laser data set was taken. Figure 5.10 shows two laser runs taken close to the time data set p5B4w was taken. The drift distances for the two runs differ by $100 \pm 2\,mm$ [1]. Figure 5.11 shows that the drift time varies very little (less than 0.3 time bins) during the 10 minute runs.

Calculation of drift velocity:

Let z be the drift distance of the first run and $z + 100$ be the drift distance of the second run. Let t_1 and t_2 be the drift times and let v_d be the drift velocity (tb refers to units of 50 ns time bins).

[1] Uncertainty in change of position was estimated from tests with the laser beam delivery system.

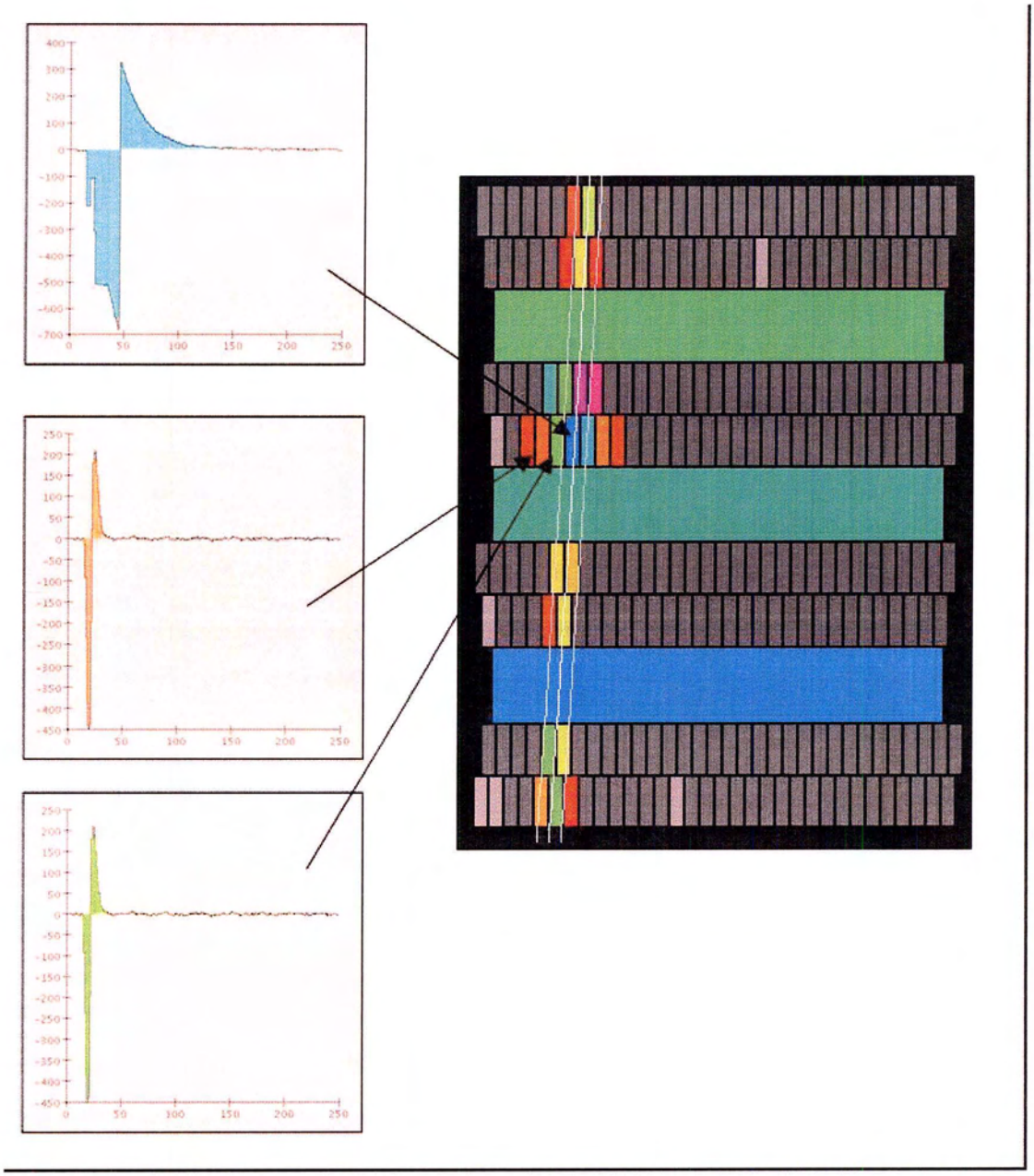

Figure 5.2: Event display showing a very large signal which is out of the dynamic range of the electronics. This is characterized by a large sigma.

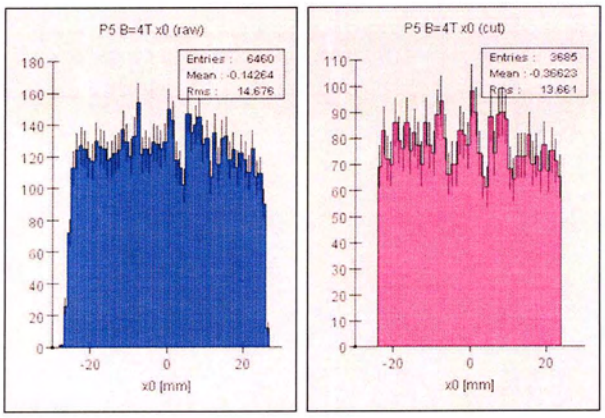

Figure 5.3: x_0 raw and cut for data run p5b4.

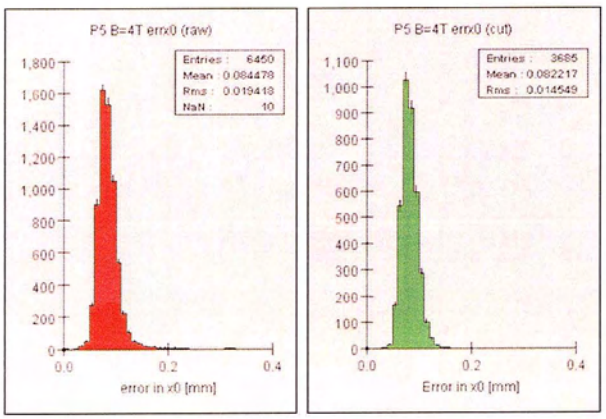

Figure 5.4: error in x_0 raw and cut for data run p5b4.

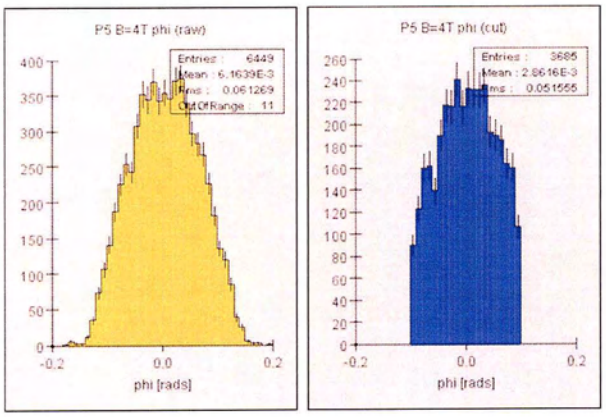

Figure 5.5: ϕ raw and cut for data run p5b4.

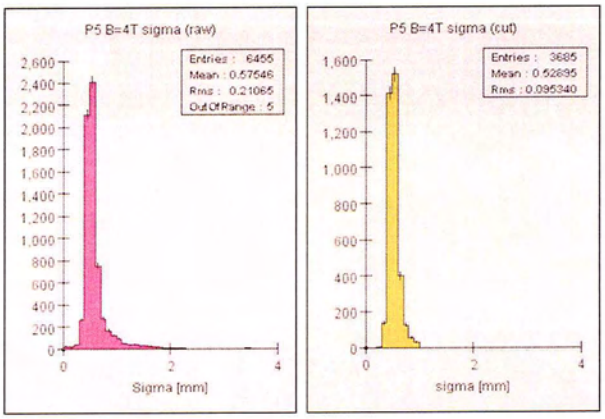

Figure 5.6: σ raw and cut for data run p5b4.

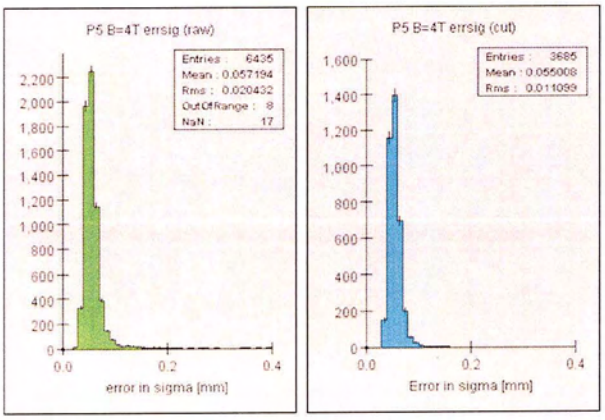

Figure 5.7: Error in σ raw and cut for data run p5b4.

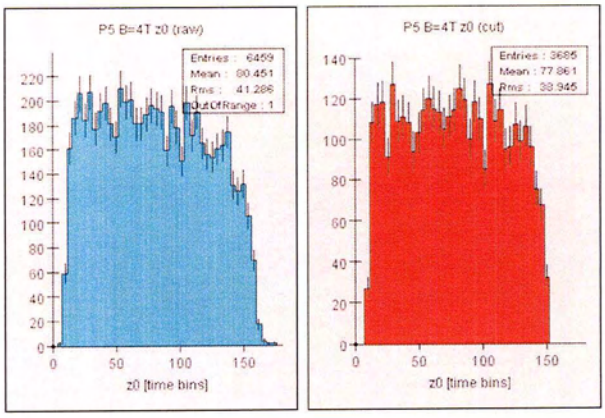

Figure 5.8: z_0 raw and cut for data run p5b4.

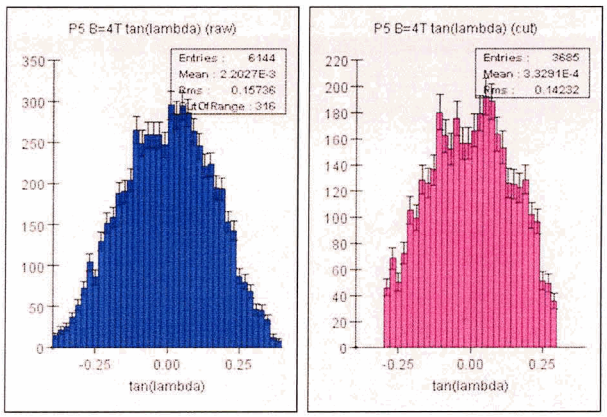

Figure 5.9: Λ raw and cut for data run p5b4.

$$t_1 = 56.57 \pm 0.02\, tb \times \frac{50ns}{tb} = 2.829 \pm 0.001\, \mu s \tag{5.1}$$

$$t_2 = 108.67 \pm 0.02tb \times \frac{50ns}{tb} = 5.434 \pm 0.001\, \mu s \tag{5.2}$$

$$v_d = \frac{(z + 100mm) - z}{t_2 - t_1} = \frac{100 \pm 2\, mm}{2.605 \pm 0.0014\, \mu s} \tag{5.3}$$

$$v_d = 3.839 \pm 0.077\, \frac{cm}{\mu s} \tag{5.4}$$

Calculation of diffusion:

Now, from section 2.4.2 we see that $\sigma^2 = {D_t}^2 t$. Therefore a plot of σ^2 vs. z_0 (measured in time bins) should give a slope of D_t^2 in units of $(\frac{mm^2}{tb})$. Dividing this by the drift velocity in units of $\frac{mm}{tb}$ and taking the square root gives us the diffusion constant.

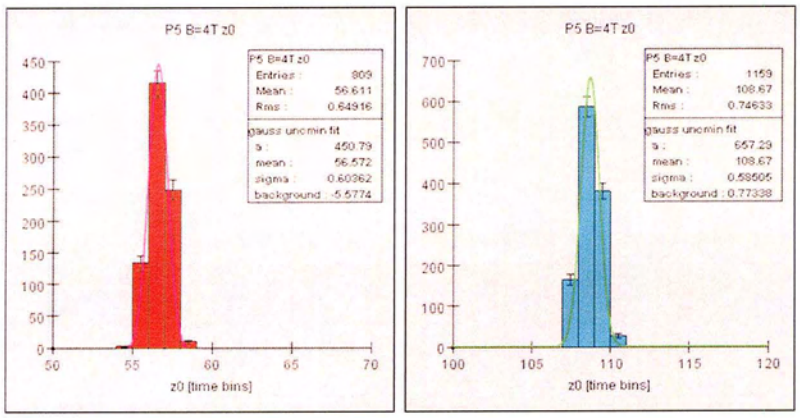

Figure 5.10: Histograms of drift time for two laser runs with a drift separation of 100mm

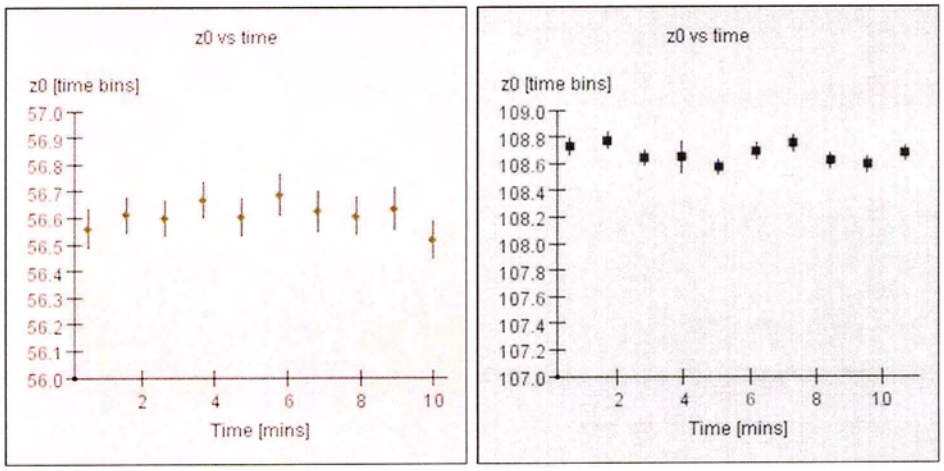

Figure 5.11: Drift time vs. real time plots. Shows little variation of drift time for these laser runs.

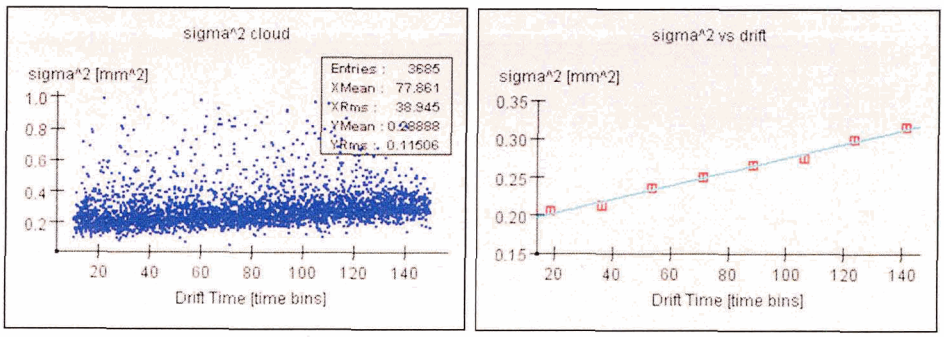

Figure 5.12: Left: Scatter plot of σ^2 vs. drift distance. Right: Plot of σ^2 vs. drift distance. The data have been binned according to drift time and histogrammed, the points are the means of Gaussians which have been fit to the histograms.

Notice that figure 5.12 shows a non-zero y-intercept, implying that tracks with zero drift have a finite width. Zero drift distance is defined as a track which starts directly in front of the first GEM. The width of these tracks is due to diffusion which occurs between the first GEM and the readout pads. We define this width for zero drift distance as the "defocusing", ie: the inherent spreading of the charge distribution through the readout.

In figure 5.12 the plot on the righthand side has a slope of $9.09 \times 10^{-4} \frac{mm^2}{tb}$, the drift velocity (from above) is $1.920 \frac{mm}{tb}$ giving

$$D_t = \sqrt{\frac{9.09 \times 10^{-4} \frac{mm^2}{tb}}{1.920 \frac{mm}{tb}}} = 4.734 \; mm^{\frac{1}{2}} \; . \tag{5.5}$$

This quantity is more commonly expressed as amount of diffusion per $\sqrt{cm}$, so we get

$$D_t = (68.7 \pm 3.7) \frac{\mu m}{\sqrt{cm}} \tag{5.6}$$

where the error comes from the statistical error in the slope of σ^2 vs. drift and the error in the drift velocity measurement.

The defocusing constant is the square root of the y-intercept of righthand plot in figure 5.12. In this example the y-intercept is at $0.1843\, mm^2$ which gives us:

$$defocusing = (429.3 \pm 2.1)\, \mu m \tag{5.7}$$

5.4 Resolution

5.4.1 Quantifying Resolution

In order to achieve the momentum resolution goal for the central tracker at the linear collider it is necessary to obtain excellent spatial resolution for each point sampled. However, when conducting tests using cosmic ray tracks we do not know the location of the ionization track a priori. Therefore it is not trivial to quantify the spatial resolution of our detector. The method which we use is as follows:

1. A standard four parameter track fit is done using the information in all pad rows. This is called the *reference track.*

2. One row is chosen for a resolution measurement (*resolution row*). The track fit is repeated using only the information from the resolution row and with σ, ϕ

and $\frac{1}{R}$ fixed to the values obtained from the reference track fit. This leaves only x_0 free in the fit.

3. The difference between the x_0 in the reference track and the x_0 in the resolution row fit is taken. This value is called the residual (δx_i), where i indicates that the resolution row is included in the reference track fit.

4. The same procedure is repeated using only the information from the rows which are not the resolution row (seven other rows) when performing the reference track fit. The residuals from this method we will call δx.

5. The δx_i and δx distributions are histogrammed and fit with Gaussian functions.

6. We call the standard deviations of the two Gaussians $\sigma_{\delta x_i}$ and $\sigma_{\delta x}$ and define the resolution for that row as[12]:

$$resolution \equiv \epsilon = \sqrt{\sigma_{\delta x_i} \times \sigma_{\delta x}} \tag{5.8}$$

5.4.2 Resolution Measurement

Figure 5.13 shows the distribution of residuals for data set p5B4w fit to Gaussian distributions. The geometric mean of the width of the two Gaussian distributions in each plot is defined to be the resolution for that row, figure 5.14 shows the same thing for all rows simultaneously. We also define a quantity called a "bias" which is the mean of the Gaussian which has been fit to a residual distribution. For these analyses we will study all of the pad rows except for the two on the top and bottom

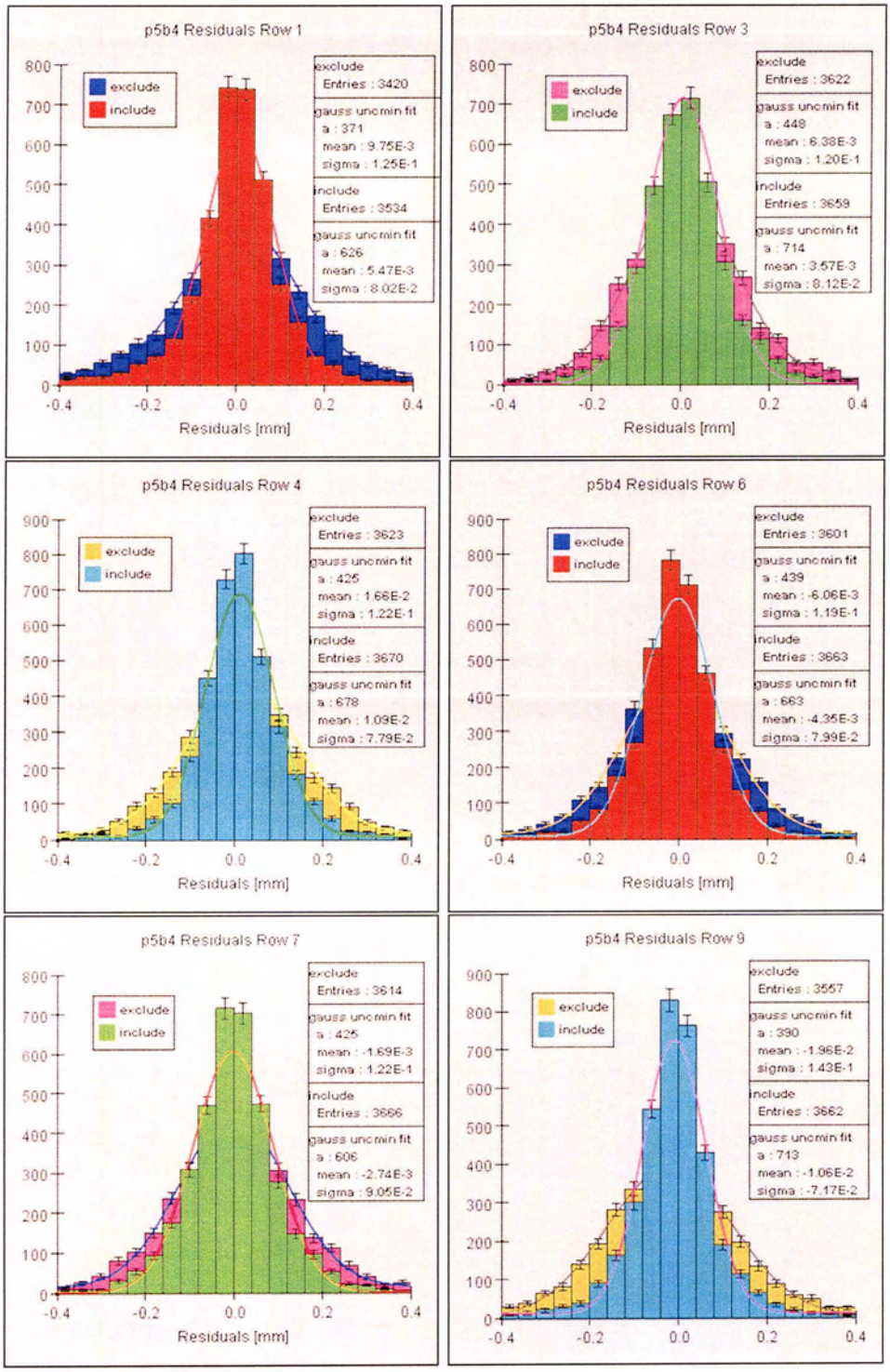

Figure 5.13: Row by row histograms of residual distributions. Each plot shows the residuals with the row included and excluded from the reference track fit.

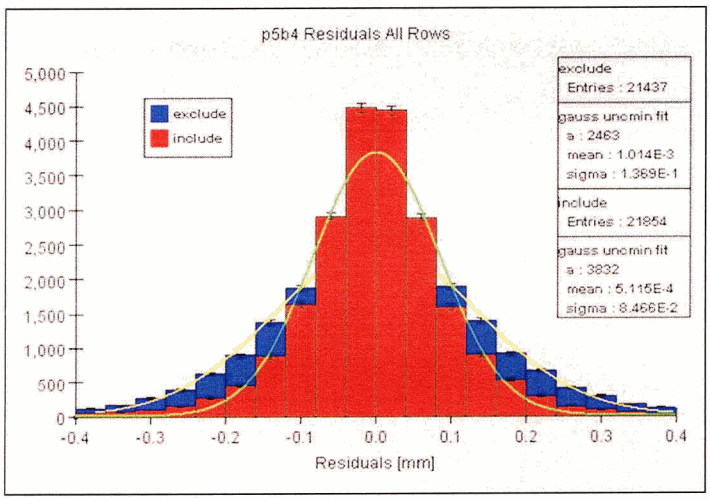

Figure 5.14: Histograms of residual distribution for all rows combined. Each plot shows the residuals with the row included and excluded from the reference track fit.

Row	Resolution [mm]	Bias (inc.) [mm]	Bias (ex.) [mm]
1	0.100	0.010	0.005
3	0.099	0.006	0.004
4	0.097	0.017	0.011
6	0.098	-0.006	-0.004
7	0.105	-0.002	-0.003
9	0.101	-0.020	-0.011
All rows	0.108	0.001	0.001

Table 5.2: Resolution and bias measurements for data set p5B4w (bias shown for reference track which includes and excludes the resolution row).

edges (ie: the rows studied will be 1,3,4,6,7,9). Table 5.2 shows the resolution and bias measurements for data set p5B4w.

In order to look for systematic problems in the data, we also choose to study the resolution and bias as a function of other variables in the analysis. In this case the data is binned with respect to the variable being studied. For each bin the resolution or bias is calculated and plotted versus the variable. We will consider the resolution

and bias as follows:

- Bias vs. x_0 see figure 5.15
- Bias vs. z_0 see figure 5.16
- Bias vs. position on the pad see figure 5.17
- Resolution vs. x_0 see figure 5.18
- Resolution vs. ϕ see figure 5.19
- Resolution vs. position on the pad $\equiv b$ see figure 5.20
- Resolution vs. z_0 see figure 5.21

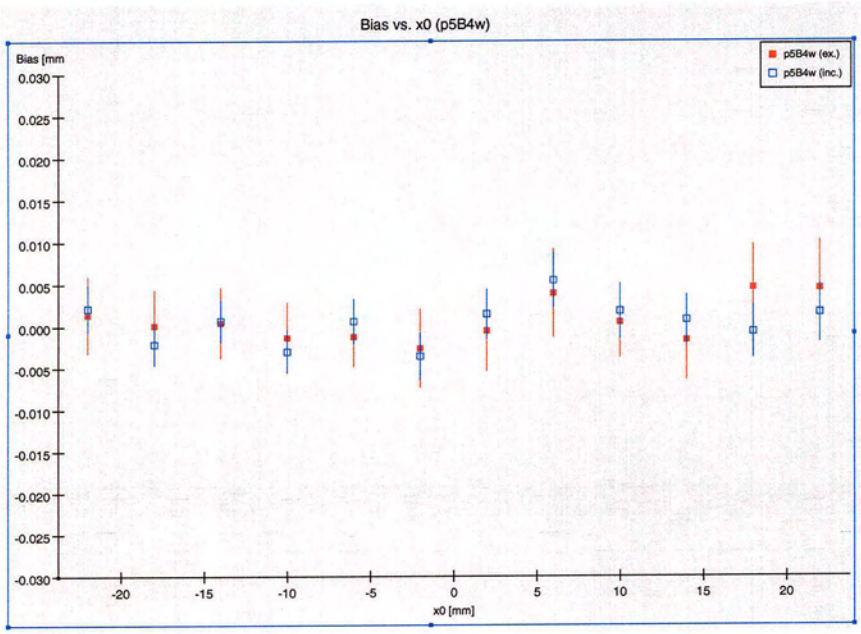

Figure 5.15: Bias versus x_0.

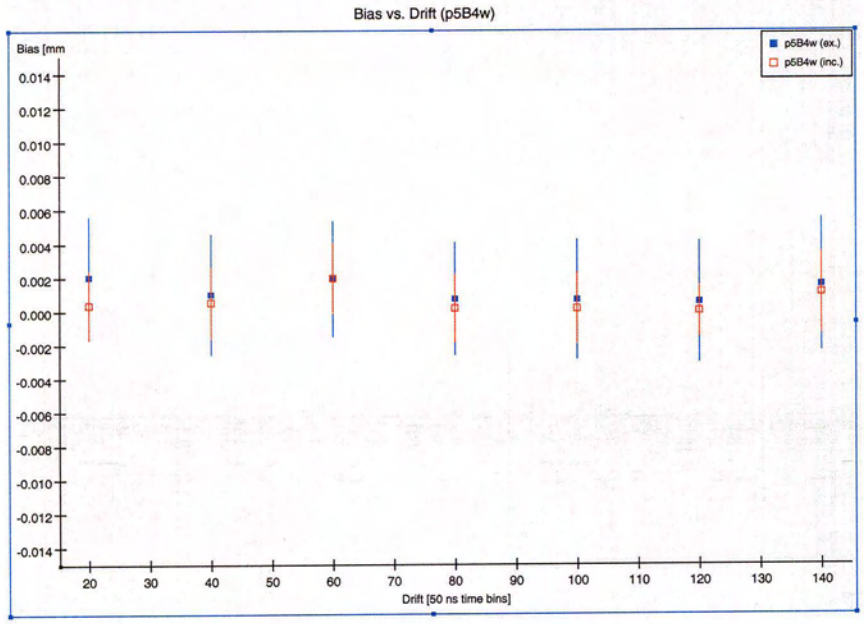

Figure 5.16: Bias versus z_0.

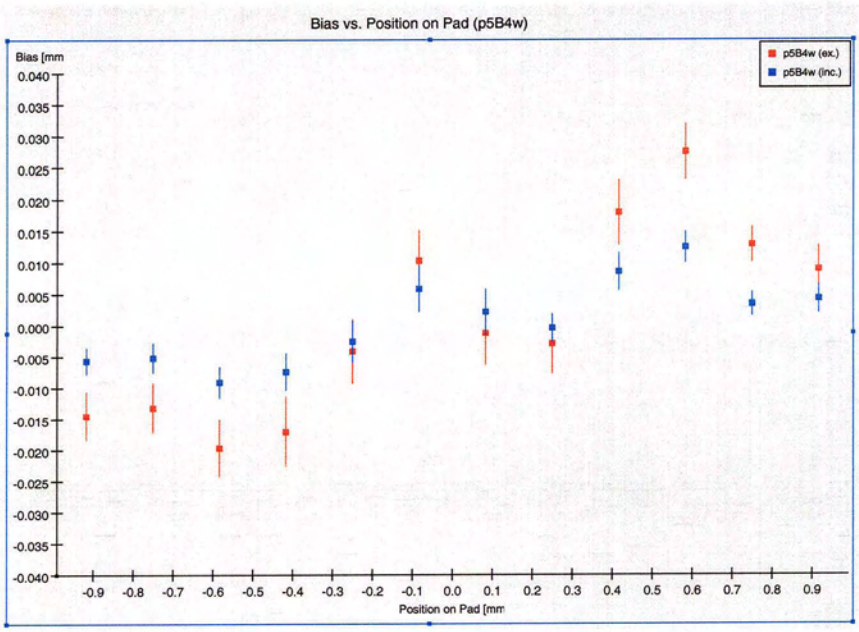

Figure 5.17: Bias versus position on the pad.

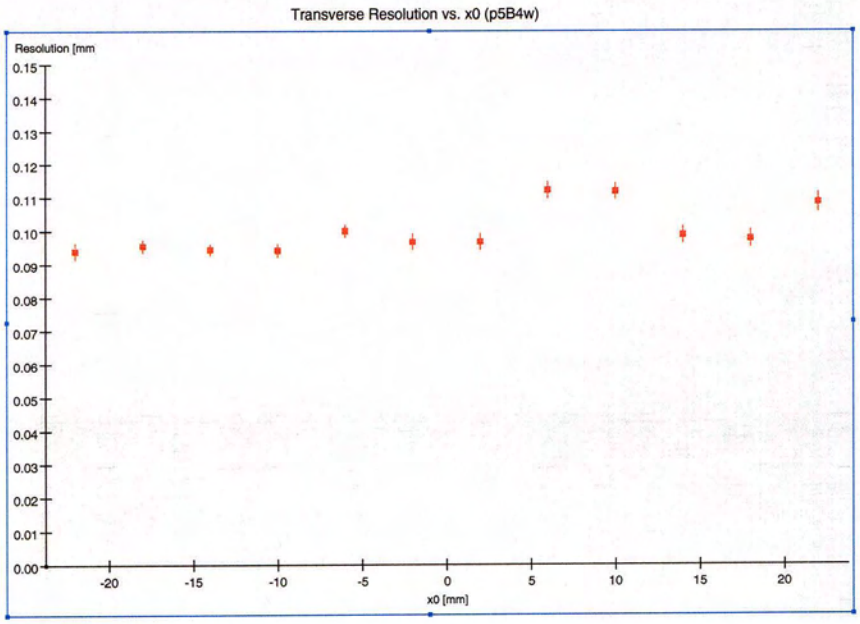

Figure 5.18: Transverse resolution versus x_0 for all rows.

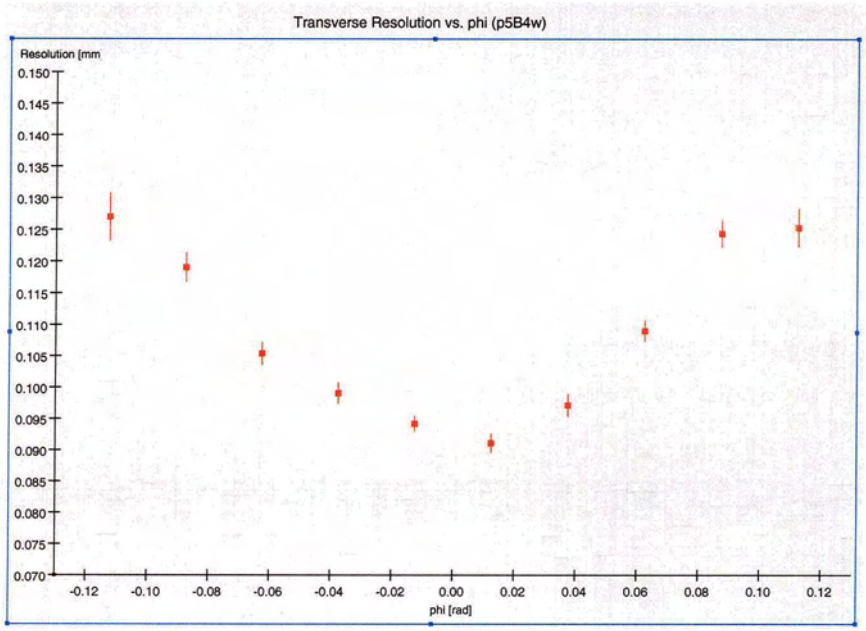

Figure 5.19: Transverse resolution versus ϕ for all rows.

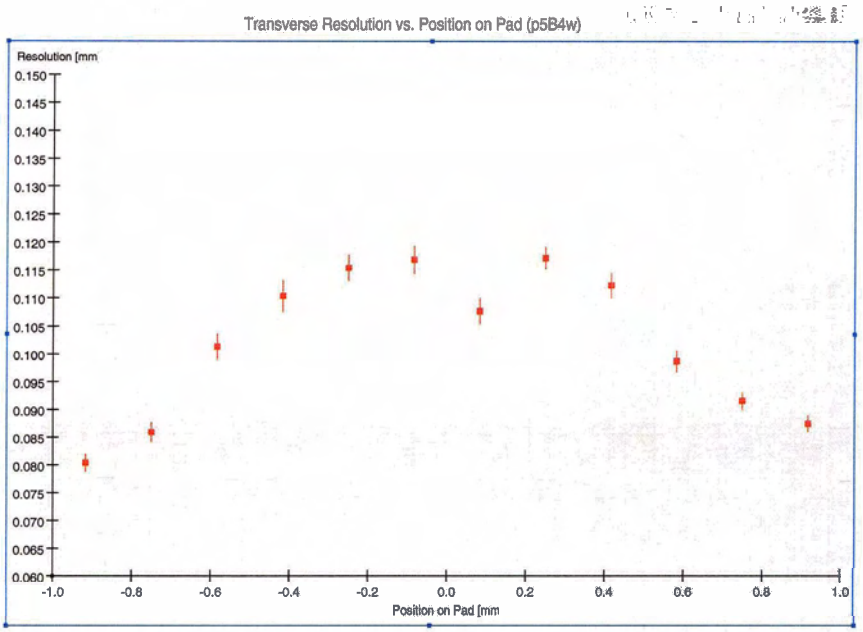

Figure 5.20: Transverse resolution versus position on pad for all rows.

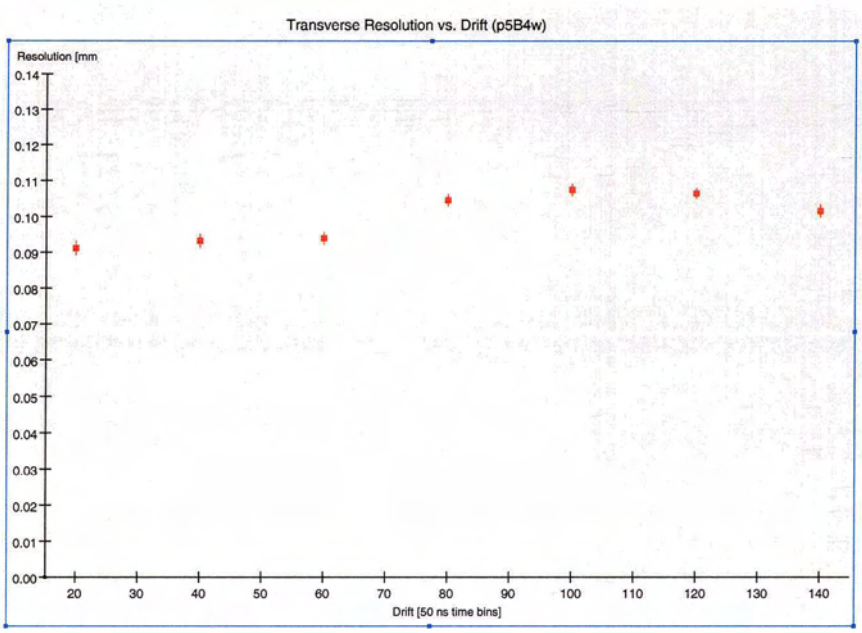

Figure 5.21: Transverse resolution versus z_0 for all rows.

Chapter 6

Results

6.1 Drift Velocity

Table 6.1 shows the measured drift velocities for all data sets. The expected drift velocities were also calculated using a simulation program called Magboltz. The TDR data are all in agreement with the Magboltz values to within 5%. The measured drift velocity for the p5B4n data set was within 7% of the Magboltz value. The data set p5B4w was the first data taken during the running time. The drift field was set to what should be the maximum drift velocity for P5 gas (90 V/cm), however the drift velocity was found to be much lower than expected. Some data runs were taken using the laser to measure the drift velocity as a function of electric field. These points are shown in figures 6.1 and 6.2. The maximum drift velocity was found to be at an electric field of 160 V/cm in the drift region. The drift velocity stayed stable throughout the data taking period of set p5B4w. After the data taking period it was found that the gas system which we were using is known to have water vapour in it for up to 2-3 weeks, after the gas flow has started. A Magboltz simulation

Data set	Drift Velocity (data) $\frac{cm}{\mu s}$	Drift Velocity (sim.) $\frac{cm}{\mu s}$	Drift Field $\frac{V}{cm}$
p5B4w	3.10 ± 0.062	4.140 ± 0.002	90
p5B4w	3.839 ± 0.077	3.639 ± 0.002	160
p5B4n	3.851 ± 0.039	4.140 ± 0.002	90
tdrB4w	4.511 ± 0.045	4.518 ± 0.002	230
tdrB4n	4.538 ± 0.060	4.518 ± 0.002	230
tdrB1n	4.655 ± 0.060	4.518 ± 0.002	230
tdrB0n	4.675 ± 0.060	4.518 ± 0.002	230

Table 6.1: Drift velocities (data and Magboltz simulation). Errors in the data are dominated by the uncertainty in the laser position.

shows that water added to P5 gas cannot account for the drift velocities seen (figure 6.1). However, the drift velocities could be consistent with water added to a mix of argon:methane 94:6 (see figure 6.2)[1]. The TDR gas mix is less sensitive to water in the gas. It is important to note that the diffusion and drift velocities were constant throughout each data set.

6.2 Diffusion and Defocusing

Figure 6.3 and 6.4 show σ^2 versus drift for all the data sets. Each set shows the expected linear behaviour. Using the methods outlined in the previous chapter the transverse diffusion constants and defocusing constants were found for all the data sets. When performing the analysis on the MC data sets we found that the estimated diffusion constant was consistently lower than the diffusion constant which was input to the MC. The analysis software takes an input parameter which is a probability that

[1]The gas mixtures provided at DESY are supposed to be much more accurate than this.

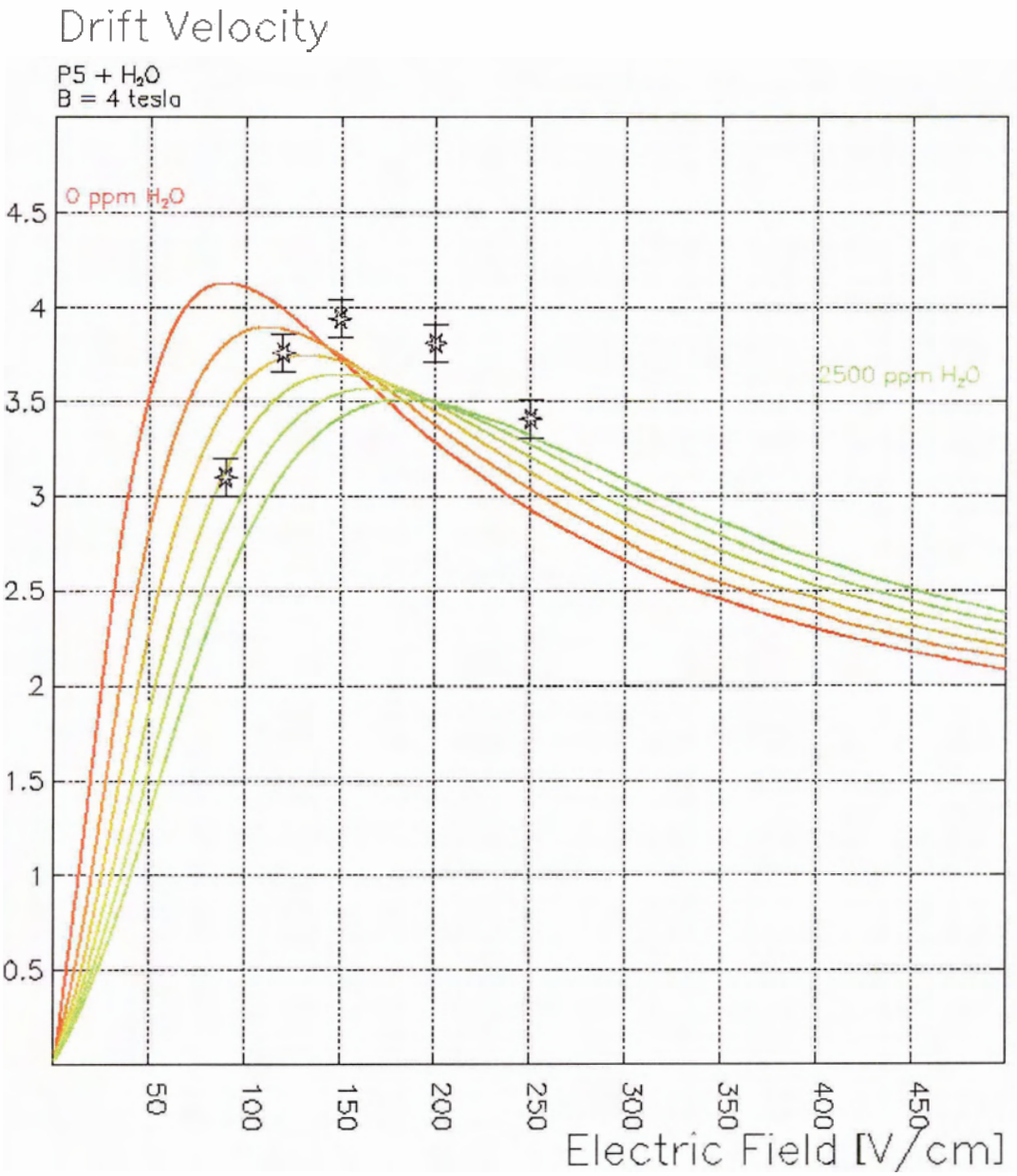

Figure 6.1: Drift velocity of P5 (Ar:CH_4 95:5) with water concentrations from 0 to 2500 ppm. Drift velocity measurements are overlaid.

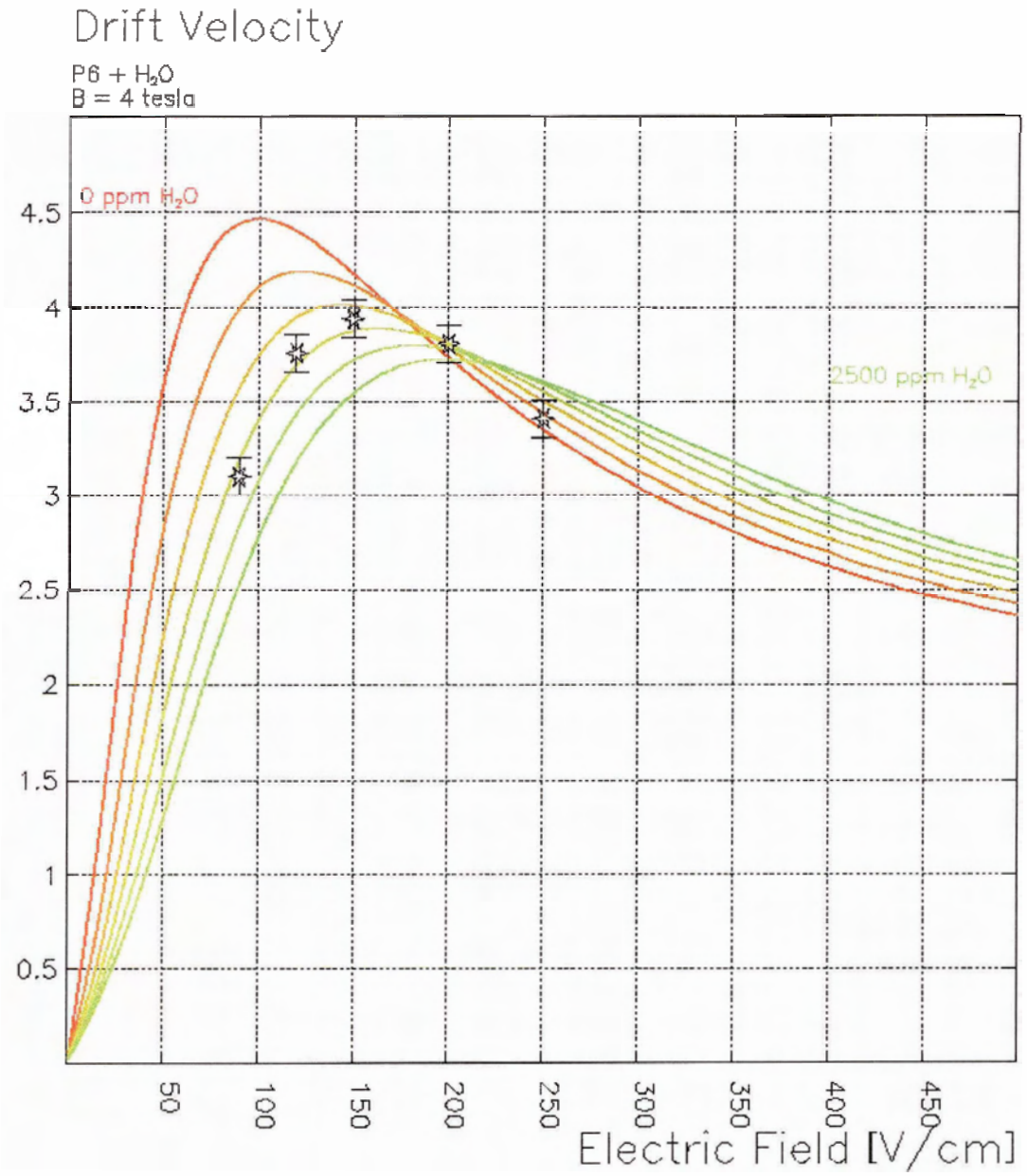

Figure 6.2: Drift velocity of P6 (Ar:CH_4 94:6) with water concentrations from 0 to 2500 ppm. Drift velocity measurements are overlaid.

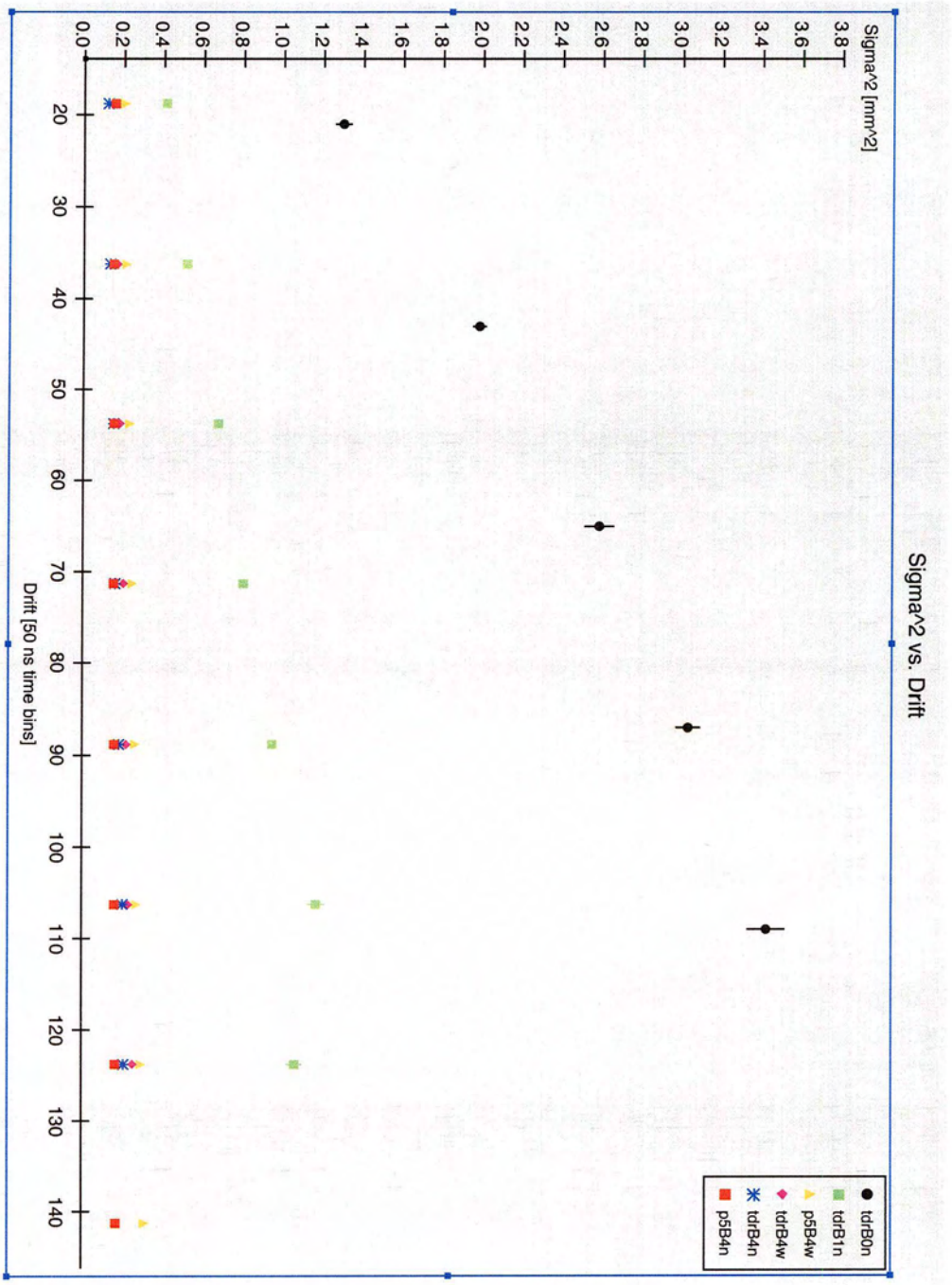

Figure 6.3: Plot of σ^2 vs. drift (all data) which shows the expected linear dependence.

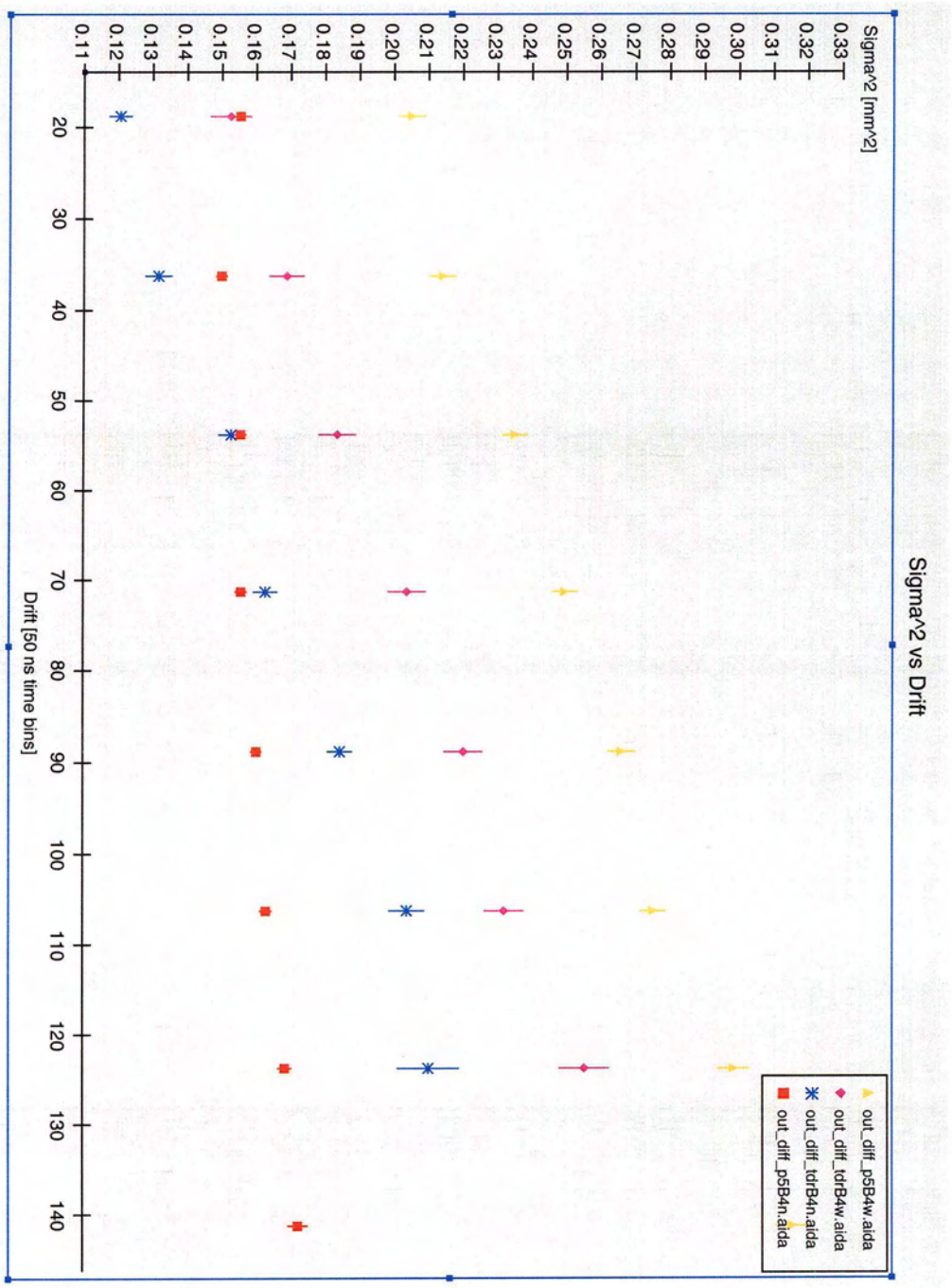

Figure 6.4: Plot of σ^2 vs. drift (4.0T data only).

there is a signal on any pad due to noise. The choice of this parameter effects the estimated diffusion. However, the relative ratio in the estimated diffusion between the data and the MC is constant regardless of the choice of this noise parameter. Therefore we can obtain a correction factor (C) to apply to the reproduced diffusion by considering the ratio of the diffusion constant, which is input to the MC, to the diffusion constant which is reproduced by the MC. From table 6.2 we take the average value of C, which is $C = 1.11$, and apply this to the diffusion measurements from the data. Table 6.3 shows the corrected diffusion constants for all the data sets as well as the diffusion constants simulated by the Magboltz program. Figure 6.5 shows two MC runs which have diffusion constants which differ by 10%. There is very little effect on the resolution for these two data sets.

Unfortunately we are not able to estimate the diffusion properties from the data for the individual regions between the GEMs and the pad plane. Thus, the MC uses gas constants which are generated by simulation and do not necessarily represent the actual diffusion in these regions. As well, there are induced signals seen on the pads in the real data due to the motion of the electrons in the induction gap. An attempt is made in the analysis to sum the signal in a way to cancel these induced signals, however it is possible that they may not be completely canceled. These induced signals (which are not included in the MC) along with the unknown diffusion constants in the readout and amplification regions may account for the discrepancy in the defocusing measurements between the MC and the data which is seen in table

MC data set	Diff. out $\frac{\mu m}{\sqrt{cm}}$	Diff. input $\frac{\mu m}{\sqrt{cm}}$	Correction C
p5B4wMC	60.1 ± 2.5	67.1	1.12
p5B4nMC	26.3 ± 2.1	30.0	1.14
tdrB4wMC	57.6 ± 1.8	64.7	1.12
tdrB4nMC	58.0 ± 1.1	62.6	1.08
tdrB1nMC	168.1 ± 1.1	184.4	1.10
tdrB0nMC	290.3 ± 1.9	313.3	1.08

Table 6.2: Diffusion constant input and output for MC and correction factors.

Data set	Corrected Diffusion $\frac{\mu m}{\sqrt{cm}}$	Diffusion (sim.) $\frac{\mu m}{\sqrt{cm}}$
p5B4w	76.3 ± 4.1	67.0 ± 1.0
p5B4n	33.5 ± 4.5	43.0 ± 1.0
tdrB4w	71.3 ± 10.1	68.7 ± 1.0
tdrB4n	69.5 ± 4.9	68.7 ± 1.0
tdrB1n	204.7 ± 6.6	205.8 ± 2.0
tdrB0n	347.8 ± 16.5	467.7 ± 10.0

Table 6.3: Corrected diffusion constants and Magboltz simulated diffusion constants.

6.4.

6.3 Resolution

Tables 6.5 and 6.6 show the the list of cuts which were applied to the data sets for analysis.

Figure 6.6 shows that with increasing magnetic field the transverse resolution improves for all drift distances. The dependance of the resolution on drift distance is also greatly reduced. The remaining analysis will be done exclusively using data runs taken at a magnetic field of 4.0T.

Data set	Defocusing (data)[μm]	Defocusing (MC)[μm]
p5B4w	429.3 ± 2.1	350.1 ± 1.7
p5B4n	382.2 ± 1.2	368.8 ± 0.5
tdrB4w	367.2 ± 4.0	261.8 ± 1.4
tdrB4n	319.6 ± 3.1	254.9 ± 0.9
tdrB1n	509.3 ± 2.3	289.3 ± 2.3
tdrB0n	917.9 ± 15.7	579.9 ± 1.0

Table 6.4: Defocusing measurements for data and MC.

Data set	x_0 [mm]	$err(x_0)$ [mm]	σ [mm]	$err(\sigma)$ [mm]	z_0 [tb]
p5B4w	$\lvert x_0\rvert < 24$	< 0.2	$> 0.15, < 1.0$	< 0.2	$> 10, < 150$
p5B4n	$\lvert x_0\rvert < 15$	< 0.2	$> 0.15, < 0.55$	< 0.2	$> 10, < 150$
tdrB4w	$\lvert x_0\rvert < 24$	< 0.2	$> 0.2, 1.0$	< 0.2	$> 10, < 140$
tdrB4n	$\lvert x_0\rvert < 24$	< 0.2	$> 0.2, < 1.0$	< 0.2	$> 10, < 140$
tdrB1n	$\lvert x_0\rvert < 15$	< 0.2	$> 0.2, < 2.0$	< 0.2	$> 10, < 130$
tdrB0n	$\lvert x_0\rvert < 15$	< 0.4	$> 0.3, < 4.0$	< 0.4	$> 10, < 120$

Table 6.5: Specific cuts.

Cut for all sets	Value
ϕ	$\lvert\phi\rvert < 0.1$
Λ	$\lvert\Lambda\rvert < 0.3$
status	status $= 0$
# clusters	# clusters $= 1$

Table 6.6: Cuts applied to all data sets.

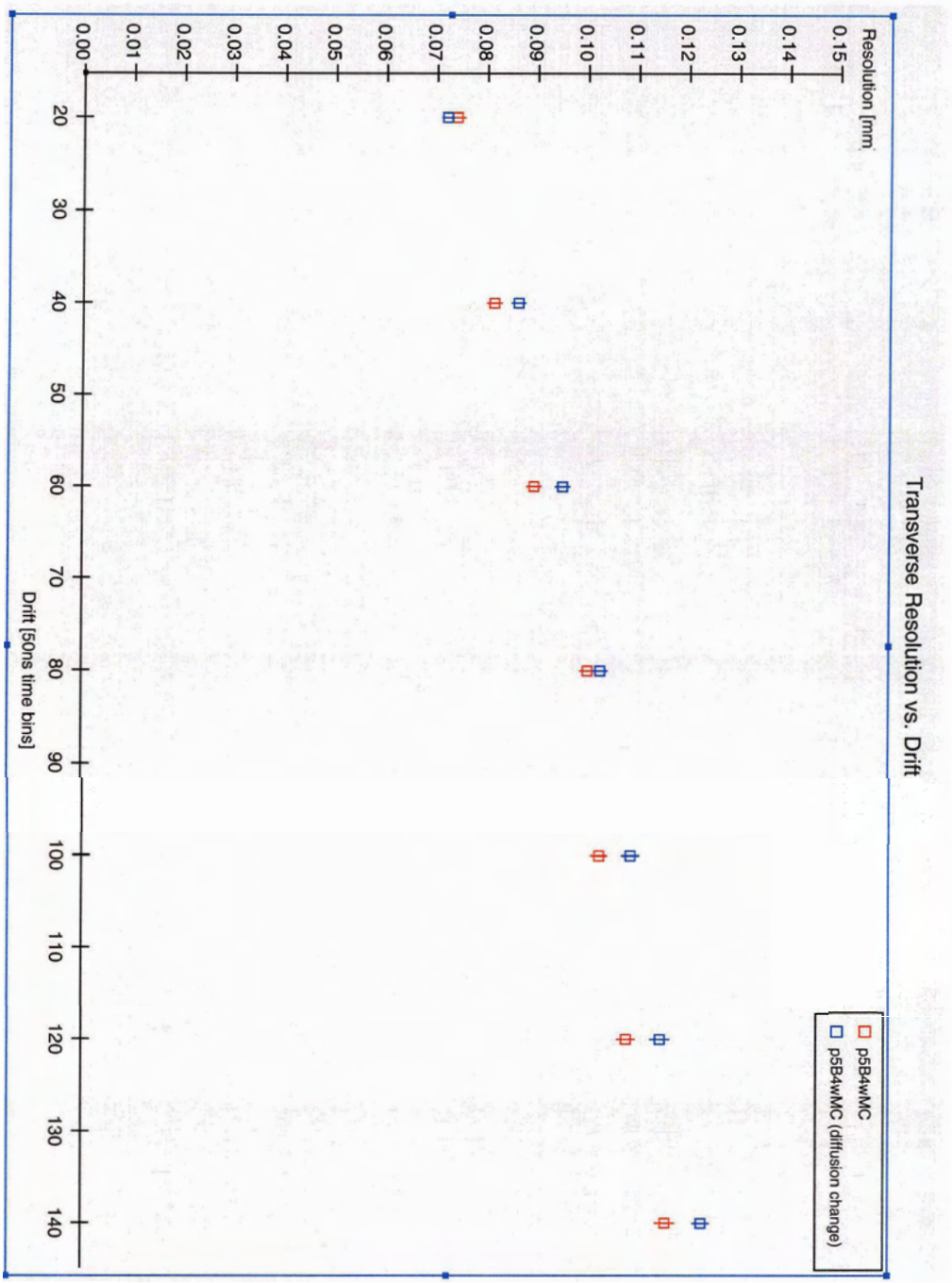

Figure 6.5: Transverse resolution vs. drift for MC sets with a diffusion constant which differs by 10%: There is very little change in the resolution.

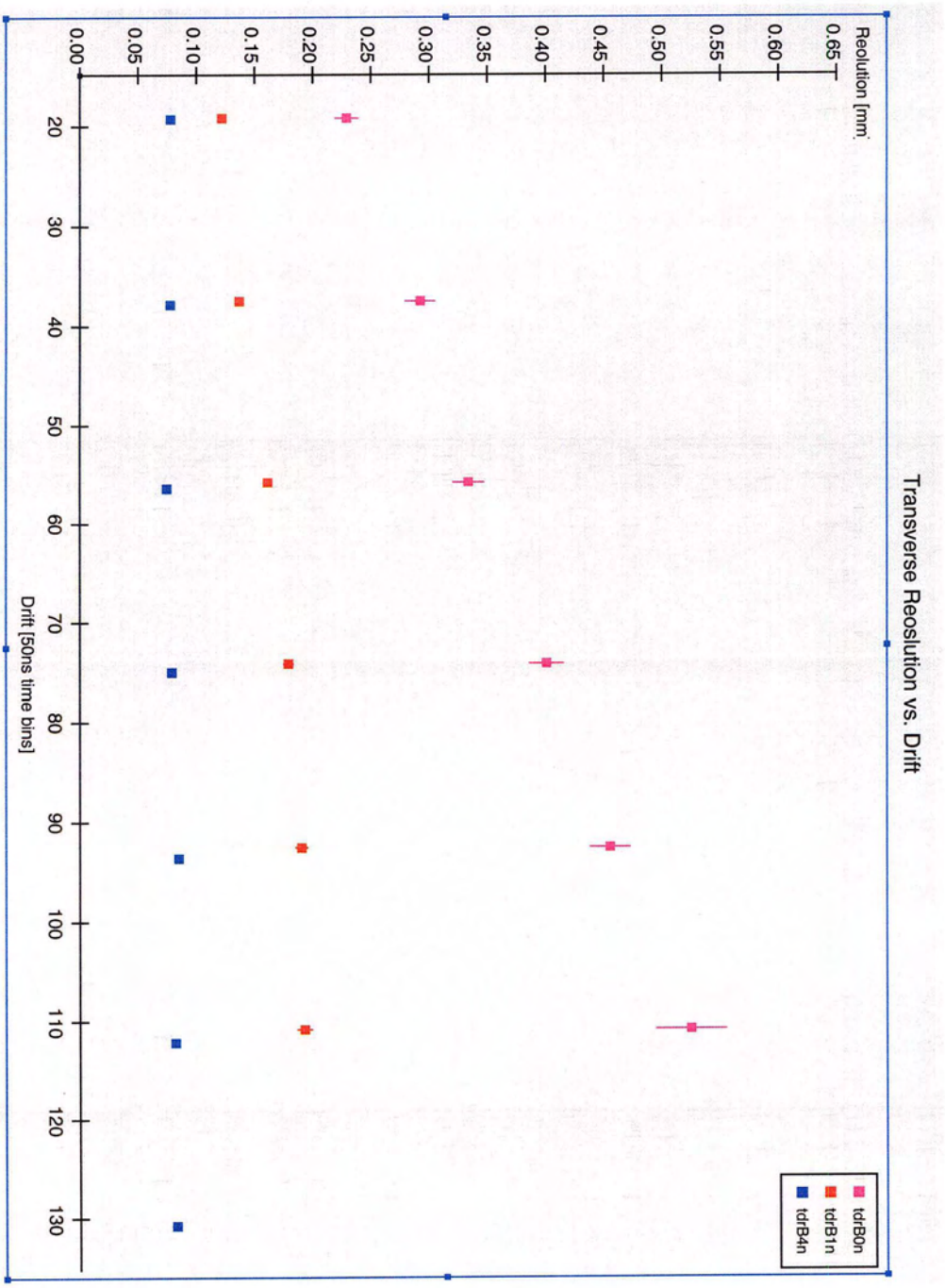

Figure 6.6: Transverse resolution vs. drift for different magnetic fields: As the magnetic field increases the overall resolution improves, as does dependence on drift distance.

6.3.1 Position in the Chamber

First we check for any substantial systematic effects as a function of position in the chamber. Figures 6.7 and 6.8 show that the bias is less than $0.010\,mm$ at all positions in x and z and that there is no obvious dependance on the bias as a function of the position in the chamber. Figure 6.9 shows that there is no significant dependance resolution as a function of x_0.

6.3.2 Track Angle

We next consider the effect of the track angle (ϕ) on the resolution.[2] Figures 6.10, 6.11, 6.12 and 6.13 show the dependance of the resolution on ϕ. A substantial degradation of the resolution can be seen as the track angle increases. This effect is similar to the $\mathbf{E} \times \mathbf{B}$ effect explained in section 2.3 (see figure 6.14). The MC sets show a larger effect on the resolution than the data does as the track angle changes. This can be attributed to different distributions of the amount of charge variation along the track. Figure 6.15 shows an example of the amount of charge which has been collected on one pad row (with the same number of events for each data set). This plot shows that the MC distribution has a greater fluctuation with many more events out on the tail of the distribution. The UV laser allows us to see the track effect for a different distribution of the ionization. The ionization along a laser track is a Poisson distribution which has a much narrower width than the Landau distributed

[2]The cut on ϕ is relaxed to $|\phi| < 0.2$ for this part of the analysis. This is the only step in the analysis where the cuts are changed from above.

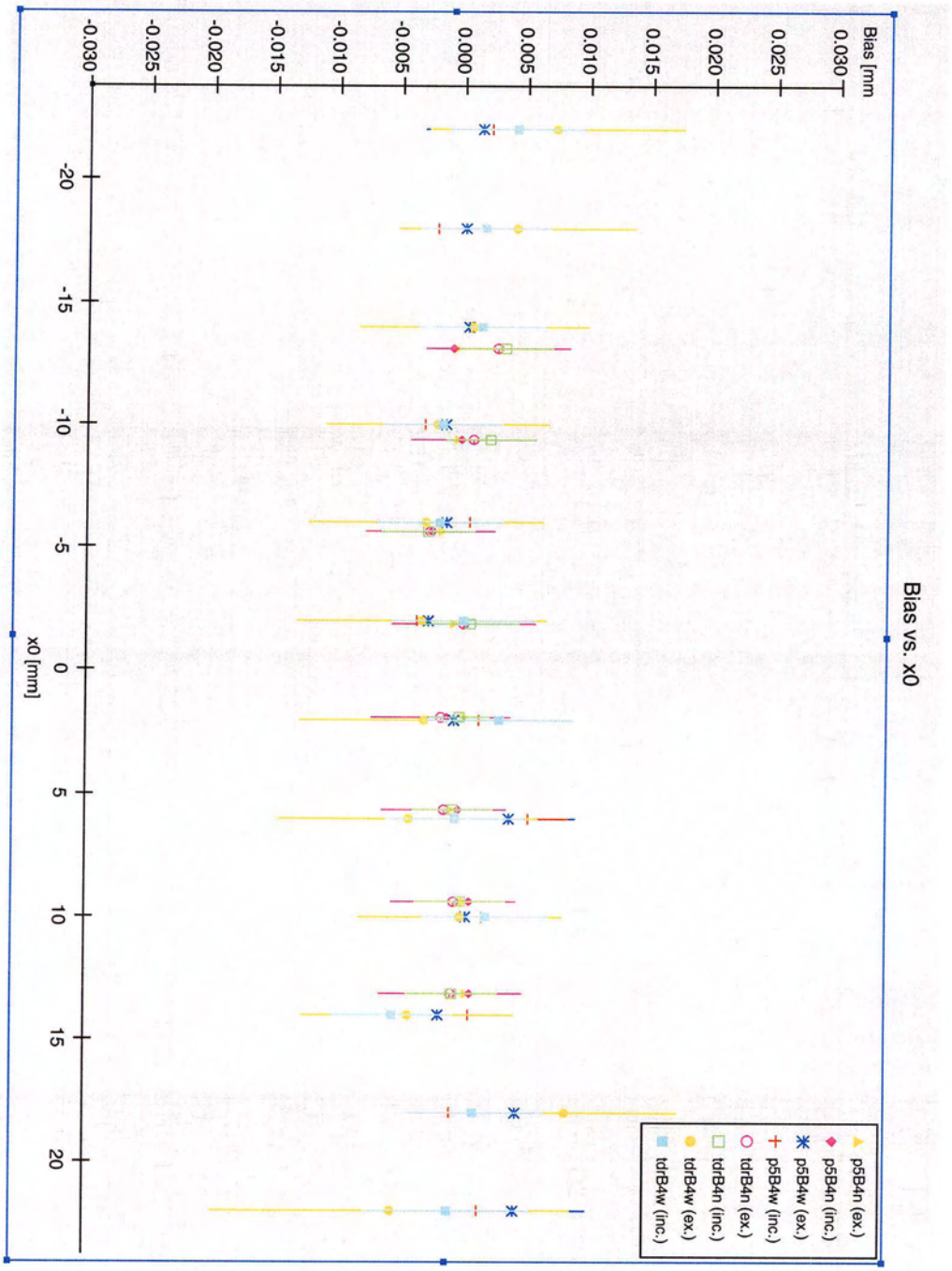

Figure 6.7: Bias vs. x_0: There are no significant biases as a function of x_0.

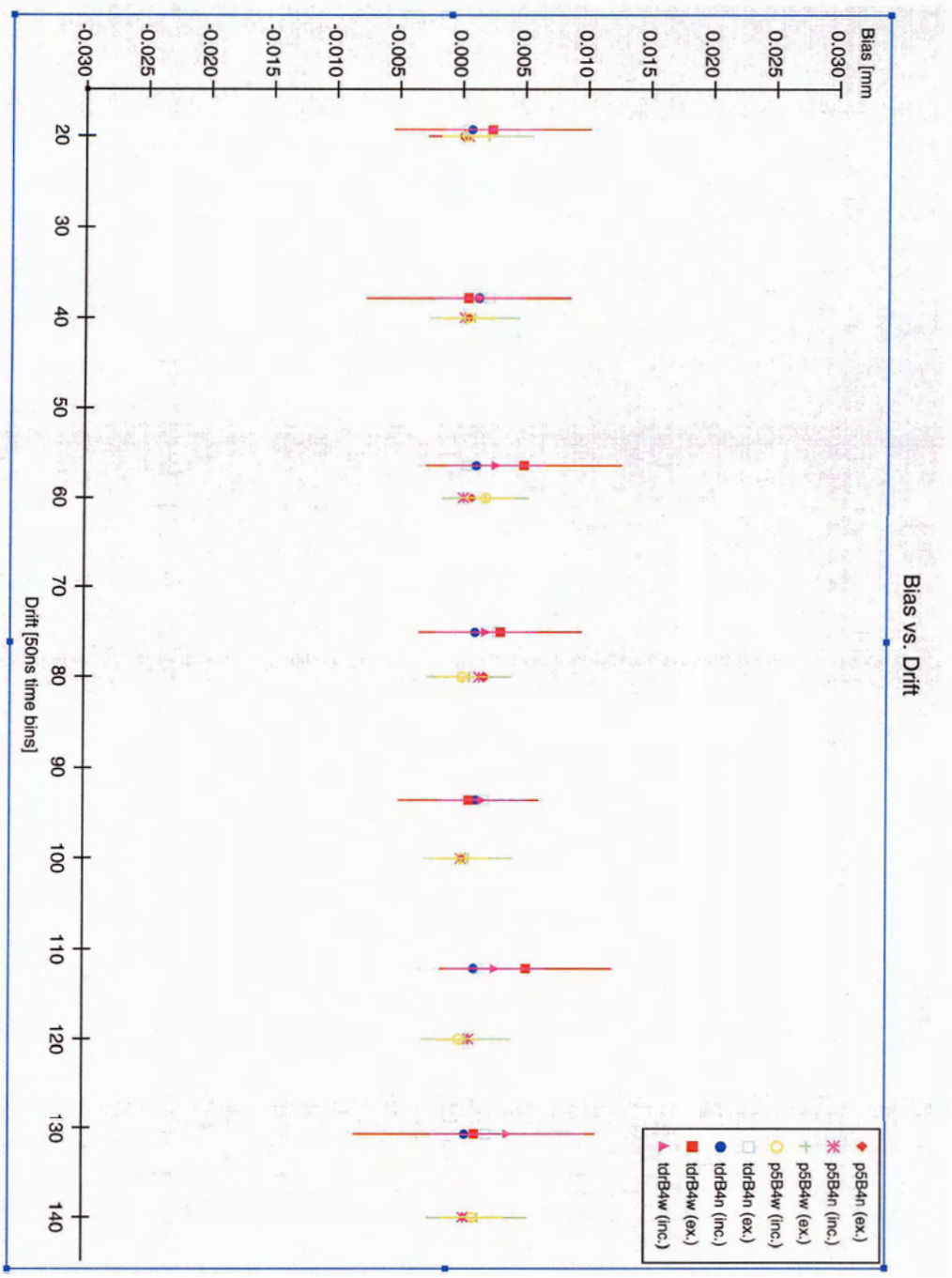

Figure 6.8: Bias vs. z_0: There are no significant biases as a function of z_0.

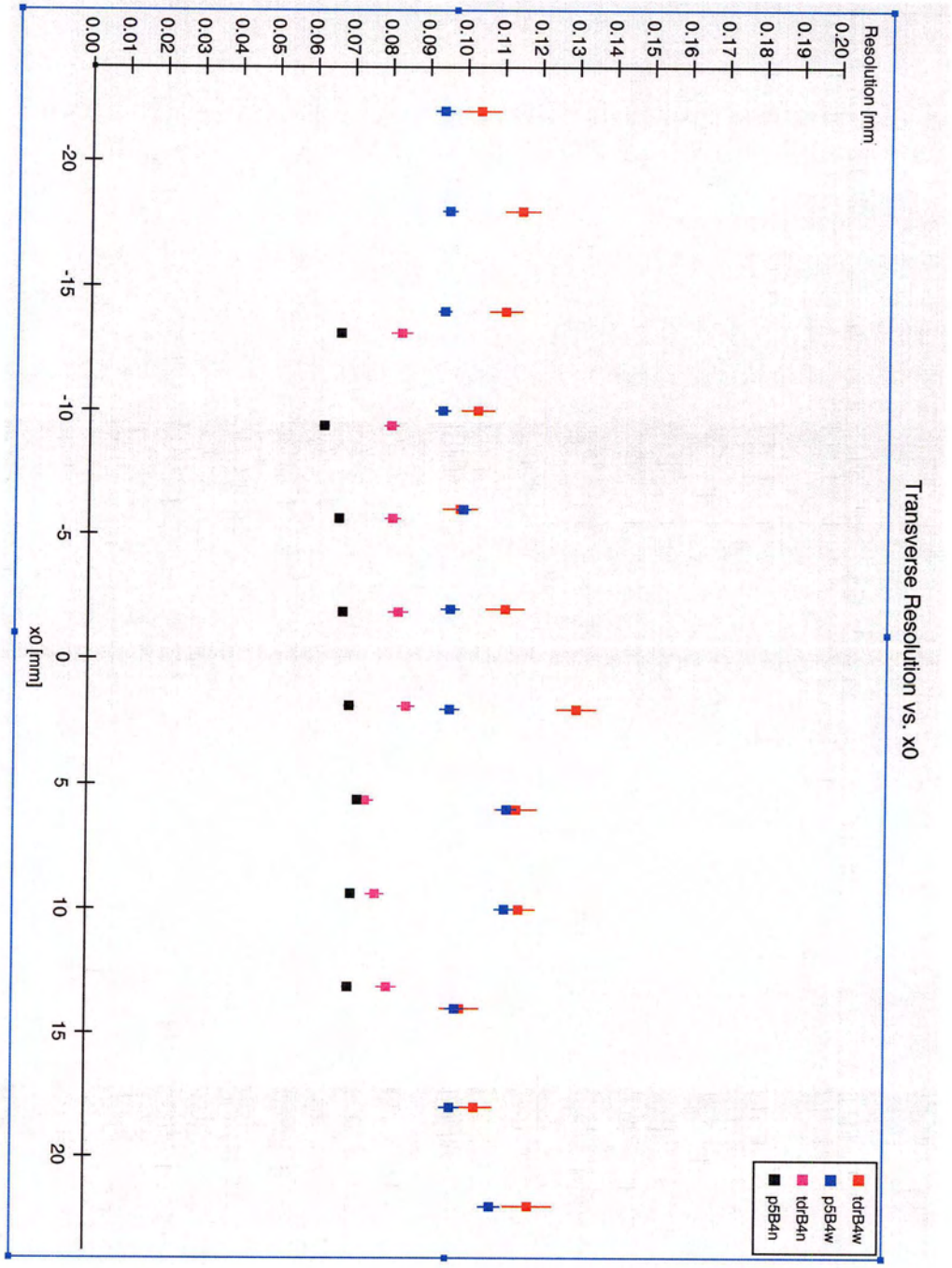

Figure 6.9: Transverse resolution vs. x_0: There is no significant dependence on x_0.

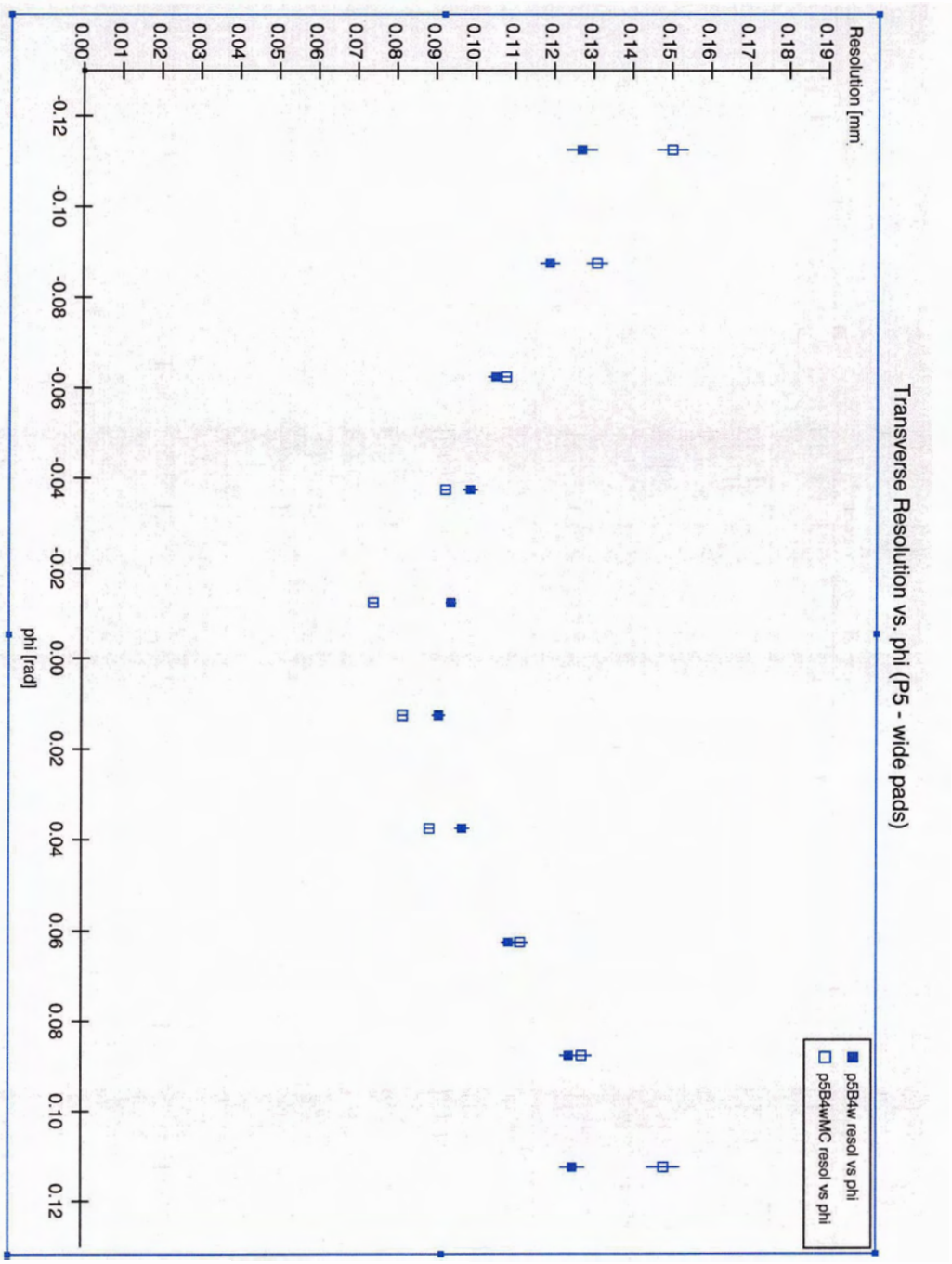

Figure 6.10: Transverse resolution vs. ϕ for P5 gas with wide pads: The resolution is seen to degrade as ϕ increases.

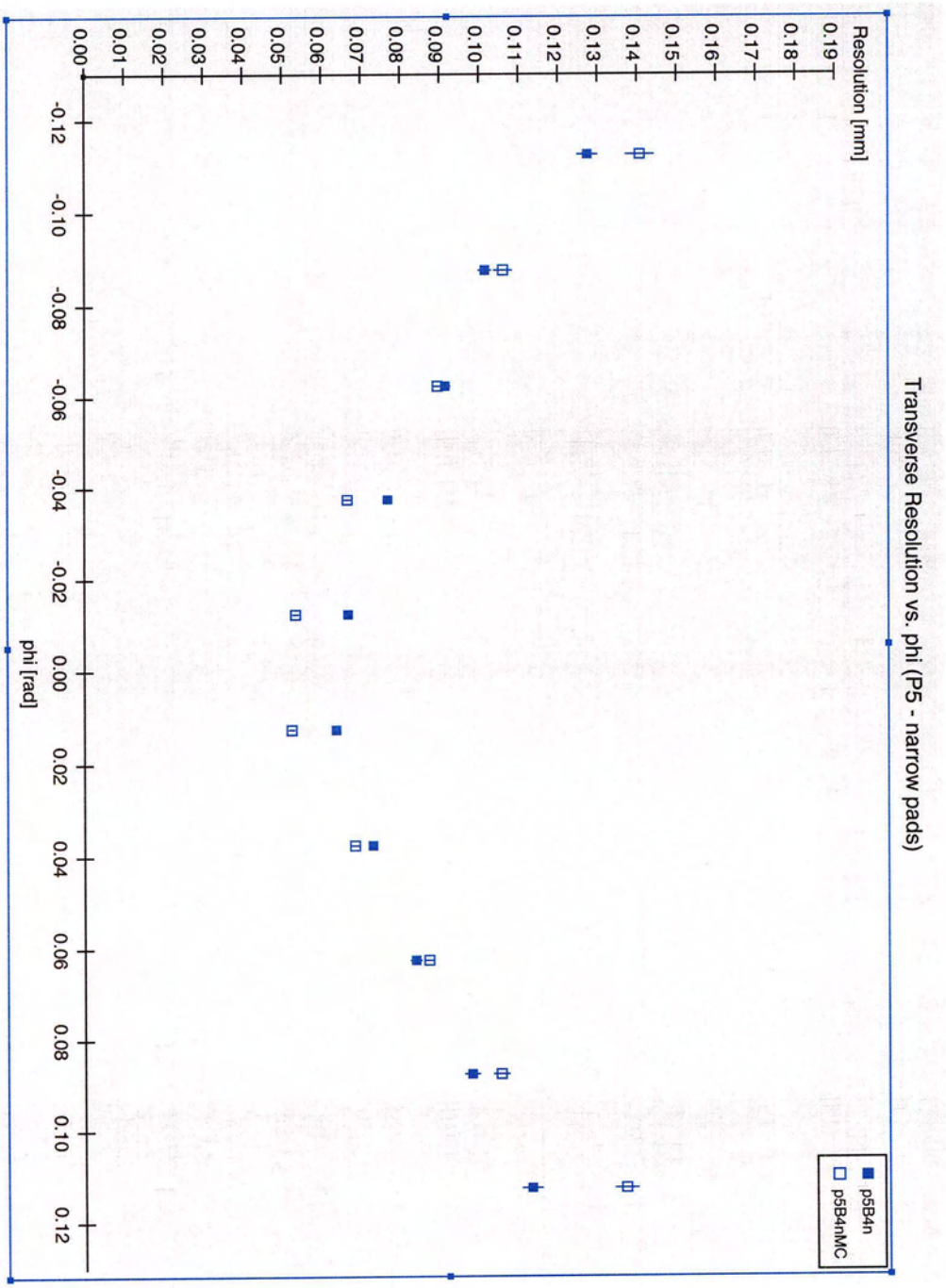

Figure 6.11: Transverse resolution vs. ϕ for P5 gas with narrow pads: The resolution is seen to degrade as ϕ increases.

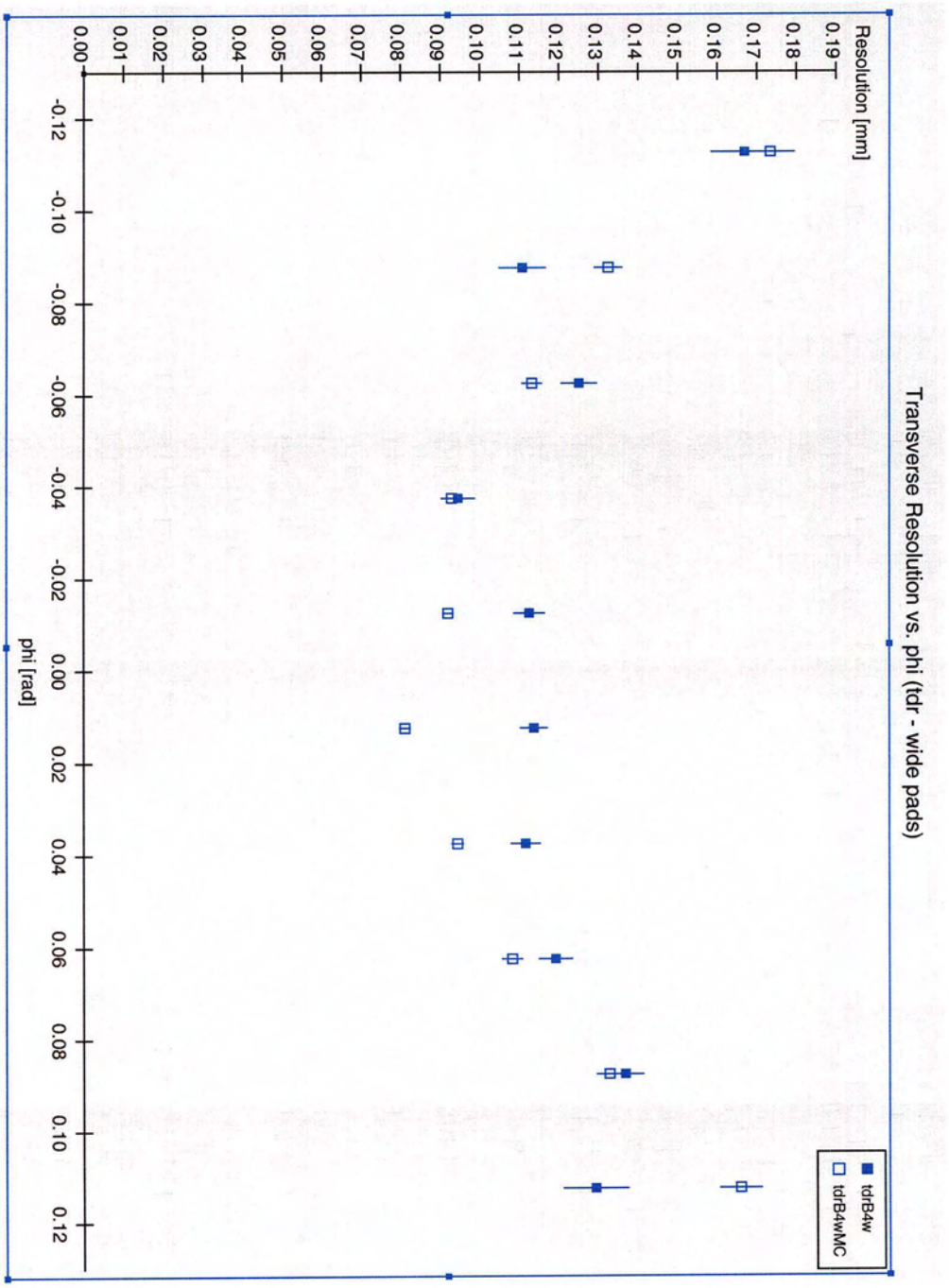

Figure 6.12: Transverse resolution vs. ϕ for TDR gas with wide pads: The resolution is seen to degrade as ϕ increases.

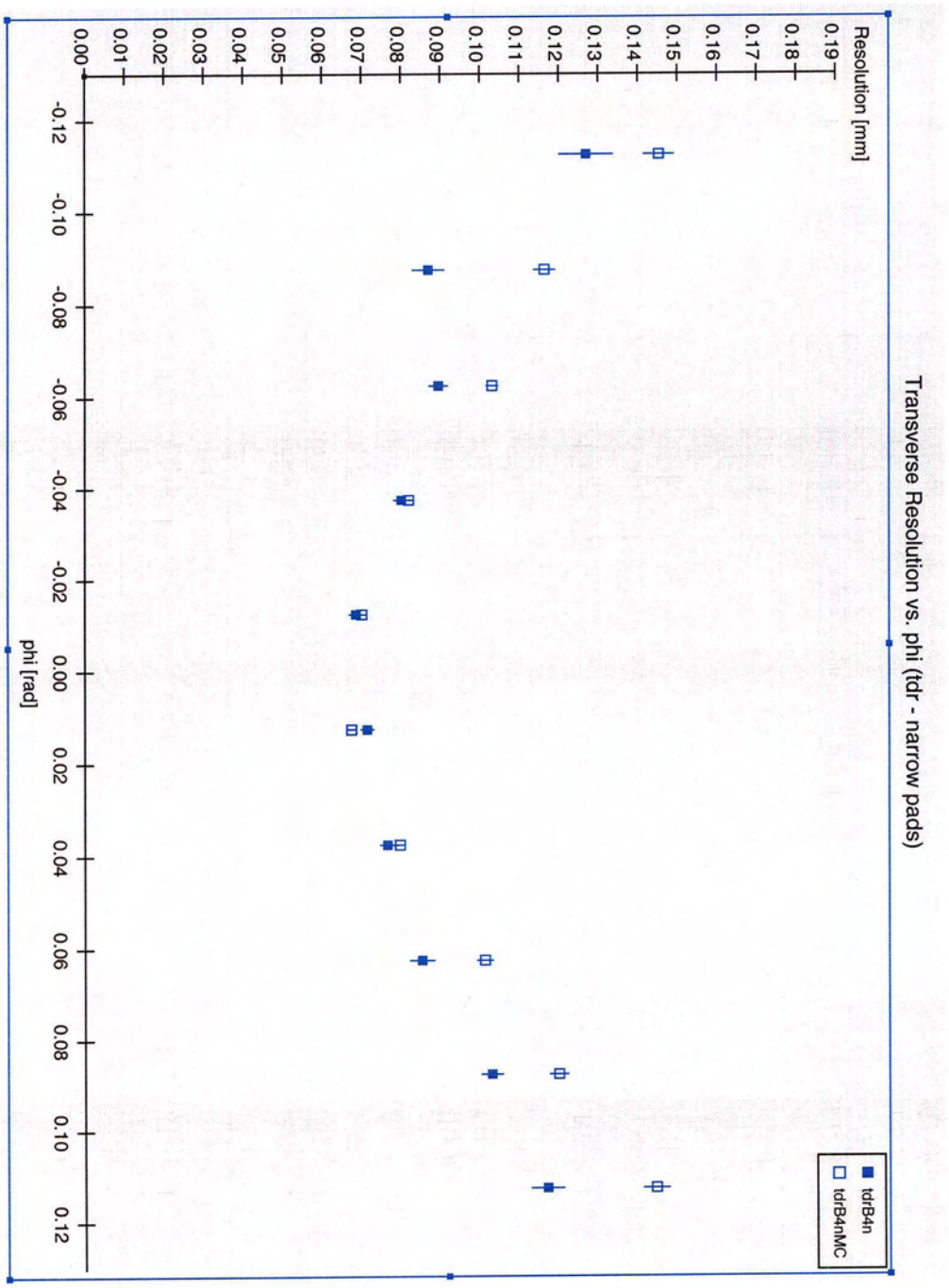

Figure 6.13: Transverse resolution vs. ϕ for TDR gas with narrow pads: The resolution is seen to degrade as ϕ increases.

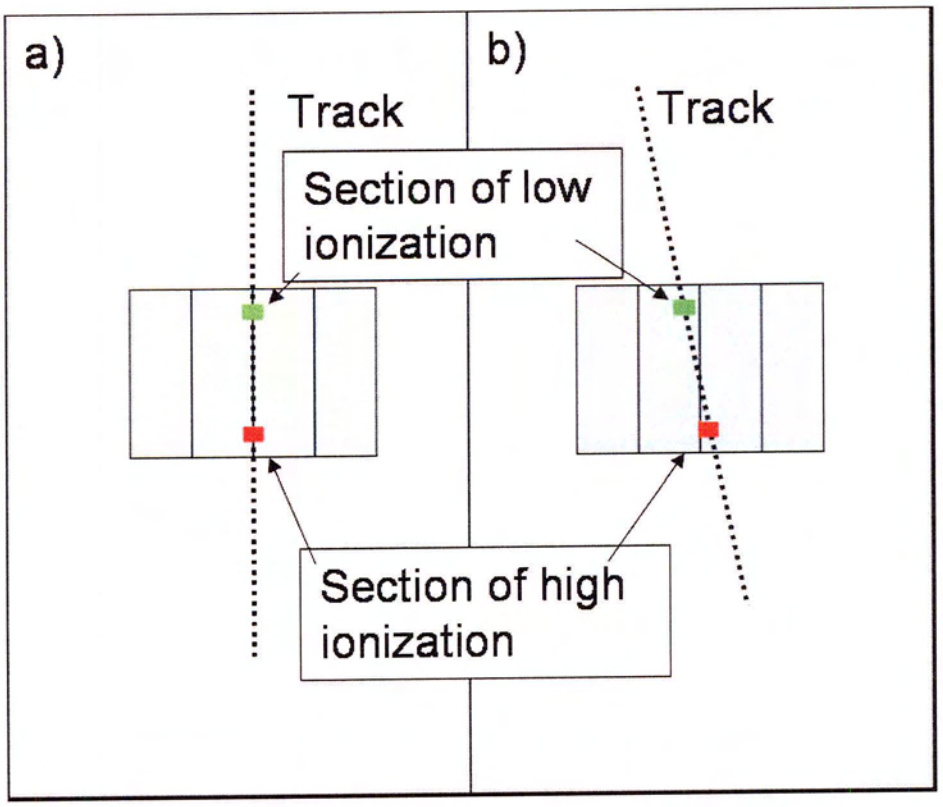

Figure 6.14: A track at an angle relative to the pads can skew the charge sharing between the pads.

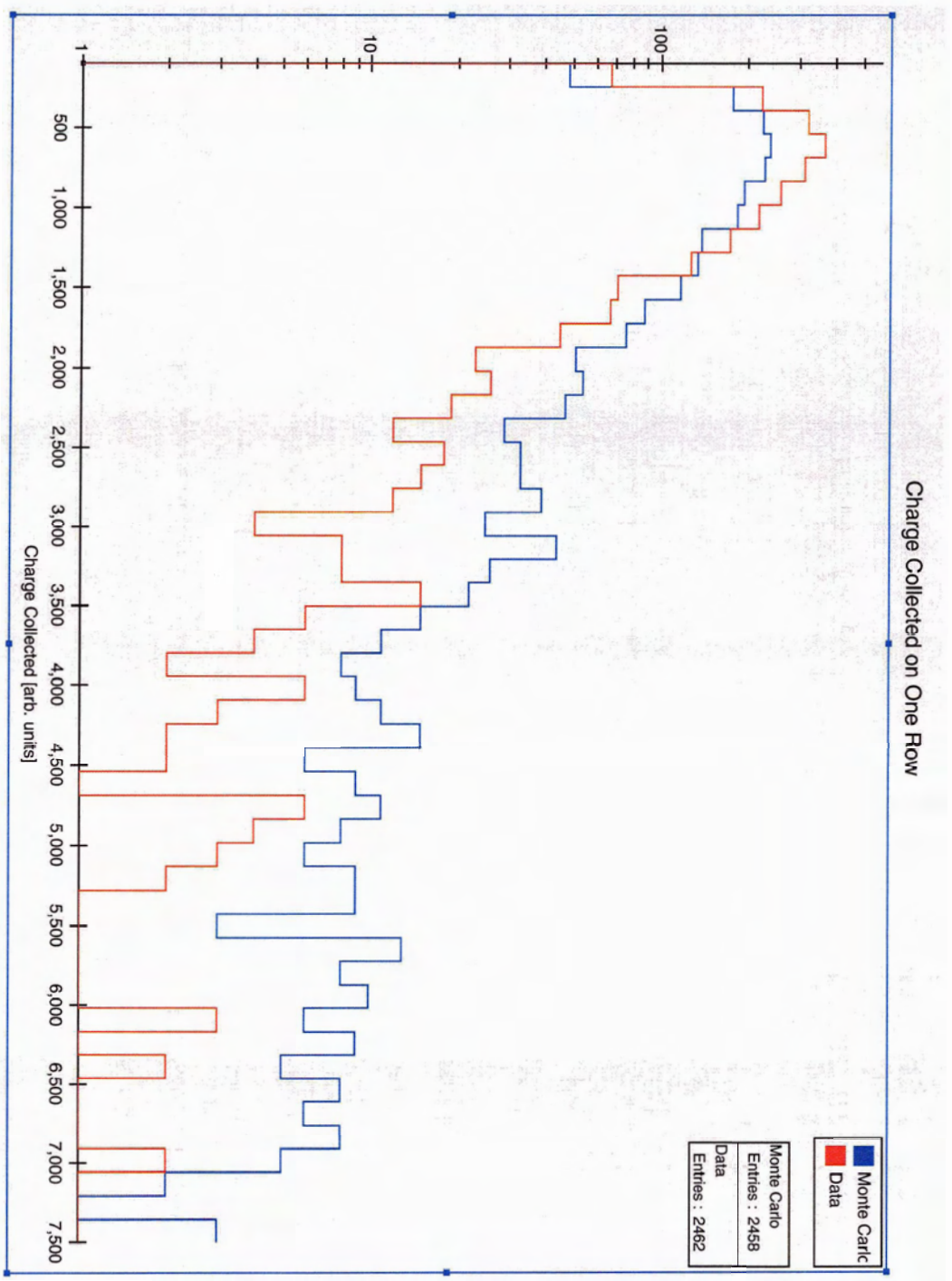

Figure 6.15: Charge collected on a pad row (data and MC): The MC shows many more events with large amounts of charge.

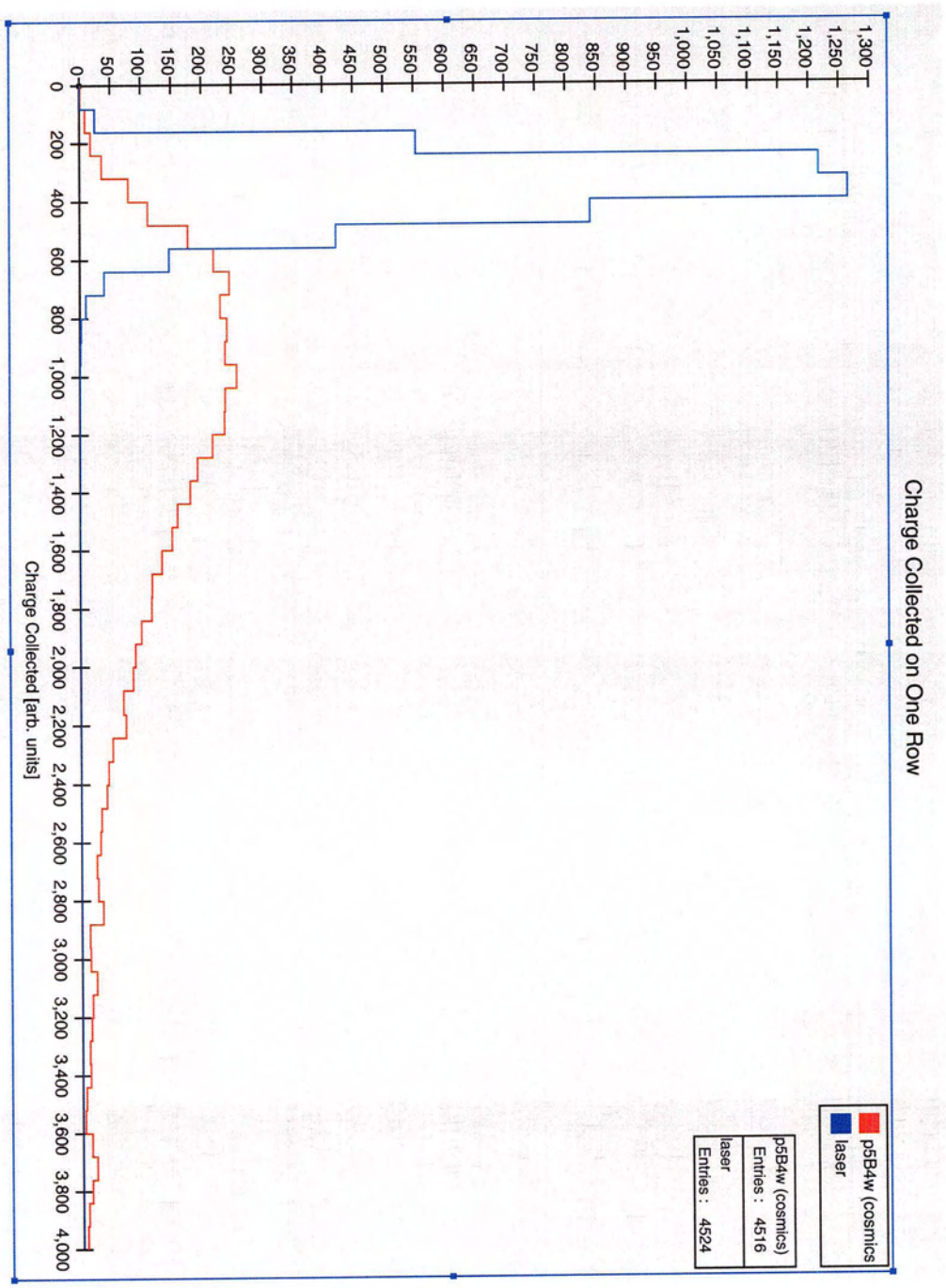

Figure 6.16: Charge collected on a pad row (cosmic and laser tracks): The Landau distribution of the cosmics is much wider than the Poisson distribution of the laser tracks.

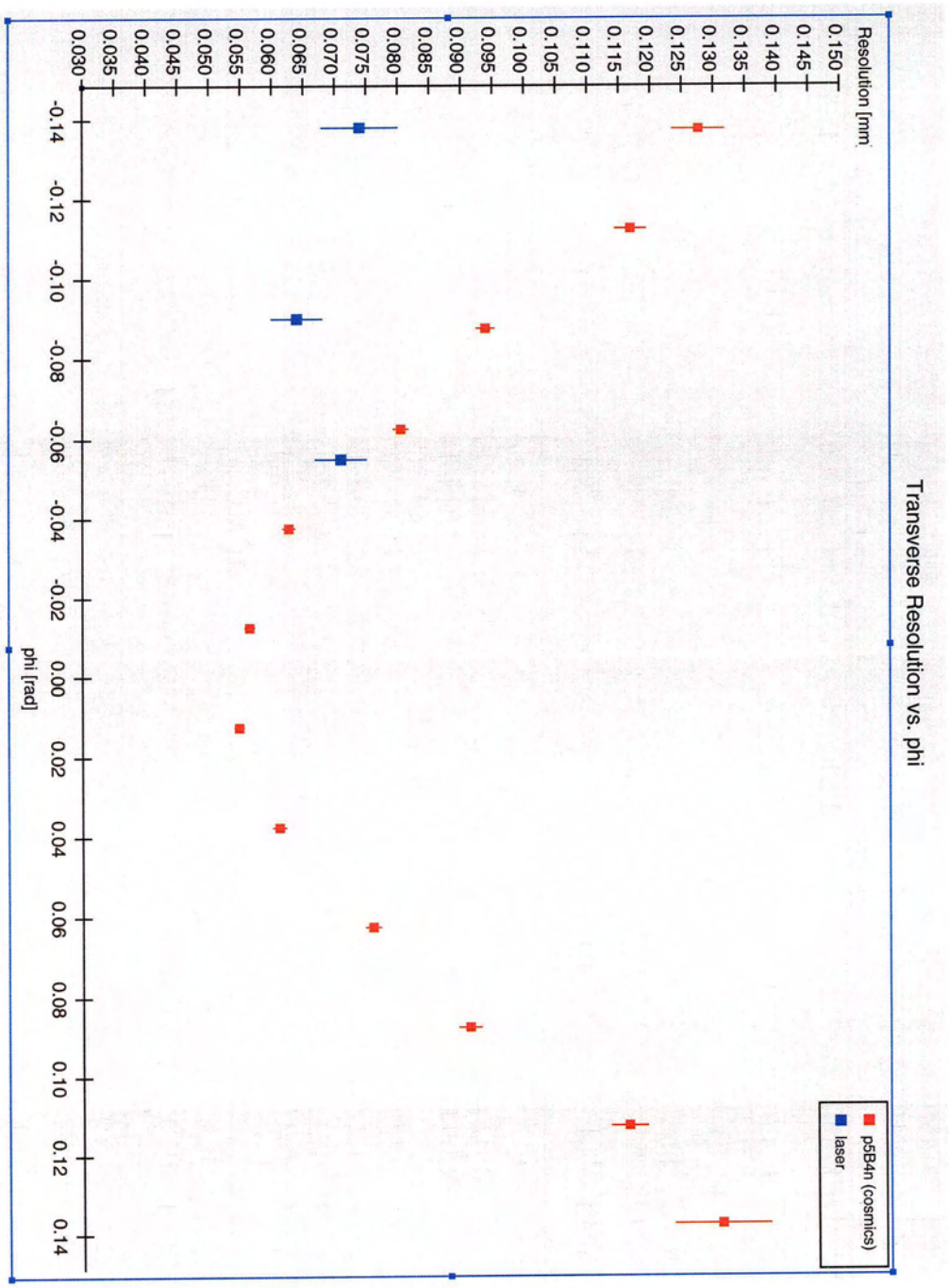

Figure 6.17: Transverse resolution vs. ϕ for cosmic and laser tracks: The resolution of the laser data does not exhibit the same track angle effect.

ionization found in cosmic ray tracks. Figure 6.16 illustrates difference of the two distributions. Three data sets using tracks made with the UV laser were taken with the same operating parameters as data set p5B4n. The track angle was changed for each run. Although the actual value of the resolution for laser tracks and cosmic tracks should not be directly compared, we can see that the track angle effect appears to be much smaller for the laser tracks (see figure 6.17).

6.3.3 Position on a Pad

Figure 6.18 shows the resolution for all data sets as a function of the position on a pad of the track (zero is the center of the pad). From this plot we see that the resolution degrades when the track is closer to the center of the pad. This effect is expected and can be explained as follows. If $f(x) \pm \sigma_f$ is the fraction of the charge collected on a pad and $\mu \pm \sigma_\mu$ is the estimated position of the track. Then σ_μ is given by:

$$\sigma_\mu = \frac{\sigma_f}{|\frac{df}{d\mu}|} \tag{6.1}$$

The estimated track centre moves toward the edge of the pad σ_μ decreases. To illustrate this consider the simplified case where the charge distribution is Gaussian with standard deviation σ and the charge is shared by only two pads. If we consider $x = 0$ to be the boundary between the pads then $f(\mu)$ is given by

$$f(\mu) = \int_0^\infty \frac{1}{\sigma\sqrt{2\pi}} e^{-\frac{(x-\mu)^2}{2\sigma^2}}\, dx = \frac{1}{2} + \frac{1}{2}\mathrm{erf}(\frac{\mu}{\sqrt{2}\sigma}) \tag{6.2}$$

therefore

$$\frac{df}{d\mu} = \frac{1}{\sigma\sqrt{2\pi}} e^{-\frac{\mu^2}{2\sigma^2}} \tag{6.3}$$

From binomial statistics we get

$$\sigma_f \propto \sqrt{f(1-f)} \,. \tag{6.4}$$

In this case $|\frac{df}{d\mu}|$ increases with increasing μ much faster than σ_f decreases, causing σ_μ to increase as we move further from the boundary between the pads.

We can see that the narrow pads show less of an effect, and that the gas with larger defocusing (P5 gas) shows less of an effect than the TDR gas.

Figures 6.19, 6.20, 6.21 and 6.22 show the bias as a function of position on a pad. A clear trend can be seen where the bias is very small in the centre of the pad and increase towards the edges. The bias is positive to the positive side of the pad and negative to the negative side of the pad. This is due to the effect the noise parameter has on reconstructing the track width. The magnitude of the bias is seen to increases as the noise parameter is increased and large noise parameters reduce the track width estimates. If the track width is estimated to be too small in the reference track, when the track fit using only the the information in the resolution row is done (to find the residual) this fit will have the width fixed to a value which is too small. If the reference track is on the positive side of the pad then the information from the adjacent pad on that side will bias the residual in the positive direction (since the track width is fixed).

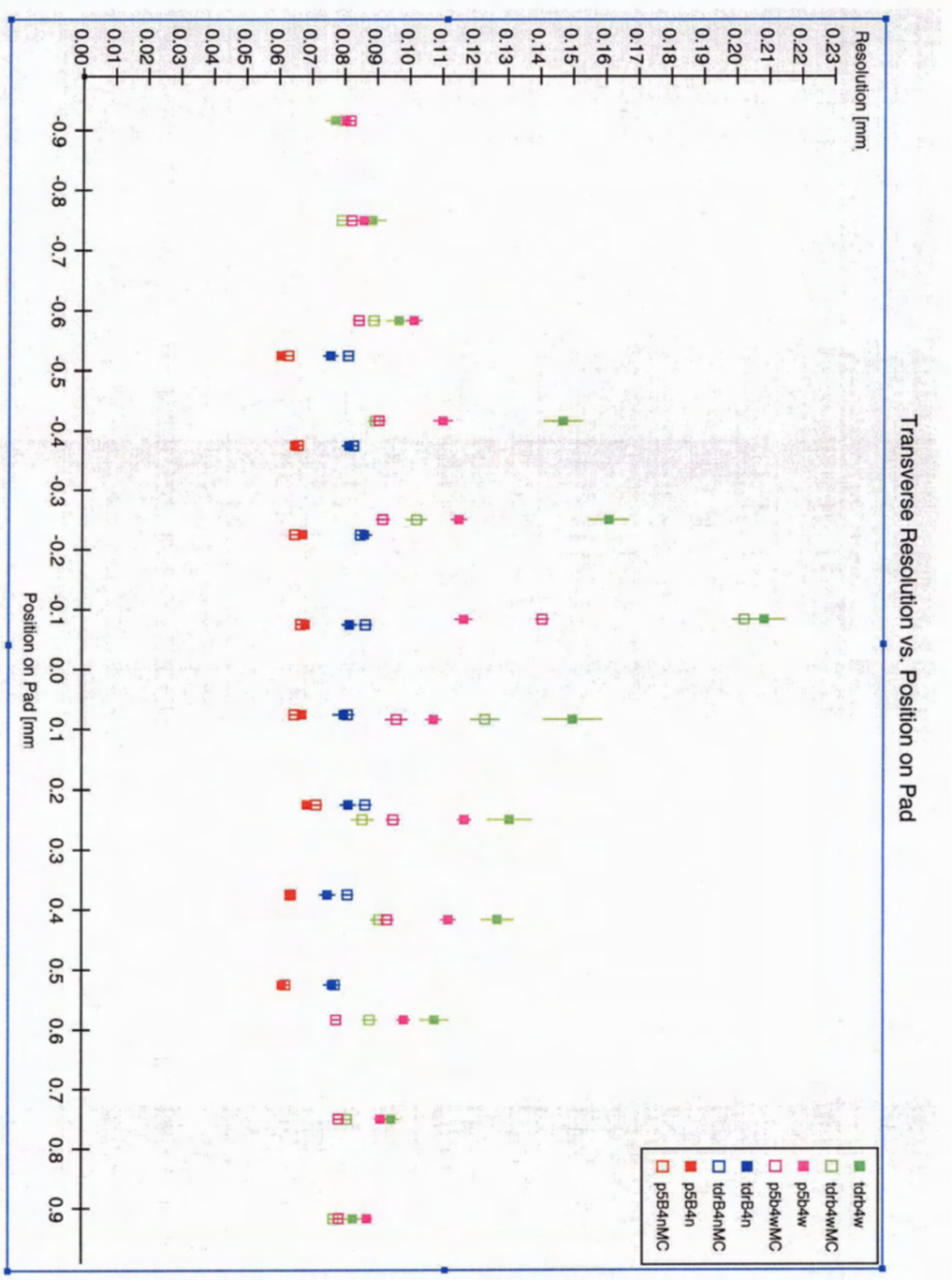

Figure 6.18: Transverse resolution vs. position on a pad: The resolution degrades near the centre of the pad.

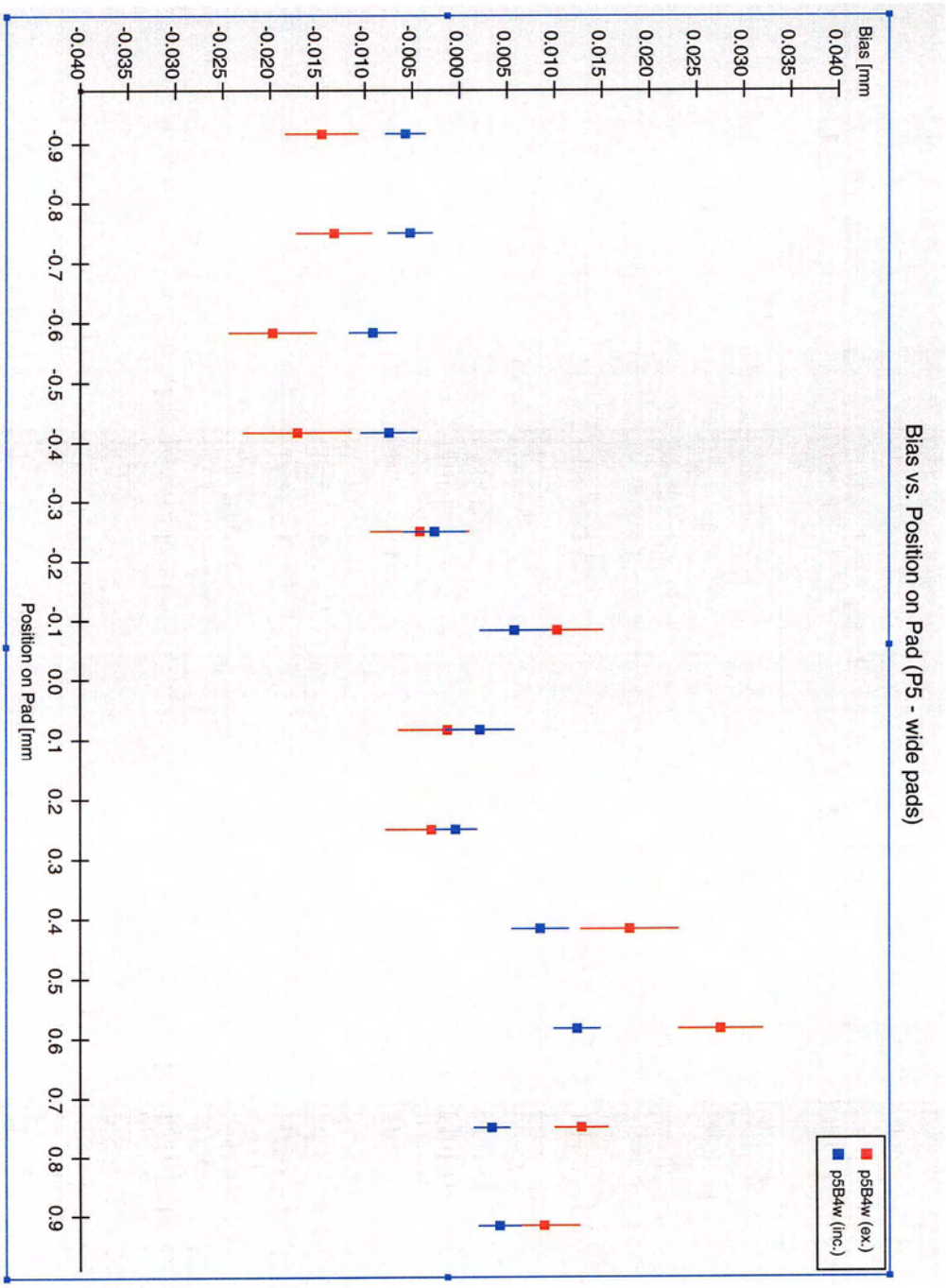

Figure 6.19: Bias vs. position on a pad (P5 wide pads): Biases are seen as a function of the position on the pad.

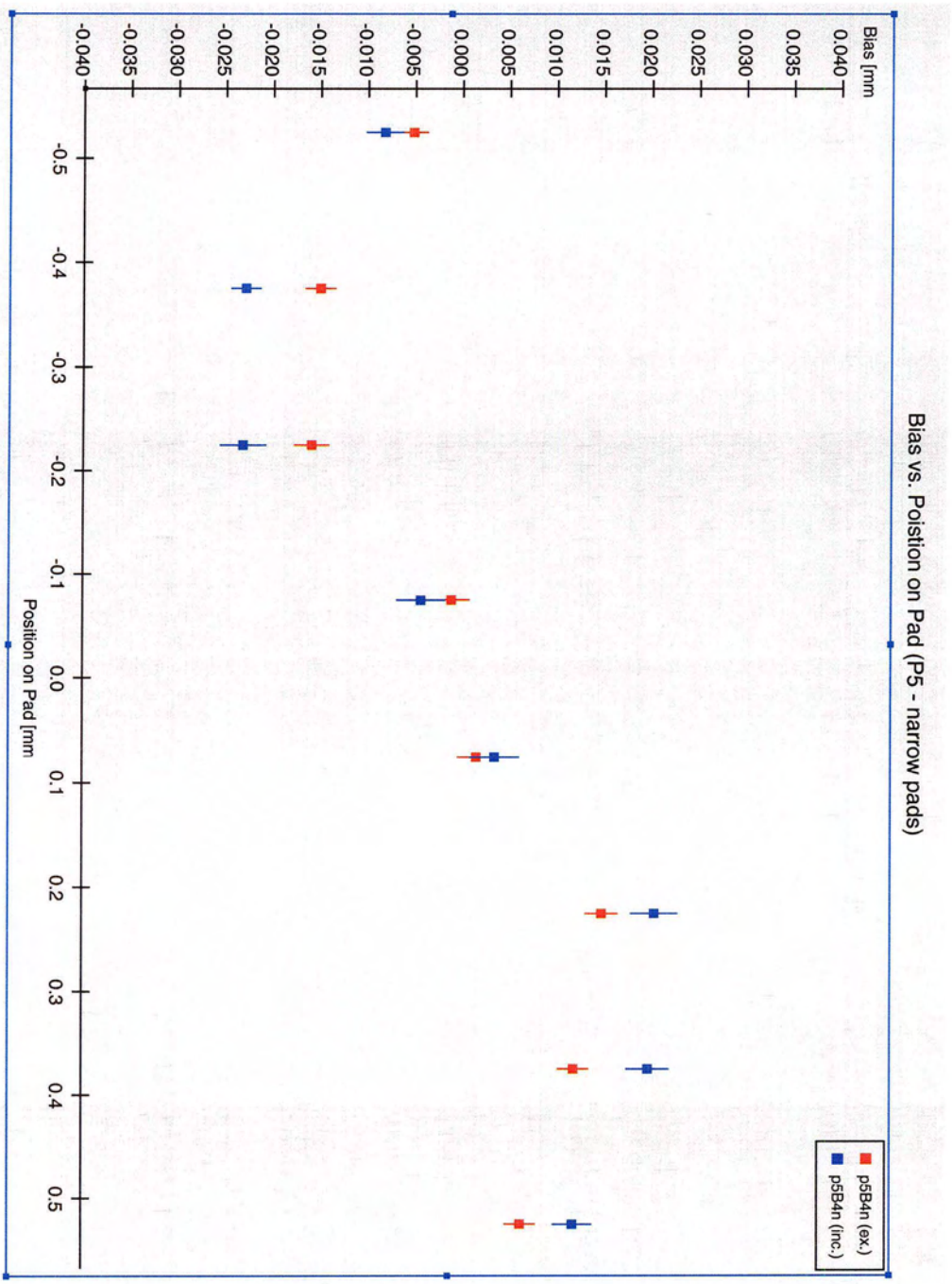

Figure 6.20: Bias vs. position on a pad (P5 narrow pads): Biases are seen as a function of the position on the pad.

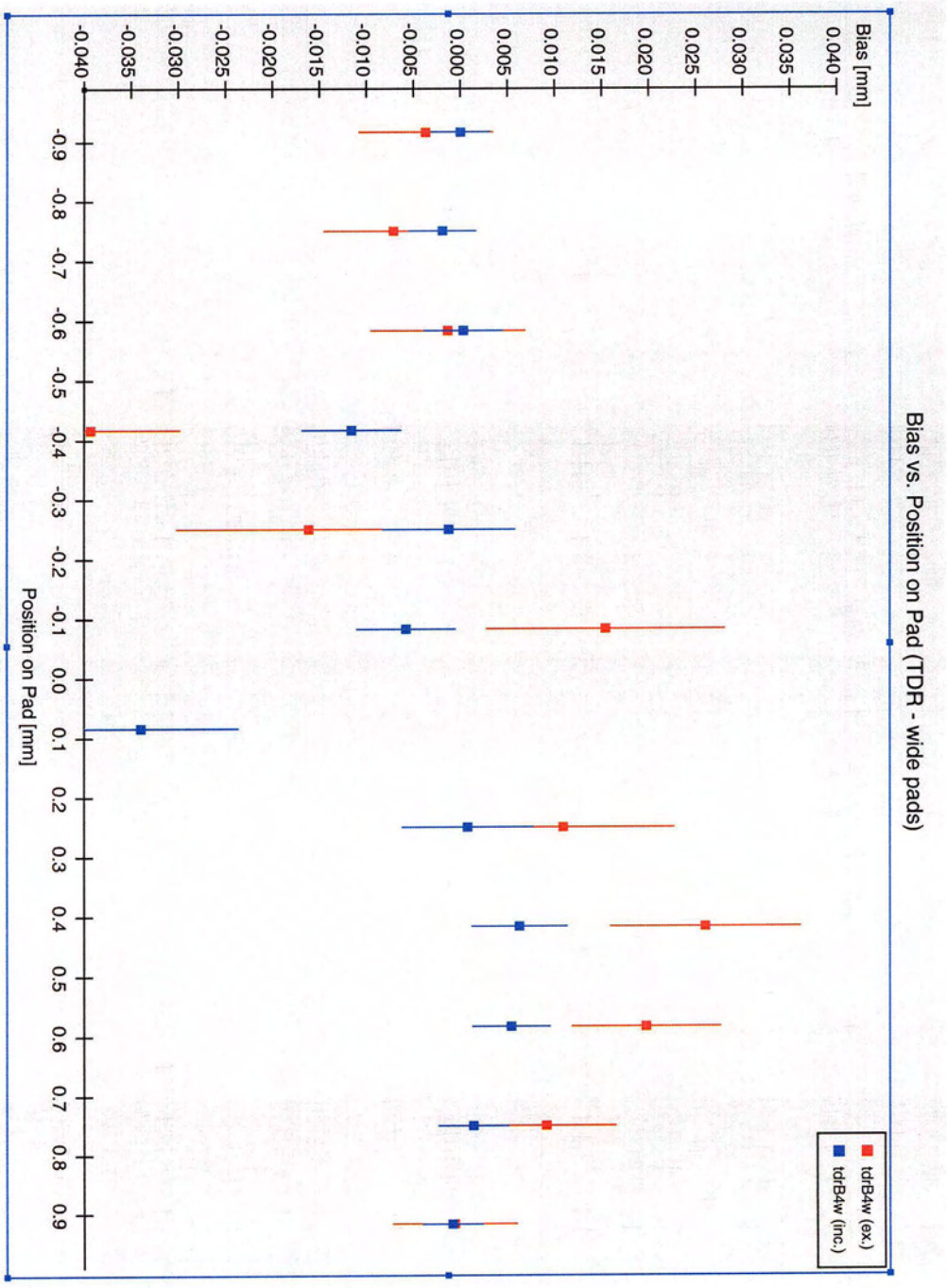

Figure 6.21: Bias vs. position on a pad (TDR wide pads): Biases are seen as a function of the position on the pad.

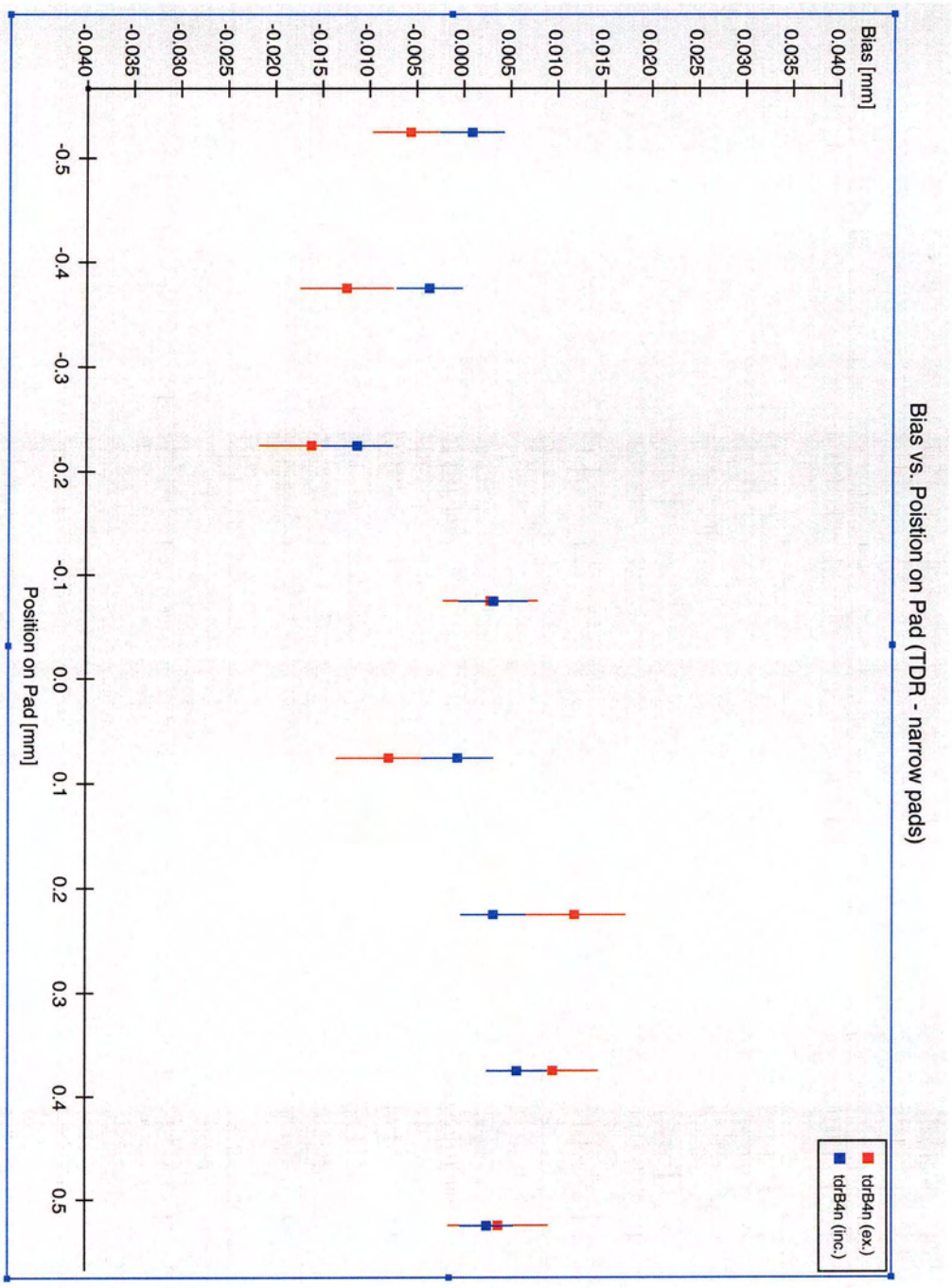

Figure 6.22: Bias vs. position on a pad (TDR narrow pads): Biases are seen as a function of the position on the pad.

Data Set	Resolution [μm] (data)	Resolution [μm] (MC)
p5B4w	107.6 ± 0.7	97.5 ± 0.6
p5B4n	66.7 ± 0.4	69.8 ± 0.7
tdrB4w	116.9 ± 1.5	111.0 ± 0.7
tdrB4n	82.4 ± 0.9	87.8± 0.6

Table 6.7: Overall transverse resolution.

6.3.4 Drift Distance

Perhaps the most important variable's effect on the resolution to consider is the drift distance. For a large scale tracker it is necessary to maintain good resolution for drift distances of a few meters. Figure 6.23 and 6.24 show how the resolution changes with drift distance for data and MC. Again we see that the narrow pads have a better resolution overall, but it is important to note that even for the narrow pads there is a significant difference between P5 and TDR gas as the drift distance increases (figure 6.23). The P5 gas has better resolution for all drift distances (see figure 6.25).

6.3.5 Overall Resolution

Finally we tabulate the overall resolution for all rows (table 6.7). We see that for each data set the overall resolution is in reasonable agreement with the corresponding MC set.

6.3.6 Longitudinal Resolution

In the transverse plane, one measures p_t. To convert to absolute $|p|$ we need to find $tan\lambda$ whose uncertainty depends on the error in the estimation of the longitudinal

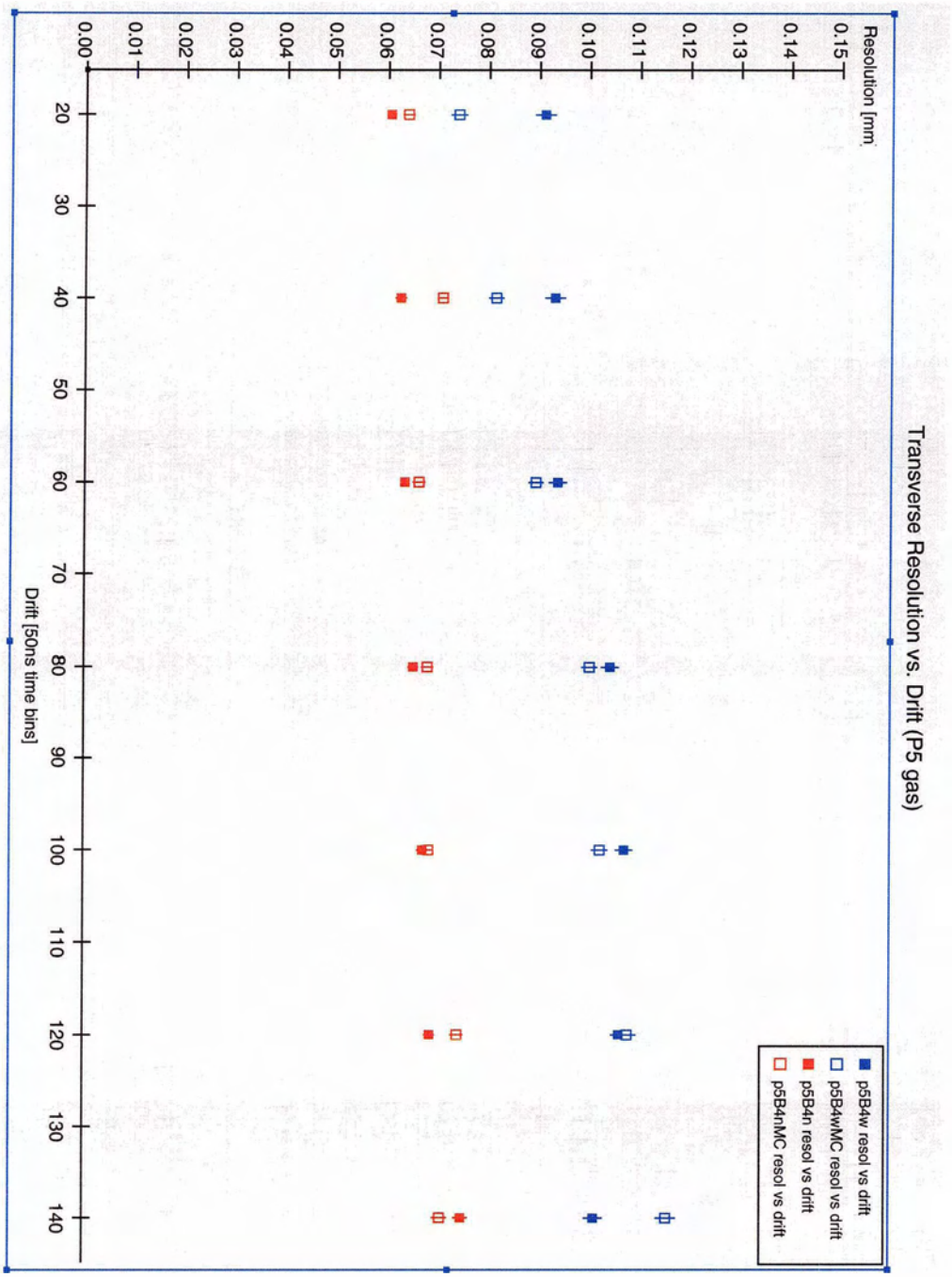

Figure 6.23: Transverse resolution vs. drift (P5 gas).

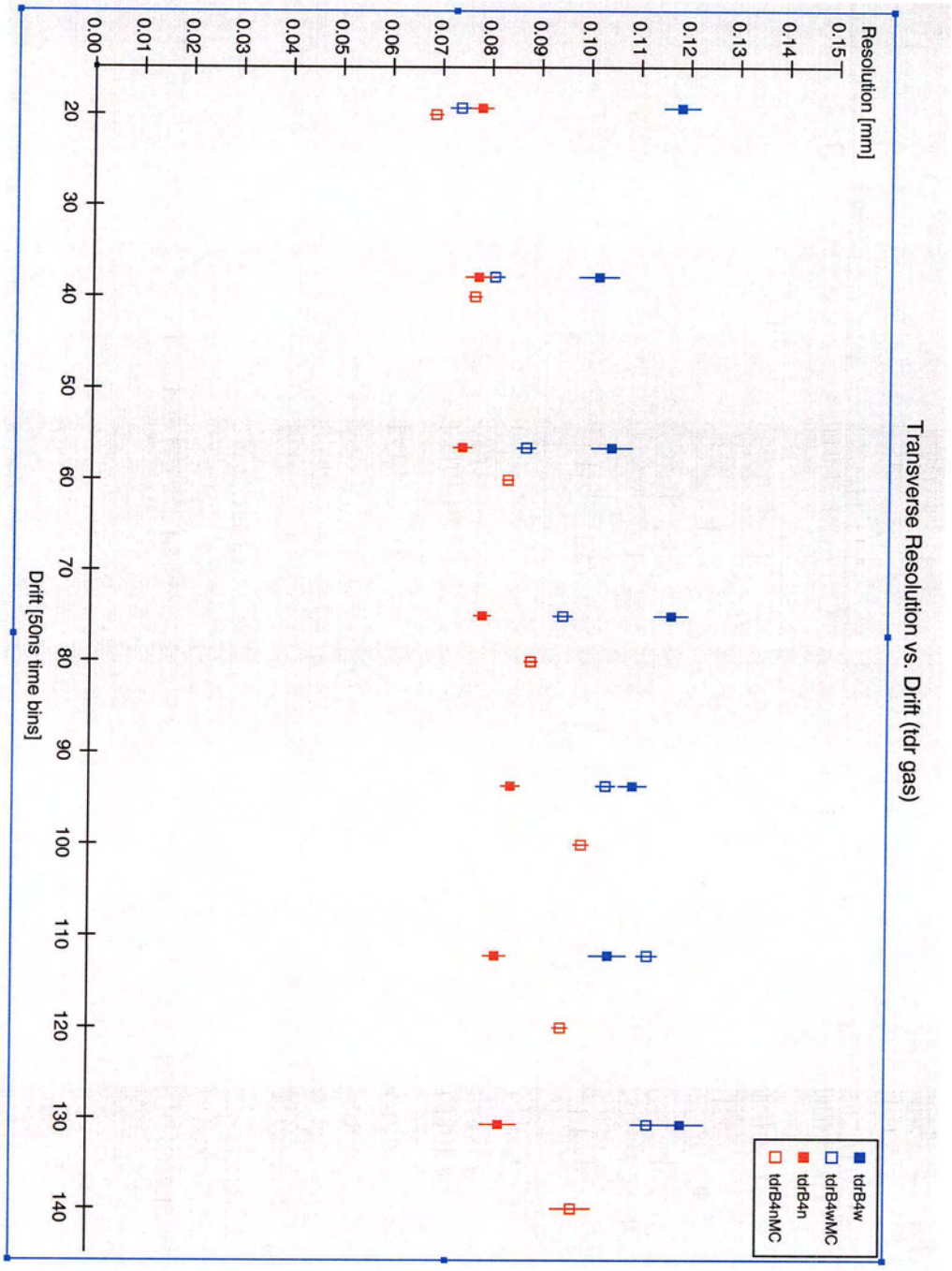

Figure 6.24: Transverse resolution vs. drift (TDR gas).

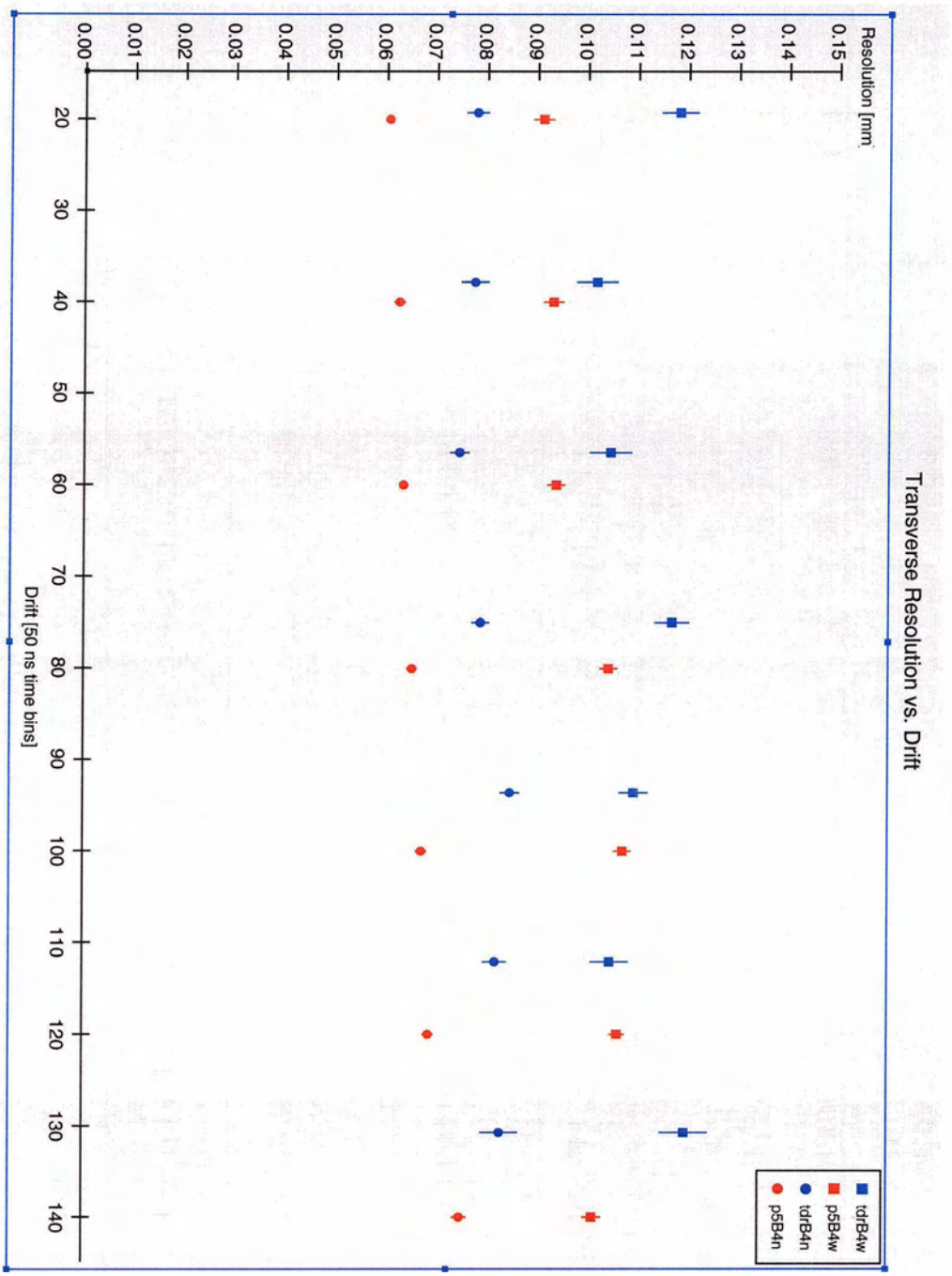

Figure 6.25: Transverse resolution vs. drift (All data): P5 gas is seen to have better resolution for both wide and narrow pads.

coordinates. However since a large lever arm is used, the uncertainty in $|p|$ is dominated by the uncertainty in p_t, not $tan\lambda$. The resolution in the longitudinal direction is therefore not as crucial as it is in the transverse direction. Figure 6.26 shows the resolution in the longitudinal direction as a function of drift distance. The resolution in these plots is given in units of time bins. Multiplying by the appropriate drift velocities (in units of $\mu m/tb$) gives us the resolution in μm. Although our analysis has not been optimized for reconstructing tracks in the z direction we see that the longitudinal resolution is better than 1200 μm for all drift distances for P5 gas, and better than 960 μm for TDR gas. Figure 6.27 shows the longitudinal resolution for the data sets p5B4w and tdrB4n and the corresponding MC data sets. The data and MC are in good agreement for tdrB4n. For the set p5B4w we did not know the gas properties exactly and the Magboltz value for longitudinal diffusion was used. The diffusion in the transverse direction for this data set was found to be substantially higher than the Magboltz value. An increased longitudinal diffusion would account for the increased overall resolution values (compared with MC). The overall trend in the MC is followed well by both data sets.

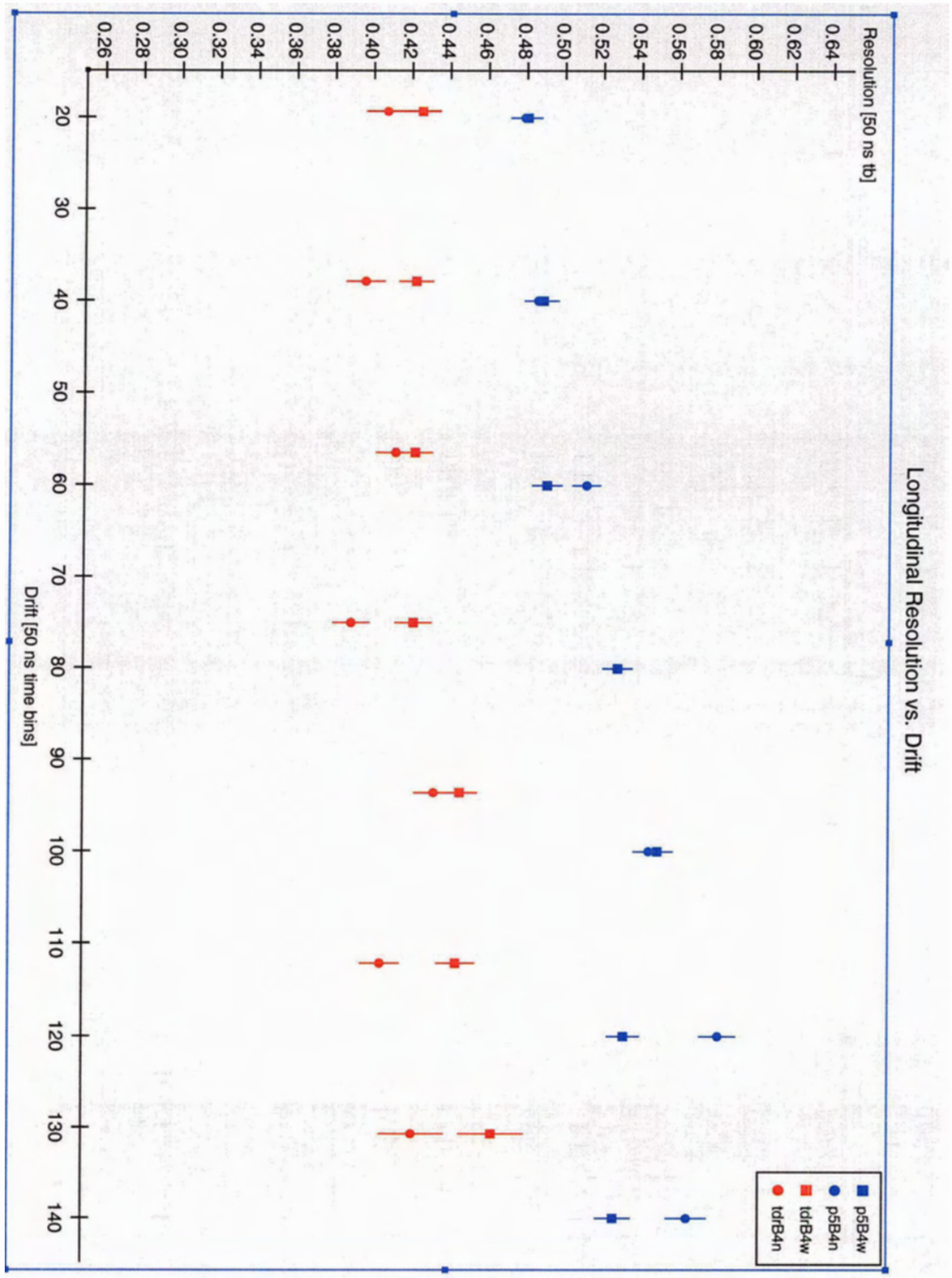

Figure 6.26: Longitudinal resolution vs. drift for all data.

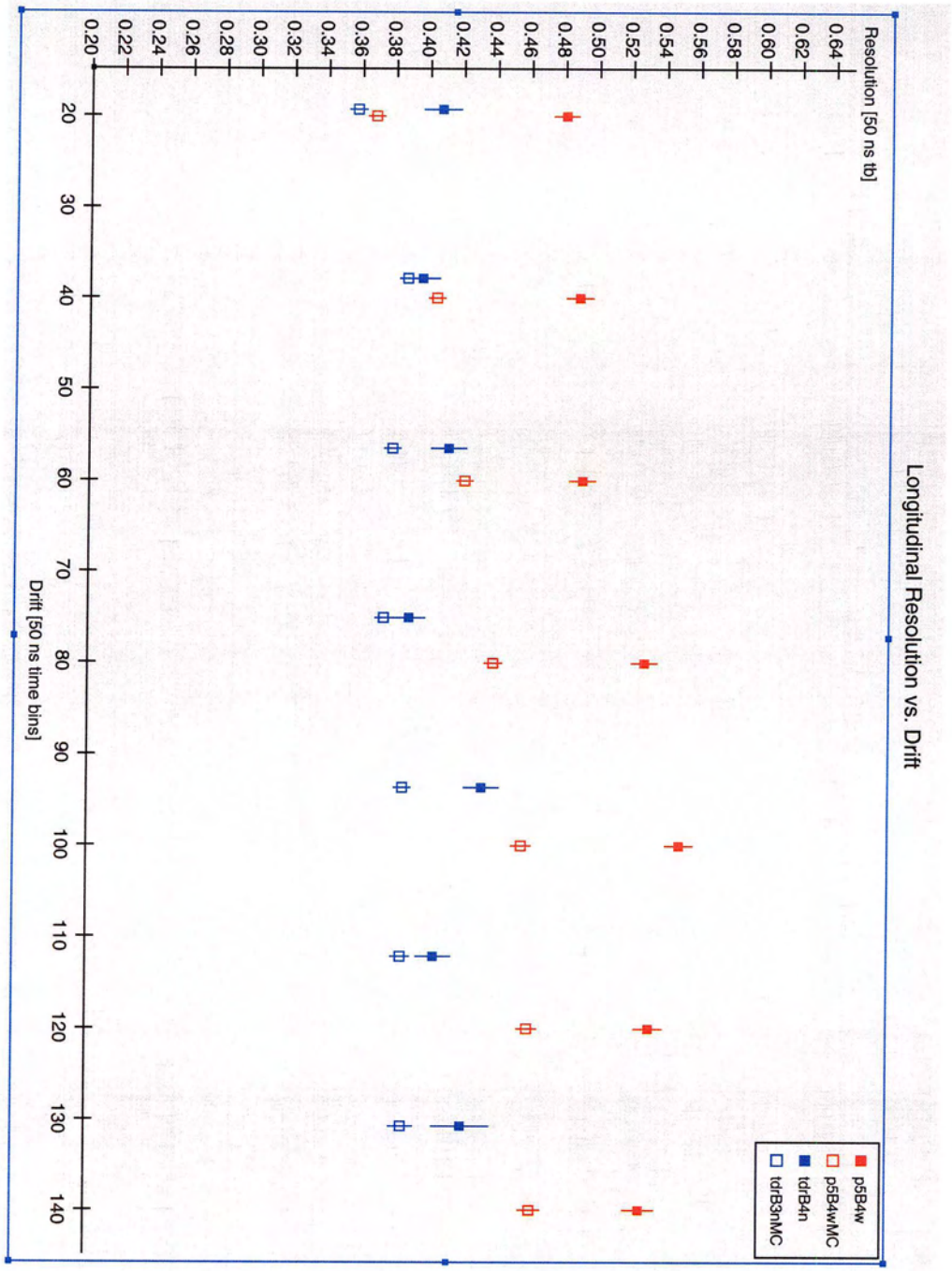

Figure 6.27: Longitudinal resolution vs. drift (data and MC).

Chapter 7

Conclusion

We have conducted the first tests of a GEM-TPC in a high magnetic field to measure the resolution capabilities of this device. We have studied the overall resolution as well the effects of different variables on the resolution in order to study systematic effects.

Our ultra-violet laser system lets us make precise measurements of the drift velocities of the electrons in our chamber. For data sets p5B4n, tdrB4w, tdrB4n, tdrB1n and tdrB0n the measured drift velocities are in agreement with what is predicted by the Magboltz simulation. The data set p5B4w showed a drift velocity which differed from the Magboltz simulation. This difference presumably was caused by having unknown gas constituents in the chamber. However, by measuring the drift velocities at different fields a stable operating point was found for data taking. Using the drift velocity measurements and the width of the tracks as a function of drift distance we calculated the diffusion and defocusing constants for each data set. After a correction was applied based on the MC the diffusion constants were found to be

in reasonable agreement with the Magboltz predicted values. Our MC has not been optimized to accurately reproduce the defocusing constants resulting in a discrepancy in the measured and simulated values. It is important to note is that the each gas possesses the properties which are needed in this type of detector, which are; high drift velocity, low diffusion in the drift volume and substantial defocusing through the amplification and readout regions.

A check for substantial systematics was done by considering the bias as a function of x, z and position on a pad, as well as the resolution as a function of x. We see no significant biases as a function of x or z and no substantial dependence of the resolution on x. We do however see a very minor effect which is a bias as a function of the position on the pad. This can be attributed to a small error in parameterizing the observed electron distribution. This effect is small in comparison to the overall resolution.

The resolution shows a strong dependence on the track angle (ϕ). This expected effect is due to the large fluctuation in the amount of ionization, (which is Landau distributed) along the track of the cosmic rays. The Poisson distributed laser track ionization did not show the same effect.

A study of the resolution as a function of position on the pads showed that the wide ($2.0\,mm$) pads showed a substantial degradation of the resolution close to the centre of the pad, with a larger effect seen for TDR gas than P5 gas. The narrow pad data showed a very small effect. However, it may be possible to optimize the

gas choice (perhaps P10 gas) and to use pads wider than $1.2\,mm$ without substantial degradation of the resolution in the pad centres.

The resolution did not show a substantial dependence on drift distance which is critical in a large scale detector. We have seen that the P5 gas performs better showing better resolution for all drift distances. We found that, for our wide pads TDR gas had a resolution of slightly greater than the goal of 110 μm while all other data sets were below this value for all drift distances.

The measurement of the longitudinal resolution is the only situation studied in which the TDR gas performed better than the P5 gas. The TDR gas showed less of a dependence on drift distance and overall better longitudinal resolution.

Section 1.2 derives a spatial resolution goal per point (ϵ) based on the design requirements of the International Linear Collider's central tracker of, $\epsilon < 110\,\mu m$. Table 6.7 shows the results of our tests for the overall point resolution of our chamber (which are in agreement with the MC values). Both data sets using the narrow pads showed overall resolution well below the goal of $110\,\mu m$. For the wide pad data sets the overall resolution is close to this goal with the P5 data below and the TDR data above. It should be noted that the data set using P5 gas with wide pads had gas transport properties which were actually slightly less desirable than what is expected for pure P5 gas. Also, except for the longitudinal resolution (which is not a critical a factor for this detector), the P5 gas performed better than the TDR gas.

In order to compare our resolution to that of wire TPCs we scale the resolu-

tion by the square root of the ratio of the sampling lengths of the chambers. The DELPHI TPC had a sampling length of $45\,mm$ and achieved a transverse resolution of $250\,\mu m$[5]. This gives us a corrected resolution for the DELPHI detector of $\sqrt{\frac{45}{7}} \times 250\mu m = 634\,\mu m$. The ALEPH TPC had a sampling length of $30\,mm$ and achieved a transverse resolution of $180\,\mu m$[6]. The same calculation gives an adjusted resolution for the ALEPH device of $373\,\mu m$. We see that our resolution is substantially better than that of these two detectors.

We have shown that time projection chamber using gas electron multipliers for gas amplification can achieve the space point resolution which is required for the momentum resolution goal for the central tracker at the ILC. Full scale TPCs have proven their worth in the past and with the new developments in gas amplification technology will undoubtedly become better and better instruments.

Bibliography

[1] TESLA, Technical Design Report part IV: A detector for TESLA (2001)

[2] Particle Data Group, Phys Lett. B 592 (2004) 268.

[3] Presented APS NW section meeting, Victoria (2005)

[4] D.R. Nygren, A Time Projection Chamber1975, Presented at 1975 PEP Summer Study, PEP 198 (1975), Included in Proceedings.

[5] DELPHI Collaboration, Nucl. Instr. and Meth. A 323 (1992) 209 212.

[6] ALEPH Collaboration, Nucl. Instr. and Meth. A 294 (1990) 121.

[7] F. Sauli, Nucl. Instr. and Meth. A 386 (1997) 531.

[8] GAS DETECTORS DEVELOPMENT - CERN, http://gdd.web.cern.ch/GDD

[9] F. Sauli and A. Sharma, Annu. Rev. Nucl. Sci. 49 (1999) 341 - 388.

[10] S.R. Amendolia, et al., Nucl. Instr. and Meth. A 283 (1989) 573 - 577.

[11] A. Bondar, et al., Nucl. Instr. and Meth. A 496 (2003) 325 - 332.

[12] R.K. Carnegie, et al., Nucl. Instr. and Meth. A 538 (2005) 372-383.